UNIVERSITY OF CALIFORNIA
SANTA CRUZ

STRAIN EFFECTS AND DIELECTRIC RESPONSE IN EXTREMELY STRONGLY CORRELATED MATTER IN TWO DIMENSIONS

A dissertation submitted in partial satisfaction of the
requirements for the degree of

DOCTOR OF PHILOSOPHY

in

PHYSICS

by

Michael R. Arciniaga

March 2022

The Dissertation of Michael R. Arciniaga
is approved:

Professor B. Sriram Shastry, Chair

Professor Jairo Velasco Jr.

Professor Sergey Syzranov

Peter Biehl
Vice Provost and Dean of Graduate Studies

Table of Contents

List of Figures

List of Tables

Abstract

Strain Effects and Dielectric Response in Extremely Strongly Correlated Matter in Two Dimensions

by

Michael R. Arciniaga

We adapt the theory of extremely correlated Fermi liquids in two dimensions to study the phenomena of anisotropic elastoresistivity and dielectric response in high-T_c superconducting cuprates. There has been considerable focus on the nematic susceptibility in iron-based superconducting systems in recent years, but not much is known for cuprates. Motivated by these experiments, in part I, we calculate the in-plane elastoresistivity for optimally- and over-doped cuprates in the normal state. We present results for strain-induced anisotropic effects on the resistivity, the optical weight, and local density of states, and we additionally calculate their associated susceptibilities. Our quantitative predictions for these quantities have the prospect of experimental tests in the near future. In part II of this dissertation, inspired by recent experiments using inelastic electron scattering off the surface of cuprate materials to obtain $\{\vec{q}, \omega\}$ dependence of the dielectric response, we study the t-J-V_C model in two dimensions. In this model in addition to the usual Hubbard-Gutzwiller short-range correlations, we add in the strong long-range correlations from Coulomb-type interactions on the tight-binding electrons. We calculate the $\{\vec{q}, \omega\}$ dependent charge density fluctuations using the Green's function from extremely correlated Fermi liquid theory which is characterized by quasiparticle

with a very small weight Z. Combining these properties with a novel set of formulae for the dynamical charge susceptibility and the dielectric constant that appropriately accounts for the physics of long-range Coulomb-type interactions in this model. We calculate the dynamical charge susceptibility $\widetilde{\chi}_{\rho\rho}(\vec{q},\omega)$, (longitudinal) dielectric constant $\varepsilon(\vec{q},\omega)$, current susceptibility $\widetilde{\chi}_{JJ}(\vec{q},\omega)$, conductivity $\sigma(\vec{q},\omega)$, and plasma frequency for any $\vec{q}$. We also present calculations for the first moment of the structure function and discuss a characteristic energy scale $\Omega_p(\vec{q})$ which locates the peaks in $\mathrm{Im}\,\widetilde{\chi}_{\rho\rho}(\vec{q},\omega)$.

For my Mom and Dad.

Acknowledgments

I would like to thank my advisor Sriram for his kindness and patience.

I also want to thank Edward and Peizhi for their encouragement and support.

Part I

INTRODUCTION

Chapter 1

Background and Motivations

The physics of Fermi liquid can be classified into three cases of interest depending on the asymptotic relation the interaction energy U and the kinetic "hopping" energy t. For the case of $U/t \ll 1$, the physics of Fermi liquids is well described by Landau Fermi liquid theory. In the intermediate regime for $1 < U/t < \infty$, the extensively studied Hubbard model is well suited. In the last case, $U/t \gg \infty$, double occupation at a single site on a lattice is strictly forbidden and in this regime is best described by the t-J model. Based on myriad of experiments, Anderson [2] argued that the *minimalist* t-J model is sufficient to describe physics of high-T_C superconductors.

The t-J model is one of the standard models in condensed matter physics and has been the subject of intense study for the past few decades. In this model Gutzwiller projected Fermi operators P_G capture the effects of extreme local interaction $U \to \infty$ which forbids double occupancy at a single lattice site. The calculation of the Green's function within this model comes with two fundamental challenges: (1) The lack of a small parameter makes Wick's theorem and perturbative schemes useless and (2) the non-canonical nature of electrons systems with forbidden double occupancies leads to non-trivial non-canonical anti-commutation relation. Shastry has overcome these difficulties with the recently developed *extremely correlated Fermi liquid theory* (ECFL) described in Refs. [62] and [66]. In particular the Schwinger method [36] is used to derive an equation of motion for the Green's function of non-canonical electrons, and the theory introduces a new parameter $\lambda \in [0, 1]$ which smoothly interpolates between the Schwinger equation of motion for a Fermi gas and the t-J model respectively.

In recent years there has been increased interest in the *elastoresistivity* (i.e., the strain dependence of resistivity) due to the discovery of strong nematicity in high-T_c superconductors. The study of elastoresistivity has potential value as a tool to illuminate on the nature of broken symmetries in these strongly correlated electron systems. Excited by the discovery of strong nematicity in said materials, researchers have measured using a piezoelectric device the electron nematic susceptibility χ_{nem} [Eq. (2.1)] on iron pnictide and, more recently, cuprate superconductors, and these experiments probe for existence of electron nematic phase transition. Inspired by these recent experiments, we adapt extremely correlated Fermi liquid theory in two dimensions to explore the effects of strain-induced anisotropy of high-T_c superconducting cuprate materials in their normal state and we calculate the elastoresistivity.

Experiments on the normal state, i.e., nonsuperconducting state, of high temperature superconductors has revealed many properties that cannot be explained by Landau Fermi liquid theory of metals. For this reason these materials are usually referred to as *strange metals*. Using Raman scattering experimentalist have observed a featureless continuum over a broad range of energies ω whose origin remains unexplained and more recently researchers have used *momentum resolved electron energy loss spectroscopy* (M-EELS) to find the finite momentum $\vec{q}$ dependence of the continuum. Motivated by these novel measurements, we modify extremely correlated Fermi liquid theory by adding the effects of strong long-range correlations due to Coulomb-type interactions, and we use a novel expression for the dielectric constant recently developed by this author and Shastry to provide the $\{\vec{q}, \omega\}$ dependent calculations the structure function from which we can elucidate the physics the charge fluctuations and collective modes of high-T_c superconducting curprates or more broadly in strange metals.

In this dissertation we apply extremely correlated Fermi liquid theory, which effectively captures the physics of the t-J model in a Green's function, to a quasi-two-dimensional electron system on a lattice. Anderson [2] suggested, based on myriad of experiments, that t-J model is well suited to describe the physics high-T_C superconducting cuprates and other strongly correlated materials. Here the two-dimensional model is a single-band approximation of the 3-band copper oxide planes. In Part II we present the theory of anisotropic strain effects in two dimensional extremely correlated systems with parameters tuned for BSCCO cuprate where we compute the resistivity, kinetic energy (i.e., f-sumrule for optical conductivity) and local density of states for comparison with experiment test in the near future. In Part III we calculate the dielectric constant ε and charge susceptibility $\widetilde{\chi}_{\rho\rho}$ for a two dimensional materials with strong short- and long-range correlations. Additionally, we compute the plasma dispersion ω_p, compressibility χ_{comp}, current susceptibility $\widetilde{\chi}_{JJ}$, optical conductivity $\mathrm{Re}\,\sigma$, and the f-sumrule $\widetilde{\omega}^{(1)}$. In Part IV we summarize some of the most important findings and present an outlook on works in progress.

Part II

THEORY OF STRAIN EFFECTS IN STRONGLY CORRELATED METALS

Chapter 2

Introduction and Motivation

Understanding the temperature and doping dependent electrical conductivity of very strongly correlated metals in two dimensions (2D) is a very important problem in condensed matter physics. Recent interest in *elastoresistivity*, i.e., the strain dependence of resistivity has been triggered by the discovery of strong nematicity in iron based superconductors [17, 61, 18]. The nematic susceptibility is defined as

$$\chi_{nem} = \lim_{\epsilon_{xx} \to 0} \frac{\rho'_{xx} - \rho_{xx}}{\rho_{xx}\epsilon_{xx}} \tag{2.1}$$

where $\rho'_{xx}(\rho_{xx})$ is the x-axis resistivity in the presence (absence) of a small strain ϵ_{xx}. The large magnitude of this dimensionless susceptibility ($|\chi_{nem}| \gtrsim 200$), and the peak like features in its temperature dependence suggest enhanced nematic fluctuations in the pnictides.

The situation for cuprates is less studied thus motivating the present work. The recently developed *extremely correlated Fermi liquid theory* (ECFL) [66] accounts quantitatively for the (unstrained) normal state resistivities of three families of single layer cuprates [64, 65]. This theory treats correlation effects within the well-defined t-t'-J model. The model lacks any explicit mechanism to drive large nematic fluctuations, but it is possible that these fluctuations are emergent. It is thus natural to ask if the theory can provide a benchmark scale for elastoresistivity effects in cuprates, as well as to examine if nematic fluctuations are encouraged. Towards this goal we present results for the anisotropic elastoresistivity in various geometries for cuprate materials in the normal state within the extremely correlated Fermi liquid theory (ECFL) [66] as applied to the t-t'-J model for spin-$\frac{1}{2}$ electrons on a square lattice given by the Hamiltonian

$$H = -\sum_{ij\sigma} t_{ij} \widetilde{C}^{\dagger}_{i\sigma} \widetilde{C}_{j\sigma} - \boldsymbol{\mu}\hat{N} + \frac{1}{2}\sum_{ij} J_{ij}\left(\vec{S}_i.\vec{S}_j - \frac{1}{4}n_i n_j\right). \tag{2.2}$$

Here $t_{ij} = t(t')$ for nearest (next-nearest) neighbor sites ij and is zero otherwise on the square lattice[1], $\hat{N}$ is the number operator, $\widetilde{C}_{i\sigma} = P_G C_{i\sigma} P_G$ and P_G is the Gutzwiller projection operator which projects out the doubly occupied states. Also the super-exchange $J_{ij} = J$ when acting on nearest neighbor sites and is zero otherwise. The other symbols have their usual meaning.

While the ECFL theory accounts for the variation of resistivity with a change of hopping parameters, we need another piece of information to calculate elastoresistivity.

---

[1] In the t-t'-J model the first and last term of Eq. 2.2, referred to as the hopping H_t and exchange H_J term, respectively, explicitly expanded as sum over neighbors is

$$H_t + \boldsymbol{\mu}\hat{N} = -t \sum_{<ij>\sigma} \widetilde{C}^{\dagger}_{i\sigma}\widetilde{C}_{j\sigma} - t' \sum_{\ll ij \gg\sigma} \widetilde{C}^{\dagger}_{i\sigma}\widetilde{C}_{j\sigma} \; ,$$

$$H_J = \frac{J}{2}\sum_{<ij>}\left(\vec{S}_i.\vec{S}_j - \frac{1}{4}n_i n_j\right) \; ,$$

where $<ij>$ is the sum over nearest neighbors, and $\ll ij \gg$ is the sum over second nearest neighbors. In terms of the Hubbard operators — see Eq. (3.1)—this becomes

$$H_t + \boldsymbol{\mu}\sum_{i\sigma} X_i^{\sigma\sigma} = -t \sum_{<ij>\sigma} X_i^{\sigma 0} X_j^{0\sigma} - t' \sum_{\ll ij \gg\sigma} X_i^{\sigma 0} X_j^{0\sigma} \; ,$$

That is a solution to the independent problem of describing the effects of strain on the hopping parameters of the underlying tight-binding model. In cuprates the t-t'-J model arises as an effective low energy model from downfolding from a three band (or in general multiband) description obtained within band structure calculations [86, 67, 48]. This procedure is not unique since the extent of correlations included in the band structure can differ among different calculations. We take the practical view that the hopping parameters can be chosen to depend parametrically on the distance between atoms, in parallel to the treatment of volume effects in transition metals by V. Heine [31]. Thus in our approach, a small strain can be parametrized through a single variable α relating the hopping to the separation R via the relation

$$t(R) \sim \frac{A}{R^{\alpha}}. \tag{2.3}$$

From tight binding theory $\alpha = l_1 + l_2 + 1$, where l_1, l_2 are the angular momenta of the overlapping orbitals [31]. Within this scheme we expect that compression enhances overlap and hence the magnitude of hopping, and conversely stretching reduces overlap. Excluding very strong multiband effects we may take $\alpha \in \{2, 5\}$ for cuprates. The single parameter needed for our purpose is α, since A is reabsorbed in the unstrained hopping. We further suggest that one may more realistically estimate this single parameter α by measuring other α dependent variation of physical variables with strain, as described

---

$$\begin{aligned} H_J = \frac{J}{2} \sum_{<ij>\sigma} X_i^{\sigma\sigma} \\ + \frac{J}{4} \sum_{<ij>\sigma_1\sigma_2} \{X_i^{\sigma_1\sigma_2} X_j^{\sigma_2\sigma_1} - X_i^{\sigma_1\sigma_1} X_j^{\sigma_2\sigma_2}\}\,. \end{aligned}$$

below.

This modeling neglects the possible three-dimensional effects, where the c-axis propagation could in certain situations influence the two-dimensional bands indirectly. Also cuprates with many layers per unit cell may have more complex dependence on strain as compared to single layer systems. Despite the above caveats in place, it is still worthwhile to study the model Eq. (2.2) together with the relation Eq. (2.3) for understanding the elastoresistivity of single layer cuprates.

The problem of (unstrained) normal state resistivity has been explored in various experiments [4, 56, 27] on different materials over the last few decades. Experiments reveal interesting and challenging transport regimes, termed the *strange metal* and the *bad metal* regime [26], whose existence is inexplicable within the standard Fermi liquid theory of metals. These results have attracted several numerical studies using the techniques of dynamical mean field theory[40, 83, 21], determinant quantum Monte-Carlo method [14, 32] and dynamical cluster approximation [47, 87] etc. These studies indicate that the unusual regimes are indicative of very strong correlations of the Mott-Hubbard variety.

Despite the numerical progress, few analytical techniques are available to extract the low temperature transport behavior, and thus better understand the various regimes. This is due to the inherent difficulties of treating strong correlations, i.e., physics beyond the scope of perturbation theory. Recently, the extremely correlated Fermi liquid theory (ECFL) [66, 63, 71] has been developed by Shastry and coworkers. This theory consists of a basic reformulation of strong correlation physics, and its many applications have been reported for the t-t'-J model in dimensions d=1,2,∞. This is a minimal and fundamental model to describe extreme correlations. The ECFL theory leads to encouraging results which are in close accord with experiments such as spectral line shape in angle-resolved photoemission spectroscopy (ARPES) [19, 43, 38, 85, 7, 28, 65], Raman susceptibility [45, 37], and particularly, resistivity [71, 22, 65]. A recent work [64] shows that the ECFL theory gives a quantitatively consistent account of the T and density dependence of the resistivity for single layer hole-doped and electron-doped correlated materials. Here we explore the strain dependence of the resistivity within the same scheme.

In the ECFL theory, the resistivity arises from (Umklapp-type) inelastic scattering between strongly correlated electrons. Here the hopping amplitudes of electrons play a dual role. The first one, that of propagating the fragile quasiparticles, is standard in all electronic systems. They provide a simple model for the band structure. Additionally, for very strong correlations the ECFL theory shows that the hopping parameters are also involved in the scattering of quasiparticles off each other[2]. A surprisingly low characteristic temperature scale [22, 65] emerges from the strong correlations, above which the resistivity crosses over from Fermi liquid type i.e. $\rho \sim T^2$ behavior, to an almost linear type i.e. $\rho \sim T$ behavior [65, 4].

From the above we argue that strain effects could provide a test of the underlying mechanism for resistivity within the ECFL theory to include strain dependence. Experiments probing these strain effects are likely in the near future, thus enabling an

---

[2] This can be seen e.g. Eq. (3.8), where the “interaction” term in the self-energy is determined by the $\varepsilon_{\vec{k}}$'s, the Fourier transform of the hopping matrix elements.

important test of the theory. For the purpose of independently estimating the strain-hopping parameter α in Eq. (2.3), we have identified two experimentally accessible variables. Firstly we study the integrated weight of the anisotropic electrical optical conductivity, i.e., the f-sum rule weight, accessible in optical experiments [9, 10]. Secondly we study the local density of states (LDOS), measurable through scanning tunneling microscopy (STM) [50, 84, 16, 39, 25]. The f-sum rule weight in tight binding systems is related to the expectation of the kinetic energy, or hopping, and can be obtained from the Green's function. The LDOS can also be calculated from the local Green's function easily.

The plan for this part of the paper is as follows: In Chapter 3, (A) we introduce the t-t'-J model and summarize the second order ECFL equations and the corresponding Green's functions and self-energies. (B) We describe how to convert the lattice constants and hopping parameters for a system under strain. (C) We outline the parameters for the program. In Chapter 4, we present the detailed calculation for and results of (A) the resistivity, (B) the kinetic energy, and (C) the LDOS and their associated susceptibilities with respect to strain. We provide a brief summary and discussion of our results and future work in Chapter 5.

Chapter 3

Methods & Parameters

3.1 The Model

It has been argued that the t-t'-J model is key to describing the physics of high-T_c superconducting materials [2]. This model is composed of two terms: $H_{tJ} = H_t + H_J$ where H_t is derived by taking the infinite-U limit of the Hubbard model plus an additional term H_J which introduces antiferromagnetic coupling. The general Hamiltonian Eq. (2.2) can be rewritten in terms of the Hubbard X operators [66] as

$$\begin{aligned} H_t &= -\sum_{ij\sigma} t_{ij} X_i^{\sigma 0} X_j^{0\sigma} - \boldsymbol{\mu} \sum_{i\sigma} X_i^{\sigma\sigma} \, , \\ H_J &= \frac{1}{2} \sum_{ij\sigma} J_{ij} X_i^{\sigma\sigma} \\ &\quad + \frac{1}{4} \sum_{ij\sigma_1\sigma_2} J_{ij} \{ X_i^{\sigma_1\sigma_2} X_j^{\sigma_2\sigma_1} - X_i^{\sigma_1\sigma_1} X_j^{\sigma_2\sigma_2} \} \end{aligned} \tag{3.1}$$

Here t_{ij} and J_{ij} are already defined below Eq. (2.2). We present results for both vanishing and nonvanishing J_{ij}. The operator $X_i^{ab} = |a\rangle \langle b|$ takes the electron at site i from the state $|b\rangle$ to the state $|a\rangle$ where $|a\rangle$ and $|b\rangle$ are one of the three allowed states: two occupied states $|\uparrow\rangle$, $|\downarrow\rangle$, or the unoccupied state $|0\rangle$ — the appropriate X operator referring to the doubly occupied state $|\uparrow\downarrow\rangle$ is excluded in both the Hamiltonian and state space. The X operator relates to the alternative representation used in Eq. 2.2 as follows: $X_i^{\sigma 0} \to \widetilde{C}_{i\sigma}^{\dagger}$, $X_i^{\sigma 0} \to \widetilde{C}_{i\sigma}$ and $\sum_\sigma X_i^{\sigma\sigma} \to n_i$.

3.2 The ECFL Equations

In this section, we briefly introduce the ECFL equations for the t-t'-J model. More details can be found in Refs. [66, 63, 71, 65]. In the ECFL theory, the one-electron Green's function $\mathcal{G}$ is found using the Schwinger method [36] and in momentum space is factored as a product of an auxiliary Green's function $\mathbf{g}$ and a "caparison" function $\widetilde{\mu}$:

$$\mathcal{G}(k) = \mathbf{g}(k) \times \widetilde{\mu}(k) \tag{3.2}$$

where $k \equiv (\vec{k}, i\omega_k)$, and $\omega_k = (2k+1)\pi k_B T$ is the Fermionic Matsubara frequency and subscript k is an integer. The auxiliary $\mathbf{g}(k)$ plays the role of a Fermi-liquid type Green's function whose asymptotic behavior is $1/\omega$ as $\omega \to \infty$, and $\widetilde{\mu}$ is an adaptive spectral weight that mediates between two conflicting requirements [63]: (1) the high frequency behavior of the noncanonical fermions and (2) the Luttinger-Ward volume theorem at low frequencies.

The Schwinger equation of motion for the physical Green's function can be symbolically written as [63]

$$\left(\mathbf{g}_0^{-1} - \hat{X} - Y_1\right) . \, \mathcal{G} = \delta \, (\mathbb{1} - \gamma). \tag{3.3}$$

where $\hat{X}$ represents a functional derivative and Y_1 describes a Hartree-type energy, i.e., $\mathcal{G}$ convoluted with hopping and exchange interactions. The left hand side of Eq. (3.3) is analogous to that of the Schwinger-Dyson equation for Hubbard model [5]: $\left(\mathbf{g}_0^{-1} - U\delta/\delta\mathcal{V} - UG\right).G = \delta\mathbb{1}$ where G is one electron Green's function on the Hubbard model. Observe on the right side of Eq. (3.3), the essential difference is the γ term which is proportional to a local $\mathcal{G}$ and originates from the noncanonical algebra of creation and annihilation operators. The noncanonical nature of operators and the lack of an obvious small parameter for expansion present the main difficulties towards solving this equation.

To tackle these difficulties, the ECFL theory inserts into Eq. (3.3) the λ parameter

$$\left(\mathbf{g}_0^{-1} - \lambda\hat{X} - \lambda Y_1\right) . \, \mathcal{G} = \delta \, (\mathbb{1} - \lambda\gamma). \tag{3.4}$$

where $\lambda \in [0, 1]$ interpolates from a noninteracting to fully interacting system. This parameter plays a parallel role to that of inverse spin parameter $1/2S$ in quantum magnets, where S is the magnitude of the spin. Then we expand Eq. (3.4) systematically with respect to λ up to a finite order and at the end set $\lambda = 1$ to recover the full t-t'-J physics. The introduction of λ bound to $[0, 1]$ in ECFL makes it possible that a low-order expansion could be enough to describe low-energy excitations in a large region of doping. This argument has been justified in one [46] and infinite [71] dimensions by benchmarking against exact numerical techniques and in two [65]dimensions by comparing well with experiments.

In the following, we use the minimal version of second order (in λ) ECFL equations [65]:

$$\widetilde{\mu}(k) = 1 - \lambda\frac{n}{2} + \lambda\psi(k) \tag{3.5}$$

$$\mathbf{g}^{-1}(k) = i\omega_k + \boldsymbol{\mu} - \epsilon_{\vec{k}} + \lambda\frac{n}{2}\epsilon_{\vec{k}} - \lambda\phi(k) \tag{3.6}$$

where $\boldsymbol{\mu}$ is the chemical potential (denoted in boldface) and $\epsilon_{\vec{k}}$ is the bare band energy found by taking the Fourier transformation of the hopping parameter. The physical Green's function features two self-energy terms: the usual Dyson-like self-energy denoted $\phi(k)$ in the denominator and a second self-energy in the numerator $\psi(k)$. The self-energy $\phi(k)$ can conveniently be decomposed as follows: $\phi(k) = \chi(k) + \epsilon'_{\vec{k}}\psi(k)$ where $\chi(k)$ denotes a self-energy part, $\epsilon'_{\vec{k}} = \epsilon_{\vec{k}} - u_0/2$ and $\psi(k)$ the second self-energy. Here u_0 acts as a Lagrange multiplier, enforcing the shift invariance [66, 63, 65] of the t-t'-J model at every order of λ. The two self-energies functions ψ and χ expanded formally in λ to second order approximation $\mathcal{O}(\lambda^2)$ are $\psi = \psi_{[0]} + \lambda\psi_{[1]} + \ldots$ and $\chi = \chi_{[0]} + \lambda\chi_{[1]} + \ldots$. The expression for these self-energies in the expansion are

$$\psi_{[0]}(k) = 0, \quad \chi_{[0]}(k) = -\sum_p \left(\epsilon'_{\vec{p}} + \frac{1}{2}J_{\vec{k}-\vec{p}}\right)\mathbf{g}(p) \tag{3.7}$$

and

$$\psi_{[1]}(k) = -\sum_{pq} \left(\epsilon'_{\vec{p}} + \epsilon'_{\vec{q}} + J_{\vec{k}-\vec{p}}\right) \mathbf{g}(p)\mathbf{g}(q)\mathbf{g}(p+q-k) \tag{3.8}$$

$$\begin{aligned}\chi_{[1]}(k) = -\sum_{pq} &\left(\epsilon'_{\vec{p}} + \epsilon'_{\vec{q}} + J_{\vec{k}-\vec{q}}\right)\left(\epsilon'_{\vec{p}+\vec{q}-\vec{k}} + J_{\vec{k}-\vec{p}}\right) \\ &\times \mathbf{g}(p)\mathbf{g}(q)\mathbf{g}(p+q-k)\end{aligned} \tag{3.9}$$

where $\sum_k \equiv \frac{k_B T}{N_s} \sum_{\vec{k},\omega_k}$ and $J_{\vec{q}}$ is the Fourier transform of J_{ij} [3]. By setting λ to 1, the resulting expressions for the ECFL equations expanded to $\mathcal{O}(\lambda^2)$ are

$$\widetilde{\mu}(k) = 1 - \frac{n}{2} + \psi(k) \tag{3.10}$$

$$\begin{aligned}\mathbf{g}^{-1}(k) = i\omega_k + \boldsymbol{\mu} - \epsilon_{\vec{k}} + \frac{n}{2}\epsilon_{\vec{k}} - \chi_{[0]}(k) \\ - \chi_{[1]}(k) - \epsilon'_{\vec{p}}\psi_{[1]}(k)\end{aligned} \tag{3.11}$$

We can verify that an arbitrary shift of $\epsilon_{\vec{k}} \to \epsilon_{\vec{k}} + \mathbf{c}_0$ leaves the above expression invariant by shifting $\boldsymbol{\mu} \to \boldsymbol{\mu} + \mathbf{c}_0$ and $u_0 \to u_0 + 2\mathbf{c}_0$. In this sense, we may take u_0 as a second chemical potential. We can determine the two chemical potentials $\boldsymbol{\mu}$ and u_0 by satisfying the following number sum rules

$$\sum_k \mathbf{g}(k) e^{i\omega_k 0^+} = \frac{n}{2} = \sum_k \mathcal{G}(k) e^{i\omega_k 0^+} , \tag{3.12}$$

where n is the particle density. We find the spectral function $\rho_{\mathcal{G}}(k) = -1/\pi \mathrm{Im}\, \mathcal{G}(k)$ by analytically continuing (i.e., $i\omega_k \to \omega + i\eta$) and by solving Eq. (3.2) and Eqs. (3.7)–(3.12)

---

[3] Here $J_{\vec{q}}$ is the Fourier transform of J_{ij} over nearest neighbors. For a homogeneous and translationally invariant system, the Fourier transform gives $J_{\vec{q}} = 2J_x \cos(q_x a) + 2J_y \cos(q_y b)$ on a rectangular lattice where J_x and J_y are the exchange parameters along the principle axes.

iteratively. We remind the reader that the spectral function $\rho_{\mathcal{G}}(\vec{k},\omega)$ is referred to in most experimental literature by the symbol $A(\vec{k},\omega)$. We can recover the interacting Green's function from $\rho_{\mathcal{G}}$ using

$$\mathcal{G}(\vec{k},i\omega_k)=\int_{-\infty}^{\infty}\frac{\rho_{\mathcal{G}}(\vec{k},\nu)}{i\omega_k-\nu}d\nu\ . \tag{3.13}$$

3.3 Strain effects on hopping and exchange

§Converting lattice constant changes to hopping changes: The t-t'-J model in two dimensions describes the hopping of electrons between copper atoms in the 2-d plane. In this model, the hopping parameters with strain and without strain are denoted as

$$\{t_x,t_y,t_d\}\rightarrow\{t,t,t'\}. \tag{3.14}$$

Thus under strain t_x and t_y refer to nearest neighbor hops along x and y axes, and t_d is the second neighbor hopping along the diagonal of the square lattice. We start with the tetragonal symmetry case $t_x=t_y=t$ where there are just two parameters t,t'.

At the level of a single bond between two coppers, any generic hopping $t(R)$ for a bond with length R can be represented by [31]

$$t(R)\sim\frac{A}{R^{\alpha}}\ , \tag{3.15}$$

where A is a constant. In the simplest cases, the exponent α is given by the angular momentum l_1,l_2 of the relevant atomic shells of the two atoms by the formula

$$\alpha=l_1+l_2+1\ . \tag{3.16}$$

Thus for two copper atoms $l_1 = l_2 = 2$ and hence we might expect

$$\alpha \sim 5, \tag{3.17}$$

whereas for copper oxygen bonds $l_1 = 2,\ l_2 = 1$, therefore

$$\alpha \sim 3\ . \tag{3.18}$$

For the effective single band description of the cuprate materials, it is not entirely clear what value of α is most appropriate. Comparisons with experiments might be the best way to decide on this question, when the results become available. Until then we can bypass this issue by presenting the theoretical results in terms of $\frac{\delta t}{t}$ rather than the strain itself. Towards this end Eq. (3.15) is a very useful result. We rewrite it as

$$\frac{\delta t(R)}{t(R)} = -\alpha\, \frac{\delta R}{R}, \tag{3.19}$$

thus enabling us to convert a change of the lattice constant to that of the corresponding hopping, using only the value of t and α. Throughout this paper we will refer to $\delta t/t$ as "strain" or with emphasis as "hopping strain" in order to distinguish it from "conventional strain" $\delta R/R$. Strain will always refer to variations along the x axis unless otherwise noted.

§Geometrical aspects of the strain variation: Our calculation studies a few variations of parameters. We start on a lattice with tetragonal symmetry at $t \sim 5220$K (0.45eV), and we vary t' to capture both electron-doped ($t' > 0$) and hole-doped ($t' < 0$) cuprates. The magnitude of t is only a crude estimate, it is refined for different single layer cuprate systems in Ref [64].

On the distorted lattice with orthorhombic symmetry and lattice constants a and b, the three distances of interest (two sets of nearest neighbors and one set of second neighbors) are

$$a,\ b,\ \ \rho = \sqrt{a^2 + b^2}. \tag{3.20}$$

For the tetragonal case we refer to the undistorted lattice parameter asa_0, thus $a = b = a_0$, $\rho = \sqrt{2}a_0$. We next study the effect of stretching ($\delta a > 0$) or compressing ($\delta a < 0$) the x-axis lattice constant, leaving the y-axis unchanged. The changes in the lattice constants then read as

$$a \to a_0 + \delta a;\ \ b \to a_0;\ \ \rho \to \sqrt{2}a_0 + \frac{\delta a}{\sqrt{2}}\ . \tag{3.21}$$

We denote the strain in the x-direction as

$$\epsilon_{xx} = \frac{\delta a}{a_0}. \tag{3.22}$$

In terms of the strain, we can rewrite the distances to neighbors as

$$a = a_0(1 + \epsilon_{xx}),\ \ b = a_0,\ \ \rho = \sqrt{2}a_0\left(1 + \frac{\epsilon_{xx}}{2}\right)\ , \tag{3.23}$$

so that $\epsilon_{xx} > 0$ is regarded as stretching and $\epsilon_{xx} < 0$ as compression. The single particle (tight-binding) energies for the distorted lattice are given by

$$\epsilon_{\vec{k}} = -2t_x \cos(k_x a) - 2t_y \cos(k_y b) - 4t_d \cos(k_x a)\cos(k_y b).$$

In terms of the band parameters of the unstrained system t and t', we can write the anisotropic band parameters as

$$t_x = (1 - \alpha\ \epsilon_{xx})\ t,\ \ t_y = t,\ \ t_d = \left(1 - \alpha\ \frac{\epsilon_{xx}}{2}\right) t'\ , \tag{3.24}$$

where the factor of $\frac{1}{2}$ for t_d comes about due to a shorter stretching of ρ as in Eq. (3.23). Their strain variations are denoted by

$$\frac{\delta t_x}{t_x} \equiv \frac{\delta t}{t} = -\alpha\epsilon_{xx}, \quad \frac{\delta t_y}{t_y} = 0, \quad \frac{\delta t_d}{t_d} = -\frac{1}{2}\alpha\epsilon_{xx}. \tag{3.25}$$

These formulas relate the change in hopping to the physical strain, and thus involve the parameter α which is somewhat uncertain. For that reason, we actually vary $\frac{\delta t}{t}$ in this study. We also go beyond the linear response regime, i.e., we use larger values of $\frac{\delta t}{t}$ than those attainable in the laboratory. In such a case we set $\frac{\delta t_d}{t_d} = \frac{\delta t}{2t}$. To summarize the sign convention used in this work,

$$\begin{aligned} &\text{compress:} && \frac{\delta t}{t} > 0, \quad \epsilon_{xx} < 0 \\ &\text{stretch:} && \frac{\delta t}{t} < 0, \quad \epsilon_{xx} > 0. \end{aligned} \tag{3.26}$$

§Converting hopping changes into exchange changes: In this model, the superexchange interaction maps to hopping as follows: $J = t^2/U$ where U is the on site energy of the Hubbard model. As we vary the hopping parameter, we find $\delta J = 2(\delta t/t)J$ since U does not vary with strain. In this model the first neighbor exchange parameters with and without strain, similar to Eq. 3.14, are denoted as

$$\{J_x, J_y\} \rightarrow \{J, J\}\ , \tag{3.27}$$

where J_x and J_y refer to the first neighbor exchange interactions along the x and y axes. In terms of hopping changes we can rewrite the exchange parameters as

$$J_x = \left(1 + 2\frac{\delta t_{xx}}{t_{xx}}\right) J, \quad J_y = J\ . \tag{3.28}$$

3.4 Parameters in the program

The model considered applies to several classes of materials, such as the cuprates, the sodium cobaltates, and presumably also to the iron arsenide superconductors. We shall restrict our discussion to the cuprates where the parameters are fairly well agreed upon in the community [2, 55, 64].

In this calculation, we set $t = 1$ as our energy scale and we allow t'/t to vary between -0.4 and 0.4, to cover the full range of cuprate materials. The hopping strain $\delta t/t$ is varied from -0.15 to 0.15. The exchange parameter J is set to zero except where otherwise noted. We convert the energy to physical units by setting $t = 0.45$eV, and hence the bandwidth is $W = 8t = 3.6$eV. If one wants to make a different choice for t, this can be done by rescaling the energies and T's by the same scaling factor.

We focus on the optimal doping case $\delta = 0.15$ for cuprate materials[4]. Here δ refers to the hole doping and relates to the particle density as follows $\delta \equiv (1 - n)$. The temperature range is set to $T \in [37, 450]$K. Lower temperatures than this lie outside the range of convergence for the current scheme. For the interacting system we solve the ECFL equations [Eqs. (3.7)–(3.12)] iteratively on a real frequency grid of size $N_\omega = 2^{14}$ within the range [-2.5W,2.5W], where W is the bare bandwidth, and a lattice $L \times L$ with $L = 61, 79, 135$. The scale of the frequency grid is tuned to capture the low-T physics. A frequency grid of size $N_\omega = 2^{16}$ only slightly improves our results at much larger computational costs. We primarily use an $L > 61$ for $t' > 0$ at low temperatures (i.e., $T < 100$K) in order to get sufficient resolution to converge electrical resistivity calculation. The need for a high resolution lattice at low temperatures is a product of the spectral function which features higher, sharper peaks for $t' > 0$, to which the resistivity calculation is sensitive [65], i.e., a larger grid is required to settle the unphysical oscillations in the resistivity calculation. For the noninteracting system we compute LDOS using a system of size $N_\omega = 2^{12}$ and $L = 271$.

---

[4] We refer to $n = 0.85$ as the optimal density since in a typical single-layer cuprate superconductors such as $La_{2-x}SrCuO_4$ (LSCO) — to which the 2D t-J model is most relevant the system — obtains its maximum critical temperature T_c at hole doping $\delta = 0.15$. Similarly, $Ba_2Sr_2CaCu_2O_{8+\delta}$ Bi2212) a double-layer curprate superconductor obtains its max T_c at doping $\delta = 0.15$.

Chapter 4

Results

Here we present the effects of strain along the x axis on electrical resistivity, kinetic energy and LDOS and their associated susceptibilities in response to a compressive ($\delta t/t > 0$) and tensile ($\delta t/t < 0$) hopping strain.

4.1 Resistivity for an x-axis strain

We now study the response of electrical resistivity ρ_α characterized by electron-electron scattering [65] in the presence of a strain. We use the bubble approximation, factoring the current correlator as $\langle J(t)J(0)\rangle \sim \sum_k v_{\vec{k}}^2 \mathcal{G}^2(k)$ with suitable vertices $v_{\vec{k}}$ and dressed Green's function $\mathcal{G}$, to compute the conductivity σ_α. Our picture of a quasi-2D metal consists of well separated Cu-O planes and hence each plane can be characterized using the 2D t-J model. The weak k dependence of the self-energy as seen in Fig. 3 of Ref. [65] diminishes the significance of vertex corrections. In fact the self-energy is completely k independent in the d=∞ limit, and studies in this limit [22] have successfully implemented the bubble approximation while completely ignoring vertex corrections. We shall calculate and quote the following objects denoting the irreducible representations of the D_{4h} point group by the standard names [77, 30, 42, 61]

- $\rho'_{xx}(T)$, the strained version of resistivity along the x-axis.
- $\rho'_{yy}(T)$, the strained version of resistivity along the y-axis.
- ρ_{xx}, the resistivity for the tetragonal lattice, which is the same as ρ_{yy}.
- XX component variations:

$$-(\rho'_{xx} - \rho_{xx})/(\rho_{xx}\delta t/t) \text{ vs } T$$

- YY component variations:

$$-(\rho'_{yy} - \rho_{yy})/(\rho_{xx}\delta t/t) \text{ vs } T$$

- A_{1g} symmetry variations:

$$-\frac{\rho'_{xx} + \rho'_{yy} - 2\rho_{xx}}{2\rho_{xx}\delta t/t} \text{ vs } T$$

- B_{1g} symmetry variations:

$$-\frac{\rho'_{xx} - \rho'_{yy}}{\rho_{xx}\delta t/t} \text{ vs } T$$

Of special interest are the $\rho'_{xx} + \rho'_{yy}$ response which corresponds to the A_{1g} irreducible representation (irrep) and the $\rho'_{xx} - \rho'_{yy}$ response, corresponding to the B_{1g} irrep.

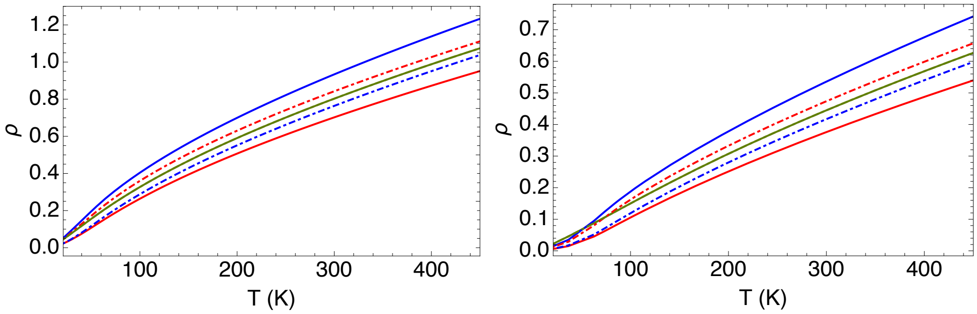

(a) $t'/t = -0.4, n = 0.85$

(b) $t'/t = -0.2, n = 0.85$

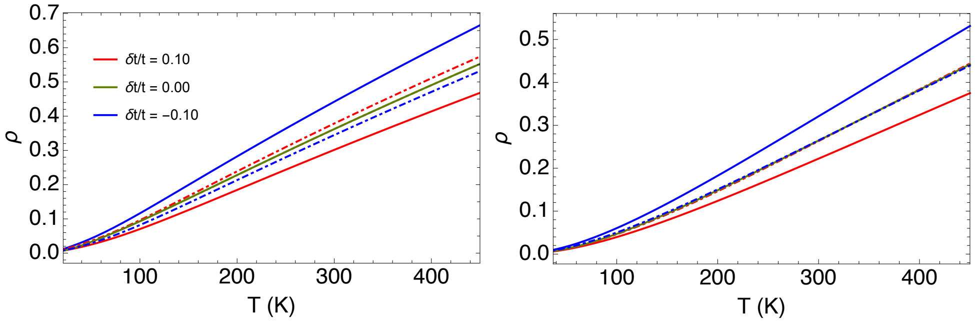

(c) $t'/t = 0.0, n = 0.85$

(d) $t'/t = 0.2, n = 0.85$

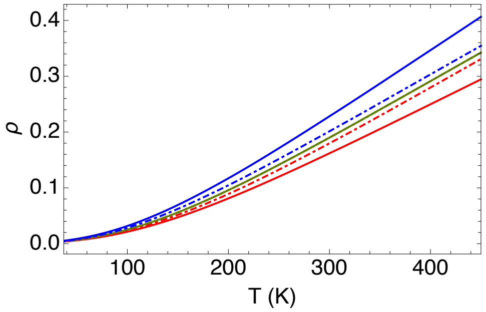

(e) $t'/t = 0.4, n = 0.85$

Figure 4.1: The longitudinal and transverse resistivities, ρ_{xx} (solid) and ρ_{yy} (dashed) respectively, versus temperature at filling $n = 0.85$, for various t', and at representative strains. While the green curves are for the unstrained case, the red curves correspond to a compressive strain $\delta t/t = 0.10$ (i.e. $\epsilon_{xx} \sim -.02$), and the blue curves correspond to a tensile strain $\delta t/t = -0.10$ (i.e. $\epsilon_{xx} \sim .02$), if we take $\alpha \sim 5$. (a) $t'/t = -0.4$, $n = 0.85$; (b) $t'/t = -0.2$, $n = 0.85$; (c) $t'/t = 0.0$, $n = 0.85$, (d) $t'/t = 0.2$, $n = 0.85$, (e) $t'/t = 0.4$, $n = 0.85$. All figures share the legend. The resistivity in physical units can be found by $\rho_{physical} = \rho \times \rho_0$, where $\rho_0 = \mathfrak{c}_0 h/e^2 \sim 1.17\text{m}\Omega\text{cm}$.

§Computation of the anisotropic resistivity: To find the anisotropic resistivity, we compute the dimensionless conductivity [65] for the anisotropic case

$$\sigma_{xx} = \langle \Upsilon_{\vec{k}} (\hbar v^x_{\vec{k}})^2/(ab)\rangle_k \ , \tag{4.1}$$

$$\sigma_{yy} = \langle \Upsilon_{\vec{k}} (\hbar v^y_{\vec{k}})^2/(ab)\rangle_k \tag{4.2}$$

where $\langle A\rangle_k = \frac{1}{N_s}\sum_{\vec{k}} A$, $N_s = L \times L$ and

$$\Upsilon_{\vec{k}} = (2\pi)^2 \int_{-\infty}^{\infty} d\omega (-\partial f/\partial\omega) \rho^2_{\mathcal{G}}(\vec{k},\omega) \tag{4.3}$$

where $f(\omega) \equiv 1/(1+\exp(\beta\omega))$ is the Fermi function, $\rho_{\mathcal{G}}(k)$ is the spectral function from ECFL theory up to $\mathcal{O}(\lambda^2)$, and $v^x_{\vec{k}}$, $v^y_{\vec{k}}$ are the bare vertices, which are defined as

$$v^x_{\vec{k}} = \frac{1}{\hbar}\frac{\partial \epsilon_k}{\partial k_x} = \frac{a}{\hbar}\frac{\partial \epsilon_k}{\partial k_1} \ , \tag{4.4}$$

$$v^y_{\vec{k}} = \frac{1}{\hbar}\frac{\partial \epsilon_k}{\partial k_y} = \frac{b}{\hbar}\frac{\partial \epsilon_k}{\partial k_2} \tag{4.5}$$

where $k_1 = k_x a$ and $k_2 = k_y b$ denote the components of the dimensionless momenta. Inserting the dimensionless momenta into Eq. (4.2), we obtain

$$\sigma_{xx} = \left\langle \Upsilon_{\vec{k}} \left(\frac{d\epsilon_{\vec{k}}}{dk_1}\right)^2 (a/b) \right\rangle_k \ , \tag{4.6}$$

$$\sigma_{yy} = \left\langle \Upsilon_{\vec{k}} \left(\frac{d\epsilon_{\vec{k}}}{dk_2}\right)^2 (b/a) \right\rangle_k \tag{4.7}$$

for the dimensionless conductivity. The corresponding dimensionless resistivities are $\rho_{xx} = 1/\sigma_{xx}$ and $\rho_{yy} = 1/\sigma_{yy}$.

The electrical resistivity can be converted to physical units as follows: $\rho_{physical,\alpha} = \rho_\alpha \times \rho_0$ where $\rho_0 = \mathfrak{c}_0 h/e^2 (\sim 1.171 \text{ m}\Omega\text{cm})$ sets the scale for the resistivity, and $\alpha = xx$ describes the longitudinal (i.e., current $\parallel \epsilon_{xx}$) resistivity and yy describes the transverse (i.e., current $\perp \epsilon_{xx}$) resistivity. Here $\mathfrak{c}_0 \sim 6.645$ is the typical separation between parallel Cu-O planes[5] (see Ref. [64]. In order to estimate the magnitude of the inelastic scattering, we can relate the dimensionless resistivity to $\langle k_F \rangle \ell$ as follows $\langle k_F \rangle \ell = 1/\rho_\alpha$ as argued in Refs. [4, 3] for quasi-2D materials, where $\langle k_F \rangle$ is an (angle averaged) effective Fermi momentum and ℓ is the mean-free-path. Hence we expect $\rho_\alpha/\rho_0 < 1$ in a good metal.

4.1.1 The raw resistivities

We first present the effects of hopping strain $\delta t/t$ on resistivity. In Fig. 4.1, we study the anisotropy of the raw dimensionless resistivity over a broad range of temperatures at the optimal density $n = 0.85$. Figure 4.1 displays the longitudinal resistivity ρ_{xx} (solid) and the transverse resistivity ρ_{yy} (dashed) for a compressive strain (red) and tensile strain (blue) in comparison to the unstrained tetragonal system (green). Here we used a representative magnitude of compressive strain $\delta t/t = 0.10$ (i.e., $\epsilon_{xx} \sim -.02$). We observe that longitudinal resistivity under a compressive strain ($\delta t/t > 0$) is reduced, and conversely, under a tensile strain ($\delta t/t < 0$) it is enhanced across the displayed temperature range for all t'. The response for transverse resistivity is less than the longitudinal one in magnitude. An interesting new feature lies in the t' dependence; we note that magnitude and sign of the change in transverse resistivity is controlled by t', e.g., for $t' = 0.2t$ the resistivity is almost unchanged for all strains.

---

[5] The unstrained system assumes a body-centered orthorhombic unit cell (a, b, c) where a, b are the lattice constants of the base and c is that of the height. In the expression for resistivity ρ_0, $\mathfrak{c}_0$ corresponds to the interlayer separation $\mathfrak{c}_0 = c/2$ between copper-oxide planes.

These behaviors can be understood qualitatively in the following ways. First, let us look at the simplest case with $t' = 0$ as in Fig. 4.1(c). When the system is compressed in the x axis, the hopping t_x rises according to Eq. (3.24) and so does the conductivity along the same direction, and vice versa. Hence, the longitudinal resistivity gets suppressed (enhanced) under compressive (tensile) strains. One can also consider isolating the strain-induced effects in Eqs. (4.6) and (4.7) from the band structure, contained in $v^{\alpha}_{\vec{k}}$, and from the spectral function $\rho_{\mathcal{G}}$, which accounts for the influence of the Gutzwiller correlations on resistivity. (Changes in the resistivity due to variation of the explicit lattice constants are small.) When we exert a compressive strain, this produces additive changes to the longitudinal resistivity due to in equal parts (1) changes in vertex and (2) T-dependent changes in spectral function, both arising from the enhancement of t_x. Whereas for the transverse resistivity the hopping parameter t_y is unchanged and hence changes to resistivity from the band structure become less important and as a result the transverse resistivity is dominated by strain-induced effects on the spectral function. For this reason, the transverse response to compressive strain is generally smaller in magnitude than the longitudinal response and likewise for a tensile strain both shown in panel (c). We also find that the transverse strain response has a different sign than the longitudinal one when there is no second neighbor hopping.

Now let us turn on t'. According to Eq. (3.24), the strain has a longitudinal-like effect, only smaller, on the magnitude of the second neighbor hopping. Turning on a positive t' strengthens longitudinal response and "counters" the transverse response from t_y hopping. Therefore we see that the longitudinal curves depart further from the unstrained one in panels (d) and (e), and it also explains why the transverse change almost vanishes for $t' = 0.2$ in panel (d) and switches to the same sign as the longitudinal one for $t' = 0.4$ in panel (e). Likewise turning on a negative t' weakens the longitudinal response and enhances the transverse response, so that the longitudinal response gets smaller in panel (a) and (b) while the transverse shifts more explicitly to the same side as $t' = 0$.

Next we discuss how strain affects the effective interaction and the characteristic temperature scale. We mainly use the longitudinal resistivity in this discussion because the longitudinal response is more explicit. In our recent work [65], a significant finding was the t' dependence of the curvature of the ρ - T lines. We observe that this t'-dependent curvature persists under strain, i.e., the curvature changes from positive (concave up like $+T^2$) to negative (convex up like $-T^2$) as t'/t is varied upward.

Recall that strain is effectively a small change in the hopping parameter, so we ought to expect strain to change thet' dependence of the curvature only quantitatively but not qualitatively. Phenomenologically, varying t' signals a change in the effective Fermi temperature scale T_{FL} where for $T < T_{FL}$ the system is in the Fermi liquid regime $\rho \propto T^2$ and hence has a positive curvature. Moreover, as we decrease t' from positive to negative, the Fermi liquid temperature regime is compressed into a smaller temperature regime down to temperatures where resistivity is usually hidden by the superconducting state. We want to focus on the crossover between Fermi liquid and strange metal which is covered by the following empirical relation

$$\rho \sim C \, \frac{T^2}{T_{FL} + T} \, . \tag{4.8}$$

Here C is a constant that defines the slope of the linear regime and T_{FL} marks the crossover from the Fermi-liquid regime. For example when $t' = -0.2t$ as found in typical hole-doped cuprates[6], we observe that a compressive strain extends the Fermi-liquid regime for the longitudinal resistivity, and flipping the strain reduces the Fermi-liquid regime. Qualitatively speaking, a compressive strain enhances the longitudinal hopping so that the effective interaction reduces relatively to the hopping. Likewise, a tensile strain increases the effective interaction in the unit of longitudinal hopping and suppresses the Fermi liquid temperature scale. Besides, we observe that a compressive strain suppresses the linear constant C while a tensile strain enhances it, as shown more obviously in Fig. 4.2 and Fig. 4.3. That can be verified in the experiment by measuring the slope of ρ - T for a *strange metal* under strain.

4.1.2 Susceptibilities for anisotropic resistivities

It has been argued [17] that cuprates are candidates for an electron nematic phase, in which nematic order might coexist with high temperature superconductivity, that is, the electronic system breaks a discrete rotational symmetry while leaving the translational symmetry intact. Here the normalized resistivity response plays the role of the order parameter in the phase transition. Since it is possible to experimentally

---

[6] In high T_c systems estimates give $t' \lesssim -0.27t$ Bi2212 and LSCO $t' \sim 0.16t$. We take $t' = -0.2t$ as a compromise between the two extremes.

identify continuous phases transitions through the observation of a diverging thermodynamic susceptibility when crossing a phase boundary, the temperature profile of elastoresistance (i.e., normalized resistivity response with respect to an arbitrary strain) is an interesting observable to explore. For that reason, we shall examine linear response function for the longitudinal and transverse components of the elastroresistivity tensor constructed in terms of the hopping strain as:

$$\chi_{XX} \equiv -\Big(\frac{\rho'_{xx} - \rho_{xx}}{\rho_{xx}}\Big)\Big/\Big(\frac{\delta t}{t}\Big) \ , \tag{4.9}$$

$$\chi_{YY} \equiv -\Big(\frac{\rho'_{yy} - \rho_{yy}}{\rho_{xx}}\Big)\Big/\Big(\frac{\delta t}{t}\Big) \ , \tag{4.10}$$

respectively. The susceptibility as defined is positive if compression along the x axis leads to a reduction of the resistivity in the specified direction. We note the connection of these susceptibilities with the nematic susceptibility Eq. (2.1) on using Eq. (3.25) as

$$\chi_{nem} = \alpha \lim_{\epsilon_{xx}\to 0} \chi_{XX}. \tag{4.11}$$

We compute the susceptibility for small values of strain $\delta t/t \gtrsim .05$. However, even these values of strain pick up some nonlinear components of the response function. These are also of interest, and we comment on these below.

The linear response function for strain-resistivity curves is plotted as a function of temperature in Fig. 4.2 and Fig. 4.3 for the longitudinal and transverse components at optimal density $n = 0.85$ for various t' and $\delta t/t$. Note that since the resistivity vanishes as $T \to 0$, there is an enhancement of the normalized susceptibility at low-T.

In Fig. 4.2, we see that the linear response function for the longitudinal resistivity χ_{XX} is mostly positive and shows non-linear (in $\delta t/t$) behavior at a fixed T(as can be identified by the separation of the strain curves) with respect to strain across the entire temperature range. This nonlinearity will be measured directly in Fig. 4.8 for $t' = -0.2$. The response function for $T \gtrsim 100\text{K}$ is highly ordered in that varying the strain from positive (compressive) to negative (tensile) increases the strength of the response function for all t'. Conversely as we cool the system, we observe that strain dependence of the response function becomes increasingly nonlinear, i.e., showing a wider separation between strain curves, the forms of which are strongly t' dependent. Now if we vary t' to survey the range of cuprate materials, we find at low T for hole-like ($t' < 0$) materials a significant enhancement in and an inversion of the strain dependence that is absent in electronlike ($t' > 0$) materials, though for both material types the strength of the response function remains approximately invariant at high-T.

We next discuss the transverse linear response function χ_{YY} shown in Fig. 4.3. This response is potentially interesting since the effects of strain on the band structure are found to play a less significant role, hence the correlation effects dominate. We find that the features of transverse response function are different from that of the longitudinal response function mainly in two ways: (1) the χ_{YY} collapses at high-T, showing strong linearity with respect to the strain and (2) it changes sign from negative to positive as we vary t'/t across 0.2 from below, consistent with Fig. 4.1. Measurements confirming this linear behavior and sign change would be potentially interesting results.

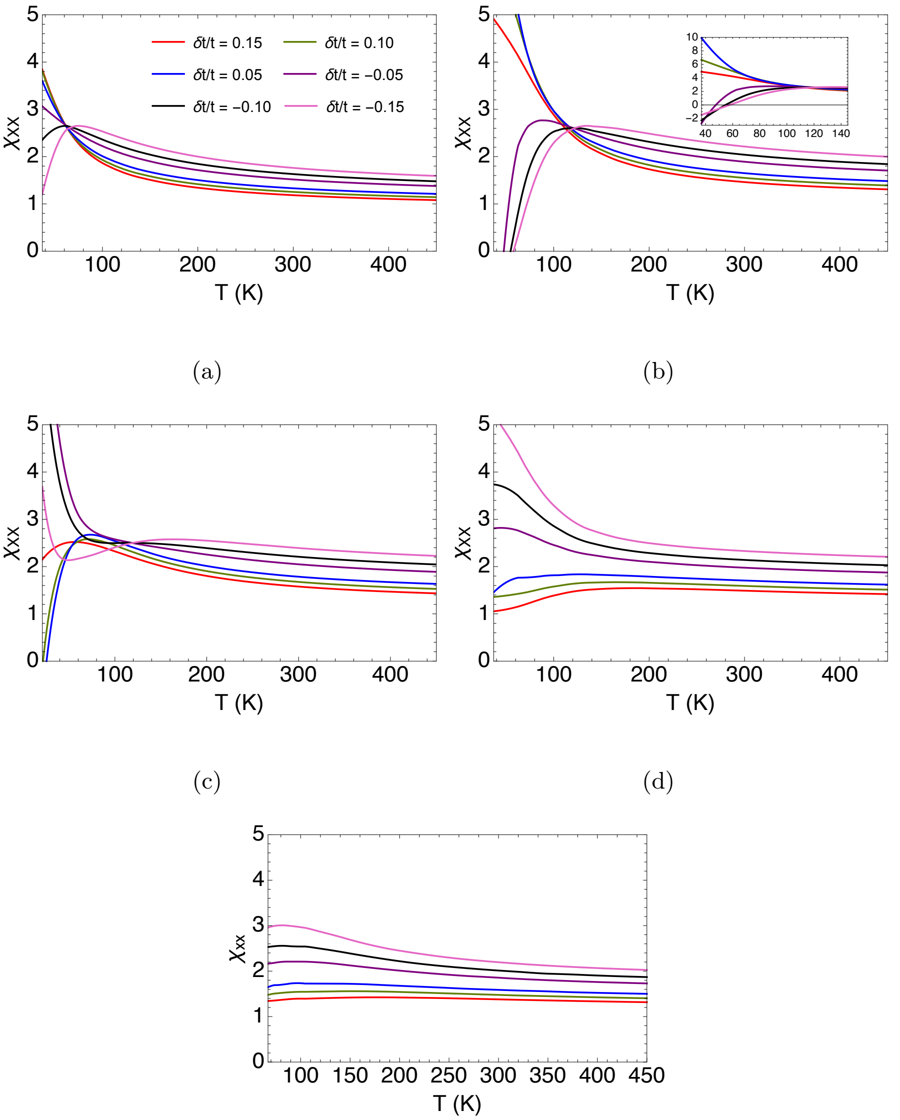

(a) (b) (c) (d) (e)

Figure 4.2: The longitudinal [Section 4.1.2] strain-resistivity susceptibilities versus temperature at filling $n = 0.85$, for various t' and $\delta t/t$. (a) $t'/t = -0.4$ (b) $t'/t = -0.2$, (c) $t'/t = 0.0$, (d) $t'/t = 0.2$, (f) $t'/t = 0.4$. All figures share a legend. For various $\delta t/t$, the susceptibilities χ_{xx} for $T \gtrsim 100$ approach each other in two sets, one for $\delta t/t > 0$ and another slightly displaced set for $\delta t/t < 0$. They splay apart at low T thus displaying strong nonlinearity in the Fermi liquid regime.

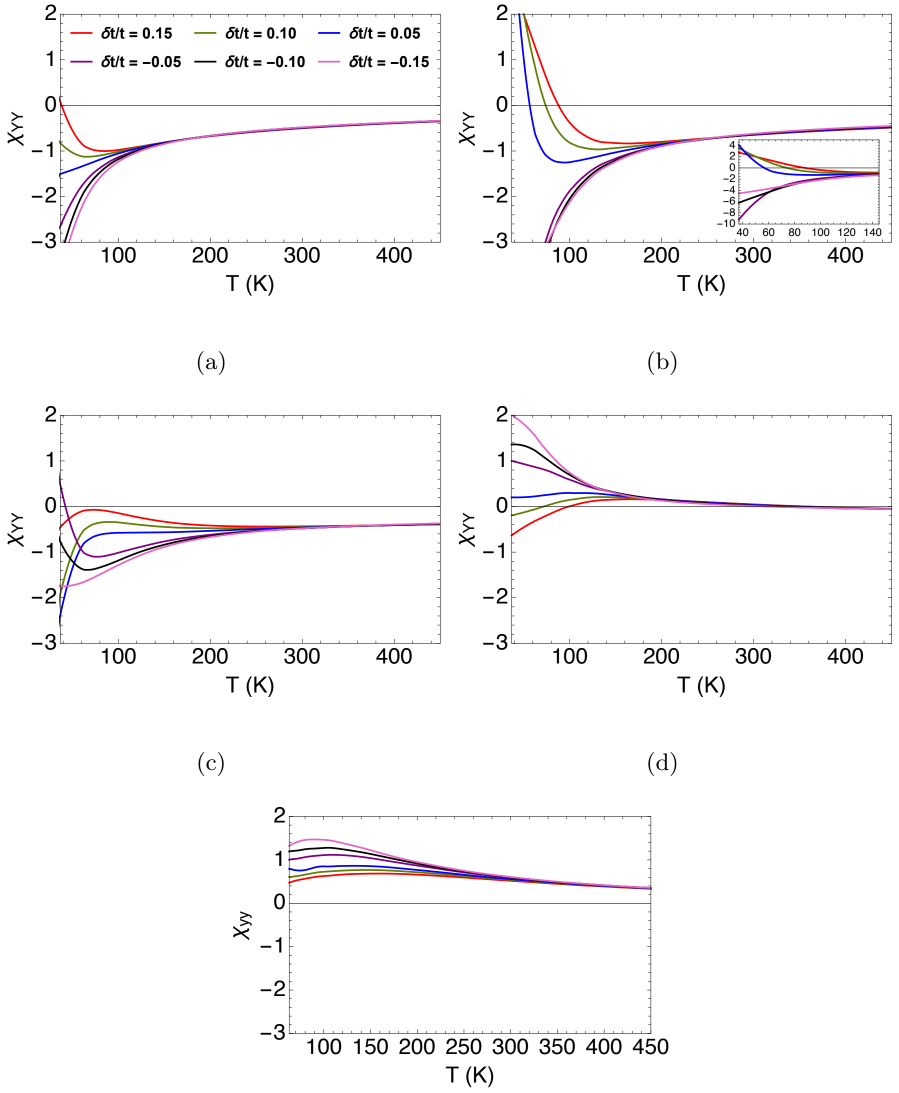

(a)

(b)

(c)

(d)

(e)

Figure 4.3: The transverse [Section 4.1.2] strain-resistivity susceptibilities versus temperature at filling $n = 0.85$, for various t' and $\delta t/t$. (a) $t'/t = -0.4$ (b) $t'/t = -0.2$, (c) $t'/t = 0.0$, (d) $t'/t = 0.2$, (f) $t'/t = 0.4$. All figures share a legend. The susceptibilities χ_{yy} approach a single set for $T \gtrsim 100$ and splay apart for low T thus also displaying strong nonlinearity in the Fermi liquid regime.

4.1.3 The nematic susceptibility

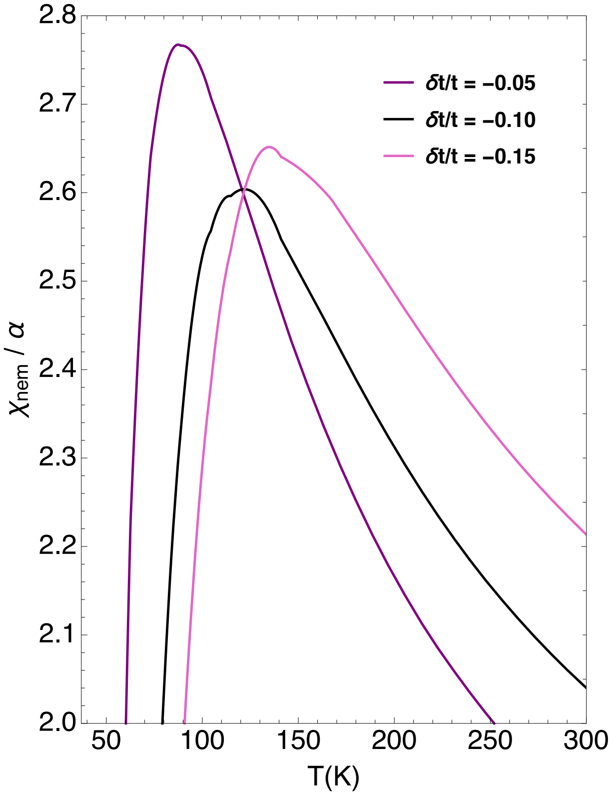

Figure 4.4: The nematic susceptibility computed using Eq. (4.12) for compressive strains of varying magnitude for $t' = -0.2t$, and $n = 0.85$. In the calculation of susceptibility, variation of $\delta t/t$ is approximately the same as variation in α at fixed strain ϵ_{xx}. This nematic susceptibility calculation can be directly compared with Fig. 2 of Ref. [41] where a piezoelectric device is used to measure the nematic susceptibility in Bi2212 at doping $\delta = 0.14$ and has a $T_C = 87$K. Unexpectedly the weight and intensity of T-profile is similar that of experimental measurements without any explicit mechanism to drive nematic fluctuations in the model. Here we approximate the exact formula $\chi_{nem} = \alpha \lim_{\epsilon_{xx}\to 0} \chi_{xx}$ using $\chi_{nem} = \alpha\chi_{XX}$.

In Fig. 4.4 we approximate the exact formula Eq. (2.1) using

$$\chi_{nem} = \alpha\chi_{XX} \ . \tag{4.12}$$

We calculate nematic susceptibility for compressive of varying magnitude. In this calculation of the nematic susceptibility, variation of $\delta t/t$ is approximately the same as variation of α at a fixed strain ϵ_{xx}. Unexpectedly, there are peak-like features in its temperature dependence and the weight and intensity of peaks are similar in magnitude to that of recent experimental observations (see Fig. 2 of Ref. [41]) of the nematic susceptibility in cuprate materials

4.1.4 Resistivity with non-zero J

In this section we examine the role of exchange parameter J (nearest neighbor exchange energy) on resistivity and the susceptibilities, setting $J = 0.17t$ which is the typical value for LSCO cuprate materials [55]. We take $J = t^2/U$ where U is the on site energy of the Hubbard model and U does not vary with strain and hence $\delta J = 2(\delta t/t)J$[3]. Now, if we turn on the exchange parameter J, we find that at low temperatures the resistivity is reduced by the exchange energy and at high temperatures the resistivity is slightly enhanced as seen in Figs. 4.5(a) and 4.5(b). In Figs. 4.5(c) and 4.5(d) we see the longitudinal and transverse susceptibility with exchange interaction is further enhanced at low temperatures whereas at higher temperatures the response is unchanged. The J effects are magnified in the low-T response since $\rho \to 0$ as $T \to 0$. We can say the effects of J on the response are negligible at high-T.

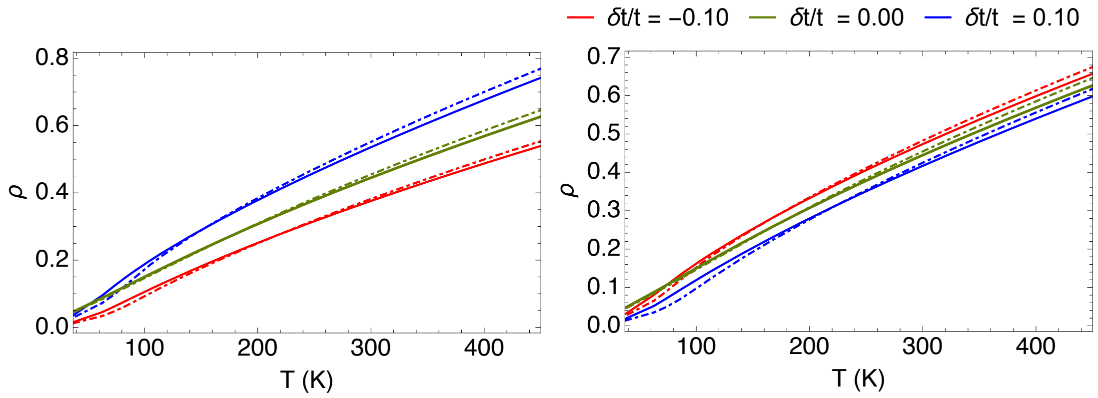

(a) Longitudinal (b) Transverse

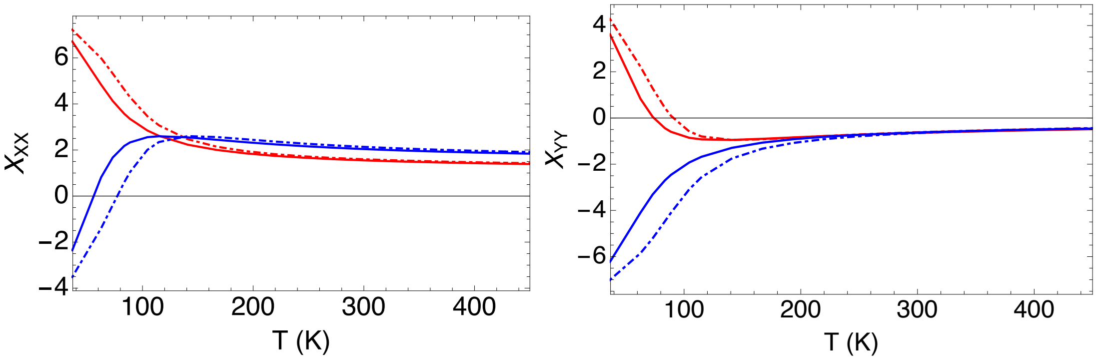

(c) Longitudinal (d) Transverse

Figure 4.5: The strain-induced resistivity for the (a) longitudinal and (b) transverse components at optimal filling $n = 0.85$, $t'/t = -0.2$ for three representative strain types with exchange parameter $J = 0.0$ (solid) and $J = 0.17$ (dashed). The strain-resistivity susceptibility in (c) the longitudinal and (d) the transverse components for the same parameter set as above. All figures share a legend. We note that a nonvanishing J enhances somewhat the magnitude of the susceptibilities in the low temperature Fermi liquid regime.

4.1.5 Susceptibilities for A_{1g} and B_{1g} irreps

Experimentally, it is possible to identify the irrep to which the order parameter belongs by applying a strain with a particular irrep of strain and searching for a divergence in the temperature profile. In the case of uniaxial strain along the x axis the strain can be decomposed into the A_{1g} and B_{1g} irreps. In this section we examine the strain-resistivity linear response function for the A_{1g} and B_{1g} irreps defined in terms of the hopping strain as

$$\chi_{A_{1g}} \equiv -\Big(\frac{\rho'_{xx} + \rho'_{yy} - 2\rho_{xx}}{2\rho_{xx}}\Big)\Big/\Big(\frac{\delta t}{t}\Big) = \frac{\chi_{XX} + \chi_{YY}}{2} \ , \tag{4.13}$$

$$\chi_{B_{1g}} \equiv -\Big(\frac{\rho'_{xx} - \rho'_{yy}}{\rho_{xx}}\Big)\Big/\Big(\frac{\delta t}{t}\Big) = \chi_{XX} - \chi_{YY} \ , \tag{4.14}$$

respectively.

In Figs. 4.6 and 4.7 we present the normalized strain-resistivity response functions at optimal density $n = 0.85$ for various t' and $\delta t/t$. In this picture the A_{1g} and B_{1g} irreps play the roles of a center of mass coordinate and a relative coordinate, respectively. Together the two susceptibilities characterize the shift of in-plane resistivity as a result of an arbitrary in-plane strain. Recall that since the resistivity vanishes as $T \to 0$, the A_{1g} and B_{1g} susceptibilities are also enhanced at low T.

Examining the A_{1g} susceptibilities in Fig. 4.6(a), Fig. 4.6(b), Fig. 4.6(c), and Fig. 4.6(d), one important feature stands out, namely, that for $T \gtrsim 100$K the response function is positive for all t' and strains $\delta t/t$. This indicates that increasing a tensile (compressive) strain for $T \gtrsim 100$K enhances (suppresses) the average of the anisotropic resistivities.

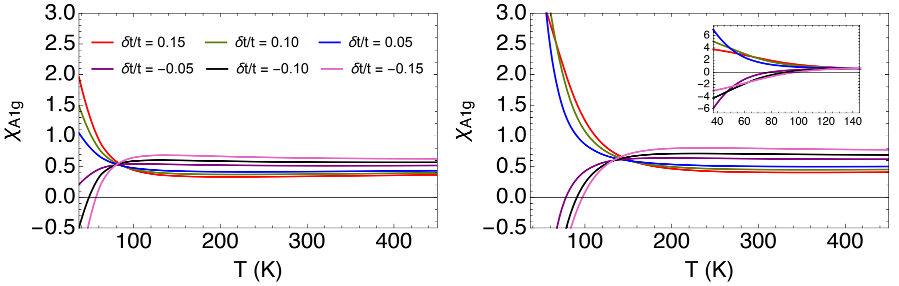

(a) $t'/t = -0.4$ (b) $t'/t = -0.2$

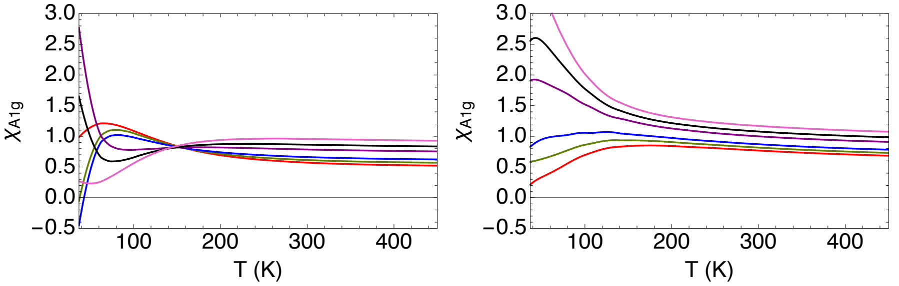

(c) $t'/t = 0.0$ (d) $t'/t = 0.2$

Figure 4.6: The normalized strain-resistivity susceptibilities from Eq. (4.13) versus T for the A_{1g} and B_{1g} irreducible representations at filling $n = 0.85$ at various t' and $\delta t/t$. (a), (c), (e), (g) $t'/t = -0.4, -0.2, 0.0, 0.2$ χ_{A1g}, respectively; (b), (d), (f), (h) $t'/t = -0.4, -0.2, 0.0, 0.2$ χ_{B1g}, respectively; All the figures share a legend. For various $\delta t/t$, and for $T \gtrsim 100$ all the susceptibilities approach each other in two sets, one for $\delta t/t > 0$ and another slightly displaced set for $\delta t/t < 0$. They splay apart at low T thus displaying strong nonlinearity in the Fermi liquid regime.

We also see that at $T \sim 100$K with hole doping, i.e., $t' \leq 0$, the normalized susceptibilities become independent of the strain, and hence the response is in the linear regime (signaled by the convergence of all strain curves). The nonlinear response at lower T is interesting and potentially observable in experiments with varying strain. On the other hand for electron doping, i.e., $t' > 0$, we see nonlinear behavior even at high T. Its origin is the extended Fermi-liquid regime which has a higher crossover temperature scale. Summarizing, we find that the early departure from Fermi liquid behavior into a

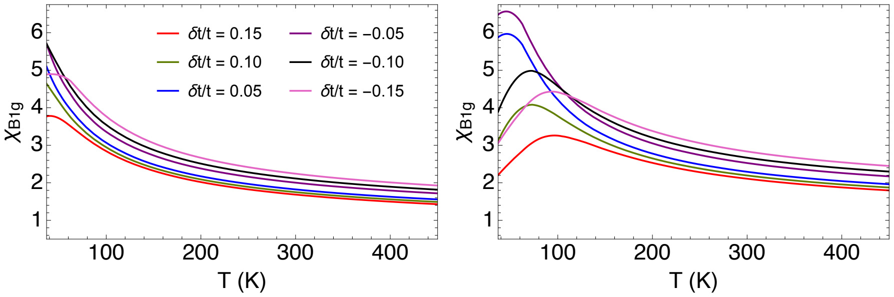

(a) $t'/t = -0.4$ (b) $t'/t = -0.2$

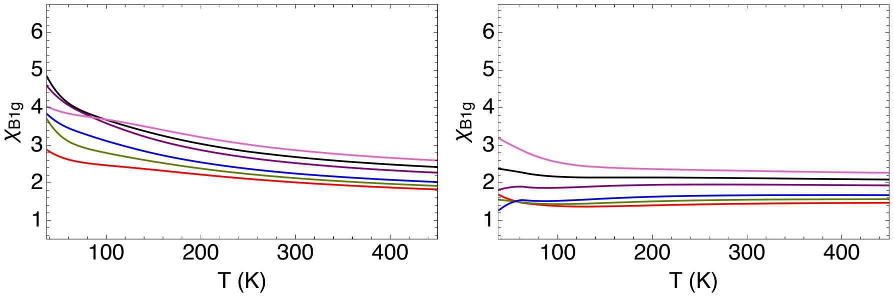

(c) $t'/t = 0.0$ (d) $t'/t = 0.2$

Figure 4.7: The normalized strain-resistivity susceptibilities from Eq. (4.13) versus T for the B_{1g} irreducible representations at filling $n = 0.85$ at various t' and $\delta t/t$. (a), (b), (c), (d) $t'/t = -0.4, -0.2, 0.0, 0.2$; All the figures share a legend. See caption of Fig. 4.6 for common details.

strange metallic behavior in the hole doping favors an apparent linear response above 100K due to a change in scale. Conversely we expect to see nonlinearity extending to much higher T's in electron-doped systems.

From Fig. 4.6, we observe that the B_{1g} susceptibilities for $T < 100$K are strongly dependent on the value of t' of the system. We find in hole-like materials ($t' \lesssim 0.0$) there is a strong enhancement (the details of which depend on the $\delta t/t$) in the susceptibility at low-T. In contrast, this feature is absent in electron-like materials ($t' > 0.0$) where there is weaker correlation, higher T_{FL}, and hence stronger quasiparticles.

Focusing on the strain dependence, we see that at high-T the susceptibilities are relatively insensitive to t' and generally increases as we vary from a compressive to a tensile strain. There is also asymmetry in rate of change of susceptibilities between a compressive and tensile strain as $|\delta t/t|$ is varied, i.e., the response function changes more rapidly for tensile than compressive strains. Therefore the degree of anisotropy is higher for tensile strain than compressive strains of equal magnitude.

Also, the B_{1g} curves under compressive strain ($\delta t/t > 0$) are closer to each other than those under tensile strain for electron-doped systems, yet this spacing difference is less obvious in the hole-doped case. It means that a tensile response tends to show stronger nonlinearity, especially in electron-doped systems.

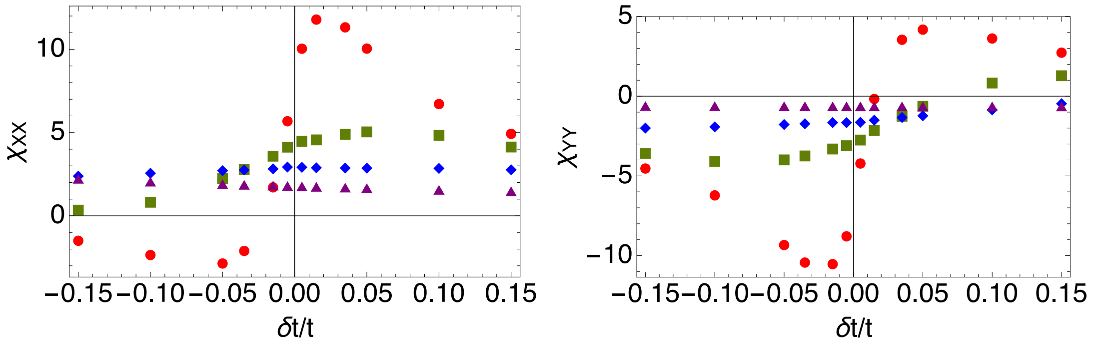

(a) XX (b) YY

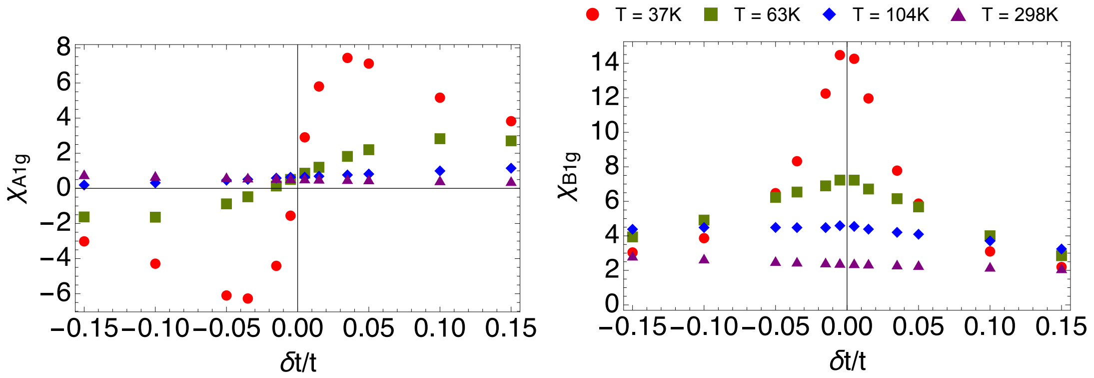

(c) A_{1g} (d) B_{1g}

Figure 4.8: The strain-resistivity susceptibilities for various symmetries as a function of strain $\delta t/t$ at filling $n = 0.85$ and $t'/t = -0.2$. (a) XX, longitudinal, Section 4.1.2; (b) YY, transverse, Section 4.1.2; (c) A_{1g} irrep, Eq. (4.13); (d) B_{1g} irrep, Eq. (4.14). The susceptibilities are relatively strain independent above 100K but show strong nonlinearity at low T. It is noteworthy that for the lowest T shown, the susceptibilities $\chi_{xx}, \chi_{yy}, \chi_{A_{1g}}$ change sign at or close to $\delta t/t = 0$. At higher T this change of sign is lost. The behavior of the nematic susceptibility $\chi_{nem} = \lim_{\epsilon_{xx}\to 0}(\alpha\chi_{xx})$ at low T has thus the potential for a change of sign, depending on how we choose a sufficiently small $|\epsilon_{xx}|$ or $|\delta t/t|$ for the purpose of taking the limit $\lim_{\epsilon_{xx}\to 0}$.

4.1.6 Susceptibilities versus strain

In Fig. 4.8, we display the strain-resistivity response functions versus hopping strain for various symmetries at $t' = -0.2t$ and $n = 0.85$ (which is roughly the parameter set for LSCO cuprate material[6] at optimal density) at four representative temperatures.

Here we approximate the variance in the linear response function as follows

$$\chi(T) = c_0(T) + c_1(T)(\delta t/t) + c_2(T)(\delta t/t)^2 + \dots \,. \tag{4.15}$$

In panels (a) and (b) we have longitudinal and transverse linear response functions, respectively, showing nonlinear behavior at low temperature which becomes more linear (as indicated by horizontal line) as the system warms. This nonlinear behavior at low T can be understood as a result of the increasing importance of correlations as the system is cooled. Although the longitudinal and transverse response functions differ considerably in magnitude, the curves are approximately symmetric under inversion of the axes. In panels (a), (b), and (c) there is a wave-like oscillation which indicates the presence of higher order terms, e.g., the $T = 37$K curve in panel (a) appears to have $(\delta t/t)^3$ term competing with a linear term. Another interesting result we find is that as the system cools the B_{1g} response function appears to diverge at $\delta t/t = 0$ as $T \to 0$ suggests that any deviation from the point group symmetry of the square lattice produces a finite resistivity response.

4.2 Kinetic Energy for an x-axis strain

In this section we explore the kinetic energy anisotropy induced by strain along the x-axis using ECFL theory. Since the anisotropic kinetic energy can be related to measurements of the optical conductivity using the f-sum rule on the t-t'-J model, this makes it another interesting observable to explore.

The total kinetic energy for a system under strain is computed as

$$K_{\text{tot}} = \left\langle \int_{-\infty}^{\infty} \rho_{\mathcal{G}}(\vec{k},\omega)\epsilon_{\vec{k}} d\omega \right\rangle_k . \tag{4.16}$$

This may be decomposed as follows:

$$K_{\text{tot}} = K_{xx} + K_{yy} + K_{xy}, \tag{4.17}$$

where the cross kinetic energy K_{xy} comes from the second neighbor interactions and is related to the dynamic Hall conductivity. The longitudinal, transverse and cross kinetic energies are given by

$$K_{xx} = \left\langle \int_{-\infty}^{\infty} d\omega \rho_{\mathcal{G}}(\vec{k},\omega)\epsilon_{k_x} \right\rangle_k \tag{4.18}$$

$$K_{yy} = \left\langle \int_{-\infty}^{\infty} d\omega \rho_{\mathcal{G}}(\vec{k},\omega)\epsilon_{k_y} \right\rangle_k \tag{4.19}$$

$$K_{xy} = \left\langle \int_{-\infty}^{\infty} d\omega \rho_{\mathcal{G}}(\vec{k},\omega)\epsilon_{k_{xy}} \right\rangle_k \tag{4.20}$$

where

$$\epsilon_{k_x} = -2t_x \cos(k_x a) \tag{4.21}$$

$$\epsilon_{k_y} = -2t_y \cos(k_y b) \tag{4.22}$$

$$\epsilon_{k_{xy}} = -4t_d \cos(k_x a)\cos(k_y b) . \tag{4.23}$$

In the t-t'-J model the anisotropic kinetic energies K_α, where $\alpha = xx$, yy, and xy, are related to the optical conductivity σ_α by the following sum rule

$$\mathrm{Re}\int_0^\infty \sigma_\alpha(\omega)d\omega = -K_\alpha e^2 \ , \tag{4.24}$$

where e is the electrical charge. $K_\alpha e^2$ sets the scale of the optical conductivity, i.e.,

$$-\frac{1}{K_\alpha e^2}\mathrm{Re}\int_0^\infty \sigma_\alpha(\omega)d\omega = 1 \ . \tag{4.25}$$

The optical conductivity in the DC limit $\sigma_\alpha(0)$ relates to the DC resistivity as follows: $\rho_\alpha(0) = 1/\sigma_\alpha(0)$. For the anisotropic kinetic energy, we calculate and quote the following objects:

- K'_{xx} is the strained version of longitudinal kinetic energy.
- K'_{yy} is the strained version of transverse kinetic energy.
- We call K_{xx} without a prime the tetragonal result. It is the same as K_{yy}.
- We present A_{1g} :
  $$-\frac{K'_{xx} + K'_{yy} - 2K_{xx}}{2K_{xx}(\delta t/t)} \text{ vs } T$$
- We present B_{1g} : $-(K'_{xx} - K'_{yy})/(K_{xx}\delta t/t)$ vs T

4.2.1 Raw kinetic energies

From Eq. (4.18) we calculate the anisotropic kinetic energies K_α as a function of temperature at optimal density for a representative range of cuprate materials t' and hopping strains $\delta t/t$ as shown in Fig. 4.9. The main observation is that a compressive

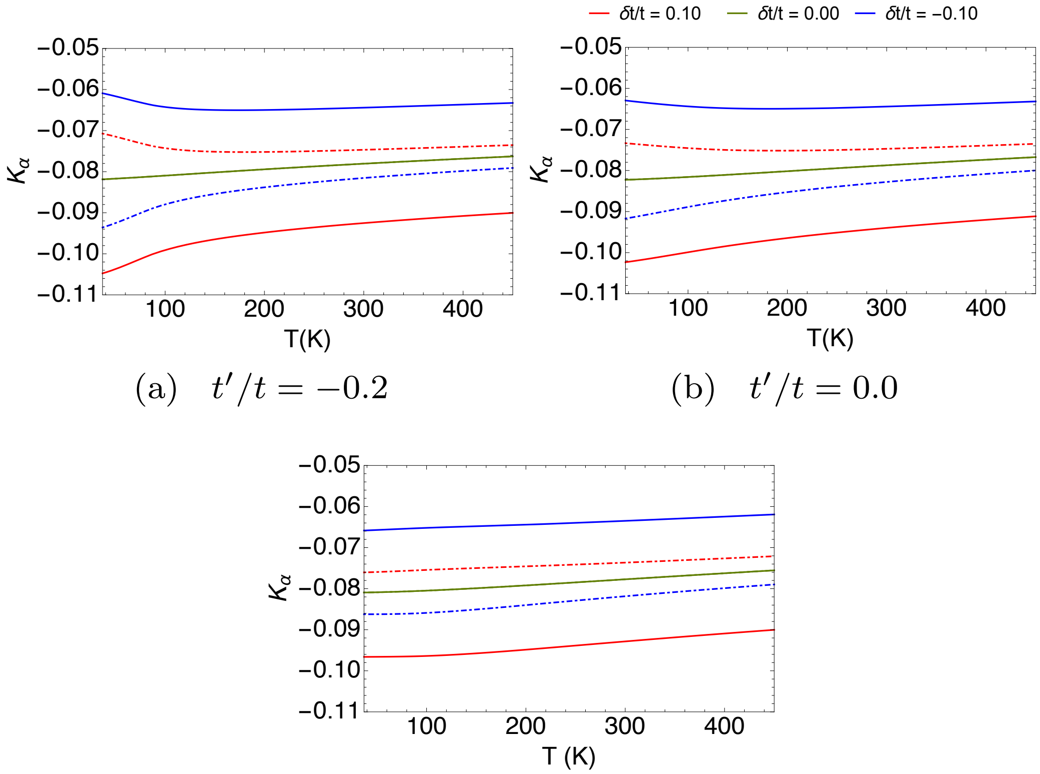

(a) $t'/t = -0.2$

(b) $t'/t = 0.0$

(c) $t'/t = 0.2$

Figure 4.9: Anisotropic kinetic energies K_α versus T for K_{xx} (solid) and K_{yy} (dashed) at filling $n = 0.85$, for various t' and at three representative strains: compressive strain, no strain, and tensile strain. Note that $K_{xx} = K_{yy}$ in the absence of strain. (a) $t'/t = -0.2$, (b) $t'/t = 0.0$, (c) $t'/t = 0.2$. All figures share a legend.

(tensile) strain suppresses (enhances) the longitudinal kinetic energy and vice versa for the transverse kinetic energy response with a smaller magnitude of variation. The variation in the longitudinal kinetic energy can be understood as a combination of changes in the band structure parameter t_x and correlations. On the other hand, the transverse kinetic energy is dominated by changes to the correlation function since the parameter t_y is unmodified by x-axis strain. There is little T-dependence with the exception of a slight broadening of the range of the response at low-T as the T_{FL} is reduced. The t' dependence is also weak because K_{xx} and K_{yy} do not explicitly depend on t' but through the spectral function.

4.2.2 Strain-kinetic-energy susceptibilities

In analogy with elastoresistance, we compute the so-called normalized strain-kinetic-energy response function, which measures the change in kinetic energy with respect to a strain. We shall focus on the normalized strain-kinetic-energy response functions for the A_{1g} and B_{1g} irrep since measurements of these symmetries are sensitive to a break in the fourfold rotation symmetry of a square lattice. Explicitly the response functions are defined in terms of hopping strain as

$$M_{A_{1g}} \equiv -\Big(\frac{K'_{xx} + K'_{yy} - 2K_{xx}}{2K_{xx}}\Big)\Big/\Big(\frac{\delta t}{t}\Big) \,, \tag{4.26}$$

$$M_{B_{1g}} \equiv -\Big(\frac{K'_{xx} - K'_{yy}}{K_{xx}}\Big)\Big/\Big(\frac{\delta t}{t}\Big) \,, \tag{4.27}$$

where the sign is imposed so that susceptibility defined in terms of hopping strain matches its counterpart defined in terms of conventional strain. Fig. 4.10 displays the normalized strain-kinetic-energy susceptibilities as a function of temperature for the A_{1g} and B_{1g} irrep at optimal density for various t' and $\delta t/t$.

The A_{1g} irrep susceptibility signals a change in the sum of anisotropic kinetic energies $K_{xx} + K_{yy}$ with respect to the hopping change. The A_{1g} susceptibility shows that tuning the strain from tensile to compressive increases rather uniformly the magnitude of the anisotropic kinetic energy, i.e., strain enhances the overall optical weight from Eq. (4.24).

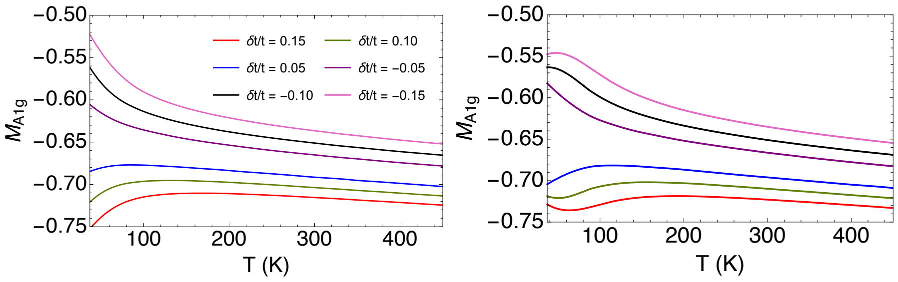

(a) $t'/t = -0.4$ (b) $t'/t = -0.2$

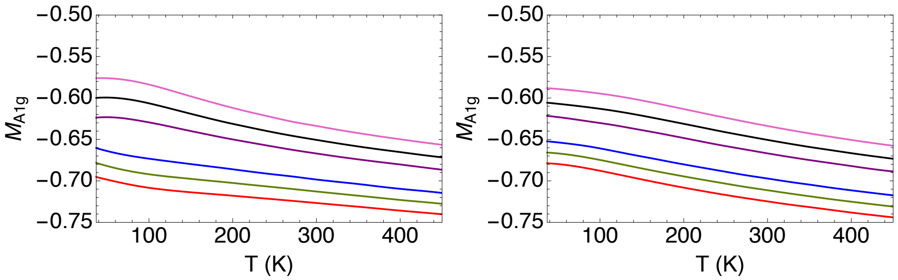

(c) $t'/t = 0.0$ (d) $t'/t = 0.2$

Figure 4.10: The normalized strain-kinetic-energy susceptibilities vs T for the A_{1g} irrep as defined in Eq. (4.26) at filling $n = 0.85$, for various t' and $\delta t/t$. (a) $t'/t = -0.4$, (b) $t'/t = -0.2$, (c) $t'/t = 0.0$, (d) $t'/t = 0.2$. All figures share a legend.

The B_{1g} susceptibility is characterized as the difference in the kinetic energies $K_{xx} - K_{yy}$ with respect to the hopping change. Thus a nonzero value for the B_{1g} irrep signals an anisotropy between the two directions. We observe that the response function for the B_{1g} irrep is strongly t' dependent. For $t' = -0.4$, the response functions is nearly linear at all temperatures. We point out a curious feature for the $t' = -0.2$ curve where at high-T the system is linear whereas at low-T the system is nonlinear, but it is nearly symmetric with respect to a compressive or tensile strain of similar magnitude. At high-T for all t' the system is monotonic with respect to strain. For $t' \geq 0$ there is little variation in the response function across the temperature range and it appears to

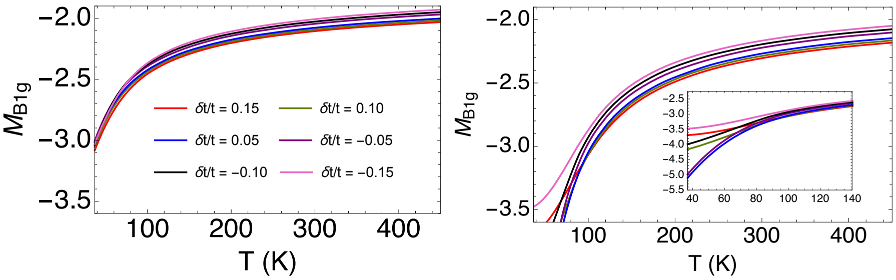

(a) $t'/t = -0.4$ (b) $t'/t = -0.2$

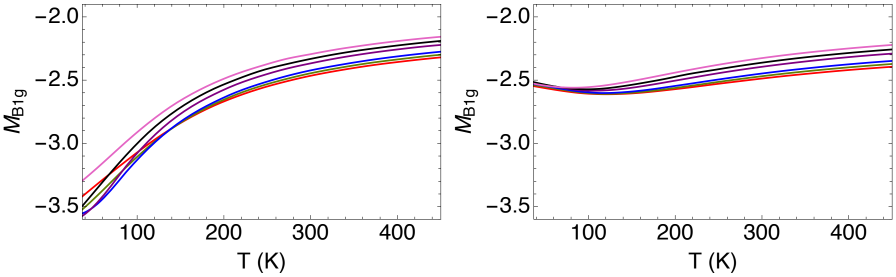

(c) $t'/t = 0.0$ (d) $t'/t = 0.2$

Figure 4.11: The normalized strain-kinetic-energy susceptibilities vs T for the B_{1g} irrep as defined in Eq. (4.27) at filling $n = 0.85$, for various t' and $\delta t/t$. (a) $t'/t = -0.4$, (b) $t'/t = -0.2$, (c) $t'/t = 0.0$, (d) $t'/t = 0.2$. All figures share a legend.

become increasingly nonlinear as the system is warmed due to the reduction in the scale of variation.

4.2.3 Strain-kinetic-energy susceptibility versus strain

We now present strain-kinetic-energy susceptibility as a function of strain at optimal density ($n = 0.85$) and $t' = -0.2t$ for XX, YY, A_{1g}, B_{1g} symmetries at various T (see Fig. 4.12), where we define the longitudinal and transverse response functions as

$$M_{XX} \equiv -\Big(\frac{K'_{xx} - K_{xx}}{K_{xx}}\Big) \Big/ \Big(\frac{\delta t}{t}\Big)\,, \tag{4.28}$$

$$M_{YY} \equiv -\Big(\frac{K'_{yy} - K_{yy}}{K_{xx}}\Big) \Big/ \Big(\frac{\delta t}{t}\Big)\,. \tag{4.29}$$

respectively. Like the resistivity case, $M_{A_{1g}} = 0.5 \times (M_{XX} + M_{YY})$ and $M_{B_{1g}} = M_{XX} - M_{YY}$.

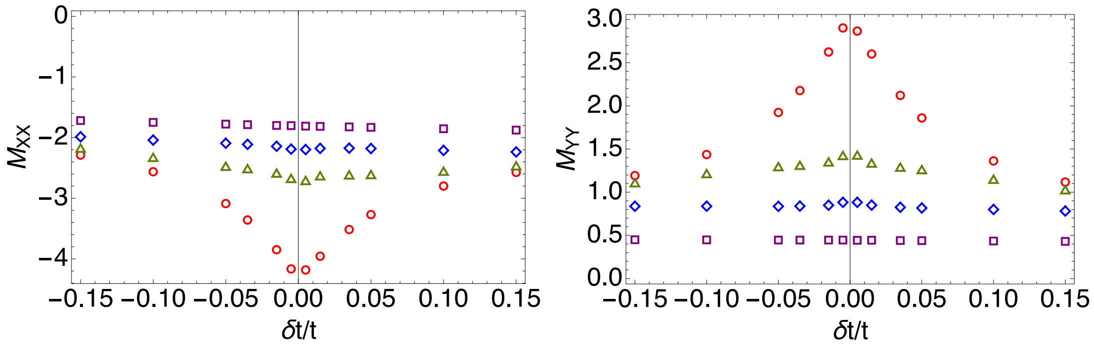

(a) XX (b) YY

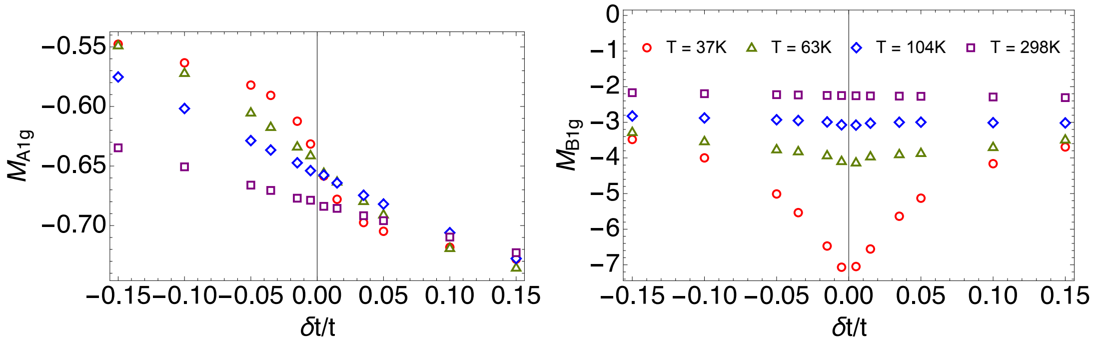

(c) A_{1g} (d) B_{1g}

Figure 4.12: The strain-kinetic-energy susceptibilities versus $\delta t/t$ at filling $n = 0.85$ and $t'/t = -0.2$ at four representative temperatures. All figures share a legend. (a) XX, longitudinal, Eq. (4.28); (b) YY, transverse, Eq. (4.29); (c) A_{1g} irrep, Eq. (4.26); (d) B_{1g} irrep, Eq. (4.27).

We find that at low temperatures, decreasing the magnitude of the strain increases the strength of the longitudinal response function in panel (a) and the response function is symmetric with respect to both strain types. The transverse response function in panel (b) shows a similar symmetry between tensile and compressive strains with a flipped sign. Therefore we find that a compressive strain for the A_{1g} response function [panel (c)] depletes the in-plane optical weight and vice versa for a tensile strain. The B_{1g} response function is similar to the longitudinal and transverse, only more intensive and it signals an enhanced (suppressed) anisotropy between in-plane kinetic energies for compressive (tensile) strains. In all cases the response function is approximately linear at room temperature (297K) and becomes increasingly nonlinear as the system cools. In comparing panels (b)–(d) we see strong similarity between their respective responses. This is expected since strain merely shifts kinetic energy versus temperatures curves up and down. Also, it appears to diverge for small strains as $T \to 0$.

4.3 The local density of states for an x-axis strain

The local density of states (LDOS) is also very interesting since it can be measured using STM probes. We present results on how the LDOS changes with strain, and the related susceptibilities. We argue that if experiments are done on resistivity variation as well as LDOS variation with strain, we can bypass the need for measuring strain accurately and of estimating the parameter α in Eq. (3.16). The LDOS is calculated as $\rho_{G\mathrm{loc}}(\omega) = \langle \rho_G(\vec{k}, \omega) \rangle_k$ where averaging over the Brillouin zone is implied, and $G \to g$ is the free Green's function (i.e., band structure) which gives the bare LDOS and the ECFL Green's function $G \to \mathcal{G}$ gives the LDOS for the t-t'-J model.

In this section we calculate the normalized change in the local density of states and quote the following:

- $\rho'_{g\mathrm{loc}}(\omega) = \langle \rho_g(\vec{k}, \omega) \rangle_k$ is the bare LDOS for a strain along the x axis.

- $\rho'_{\mathcal{G}\mathrm{loc}}(\omega) = \langle \rho_{\mathcal{G}}(\vec{k}, \omega) \rangle_k$ is the interacting LDOS for an x axis strain.

- $\rho_{g\mathrm{loc}}$ without a prime refers to the tetragonal result and similarly for $\rho_{\mathcal{G}\mathrm{loc}}$.

- We present $(\rho'_{g\mathrm{loc}} - \rho_{g\mathrm{loc}})/(\rho_{g\mathrm{loc}} \delta t/t)$ vs ω.

- We present $(\rho'_{\mathcal{G}\mathrm{loc}} - \rho_{\mathcal{G}\mathrm{loc}})/(\rho_{\mathcal{G}\mathrm{loc}} \delta t/t)$ vs ω.

4.3.1 T variation

In Fig. 4.13, we display the LDOS at optimal density ($n = 0.85$) and $t' = -0.2$ for various temperatures at three characteristic strains: a compressive strain (thick dashed), unstrained (solid) and tensile strain(thin dashed). We compare the LDOS for a non-interacting system [panel (a)] to a system with electron-electron interaction [panels (b)-(d)]. We find over large temperature scales that curves for the bare LDOS shifts to the left along the ω spectrum upon warming, leaving the line shape intact. In contrast with the bare LDOS, we see that warming the LDOS for the interacting system in panel (c) completely smooths and broadens the LDOS peaks for all strains and slightly shifting them left. This is consistent with previous findings that interactions significantly lower the Fermi liquid temperature T_{FL} [65]. We note that strain inverts the LDOS peak at low T, leaving behind a pair of cusps at a reduced height. This is an artifact of the anisotropy of hopping parameters since it also shows up in the bare case.

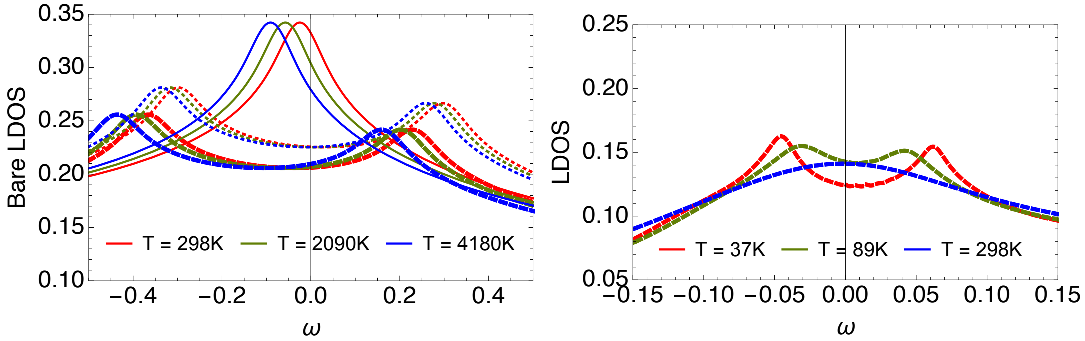

(a) bare LDOS (b) LDOS, $\delta t/t = 0.15$

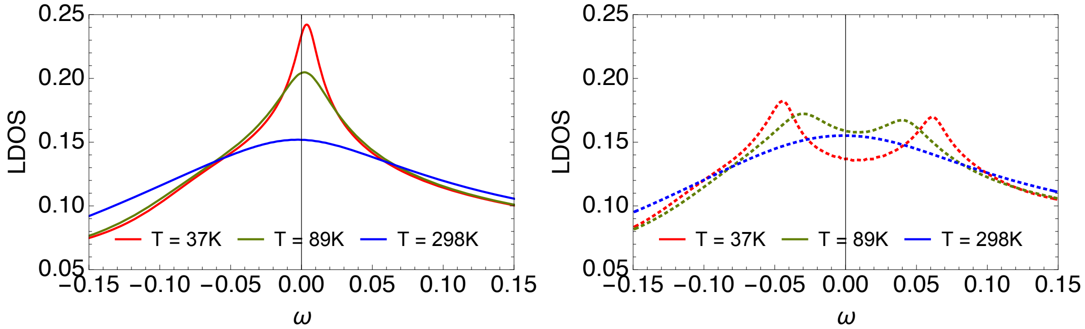

(c) LDOS, $\delta t/t = 0.00$ (d) LDOS, $\delta t/t = -0.15$

Figure 4.13: The local density of states for (a) the noninteracting (band-structure) and (b)-(d) interacting system (t-J model) at optimal filling ($n = 0.85$), $t' = -0.2$t, for various temperatures and at three characteristic strains: $\delta t/t = 0.15, 0.00, -0.15$ (thick dashed, solid, thin dashed).

4.3.2 J variation

In Fig. 4.14, we turn on the exchange parameter J and examine the LDOS. We also find it useful to examine the self-energy of the system. We define the Dyson self-energy Σ as

$$\mathcal{G}(k) = \frac{1}{\omega + \boldsymbol{\mu} - \epsilon_{\vec{k}} - \Sigma(k)} \,. \tag{4.30}$$

Here we use the shorthand $\Sigma = \Sigma' + i\Sigma''$ to denote the real and imaginary parts of a complex function. In terms of the spectral function, self-energy imaginary part is

$$\Sigma''(k) = \frac{-\pi\rho_{\mathcal{G}}(k)}{[\mathcal{G}'(k)]^2 + [\pi\rho_{\mathcal{G}}(k)]^2} \, , \tag{4.31}$$

where $\mathrm{Re}\,\mathcal{G} = \mathcal{G}'$ is found by taking the Hilbert transform of $\mathrm{Im}\,\mathcal{G} = \mathcal{G}''$ and we can find Σ' in the same manner. In Figs 4.14 (c)-(f) we display the Dyson self-energy averaged over the Brillouin zone $\Sigma_{\mathrm{loc}}(\omega) = \langle\Sigma(\vec{k}, \omega)\rangle_k$.

Turning on the exchange parameter in Fig. 4.14 (a) has a small, but visible effect on LDOS at low-ω. For panel (c) we see that varying strain from compressive ($\delta t/t > 0$) to tensile ($\delta t/t < 0$) shifts the average quasiparticle states to higher energies and panel (e) shows that increasing the intensity of the strain produces quasiparticles with higher and sharper peaks. In panels (b),(d), and (f) we see that varying J from ferromagnetic (negative) to antiferromagnetic (positive) splits a single LDOS peak into two, shifts the average quasiparticle states to higher energies, and narrows the quasiparticle peaks.

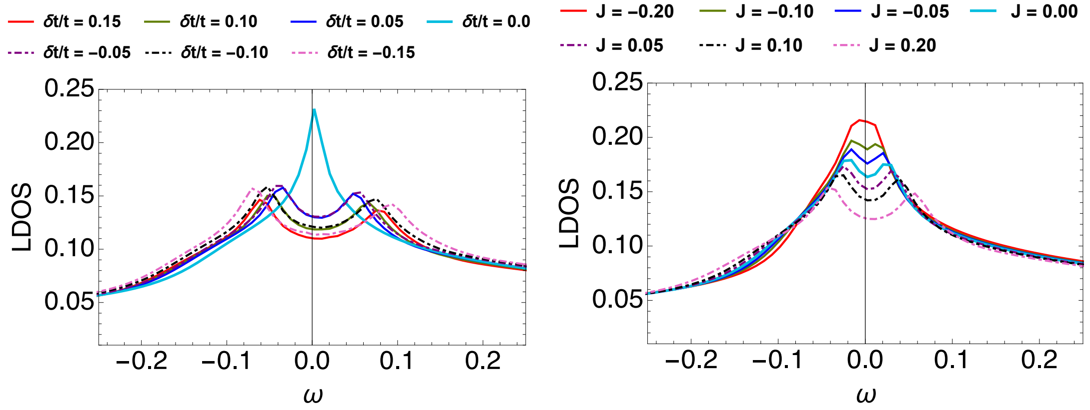

(a) $J = 0.17t$ (b) $\delta t/t = 0.05$

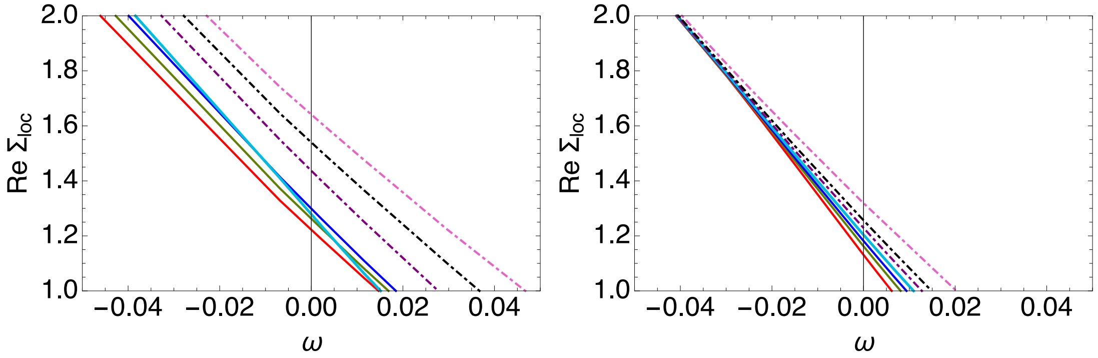

(c) $J = 0.17t$ (d) $\delta t/t = 0.05$

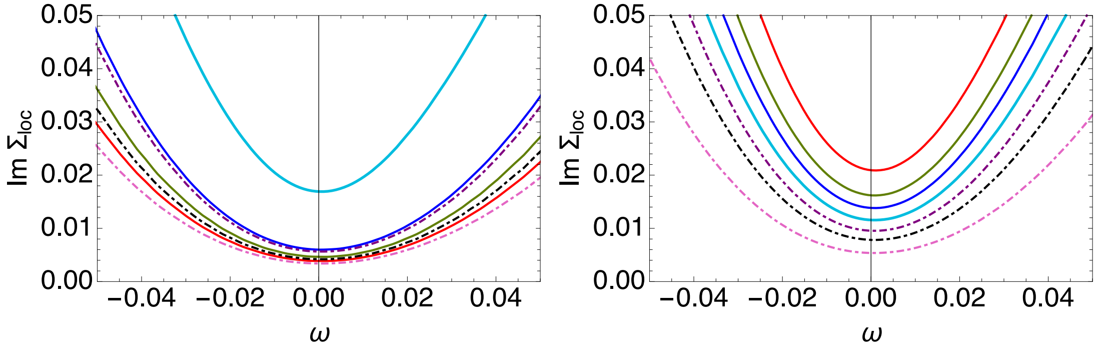

(e) $J = 0.17t$ (f) $\delta t/t = 0.05$

Figure 4.14: (a),(b) The LDOS; (b),(c) real part of local Dyson self-energy; (e),(f) the imaginary part of local Dyson self-energy for parameter set $n = 0.85$, $T = 37\text{K}$, $t' = -0.2t$ with varying $\delta t/t$ (LHS) and varying J (RHS). Figures (a),(c), and (e) and (b),(d), and (f) share a legend, respectively.

4.3.3 t' variation

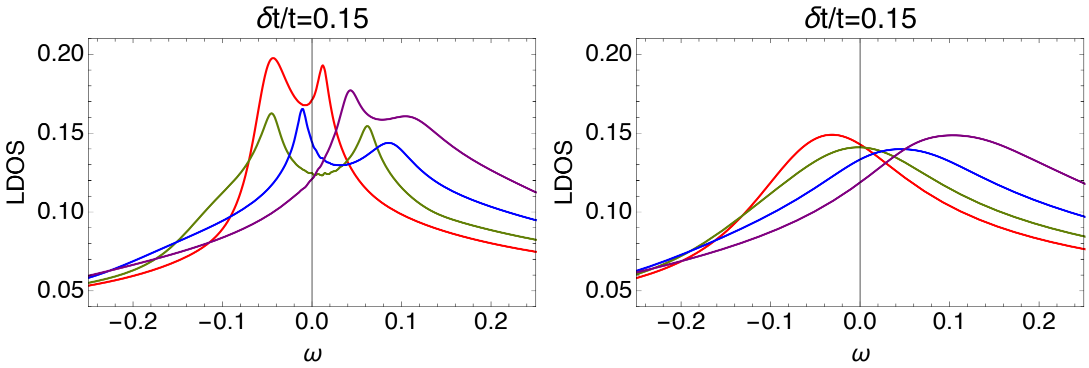

(a) $T = 37\text{K}$ (b) $T = 298\text{K}$

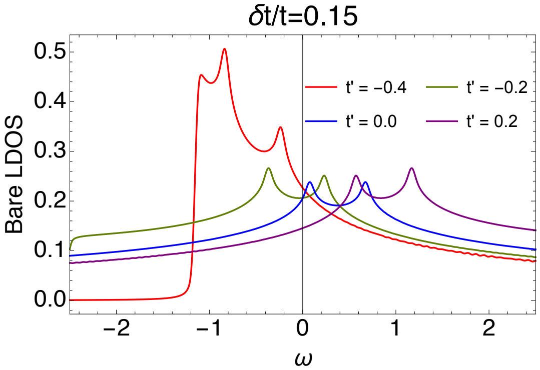

(c) $T = 298\text{K}$

Figure 4.15: The local density of states versus frequency at optimal filling ($n = 0.85$), for a compressive strain ($\delta t/t = 0.15$) at various t'. (a)-(b) The interacting system (t-t'-J model) at $T = 37\text{K}$ and $T = 298\text{K}$, respectively. (c) The non-interacting (band-structure) system at $T = 298\text{K}$. All figures share the same legend.

In Fig. 4.15, we examine the LDOS from a different vantage point by looking at the t' dependence for a system at optimal density ($n = 0.85$), for a compressive strain of $\delta t/t = 0.15$, at various t'/t. In panel (c), we show the bare LDOS at room temperature as a reference for the interacting system. In panels (a) and (b),we display interacting system at $T = 37\text{K}$ and $T = 298\text{K}$, respectively. Upon inspection it appears the primary role thatt' plays is to shift the energy band along the spectrum. As previously noted, warming the interacting system to room temperature smooths and broadens the characteristic LDOS peaks for all strain types and at all t' while leaving their position in the spectrum fixed. Even though the relative position of different t' curves remain unchanged as the interactions are turned on, we note that strong correlations renormalizes the bare band into a smaller energy region. Comparing panels (a) and (b) fixed at $t' = -0.4, -0.2$, we observe that LDOS peak height is more strongly suppressed at a lower t'. This is consistent with previous studies [65] on the unstrained interacting system, and it indicates that a smaller t' has a lower Fermi-liquid temperature scale and hence it is less robust to heating.

4.3.4 Susceptibilities versus frequency

Next, we examine the normalized response function of LDOS of the noninteracting and interacting system, respectively, defined as

$$N_g \equiv \left(\frac{\rho'_{g\mathrm{loc}} - \rho_{g\mathrm{loc}}}{\rho_{g\mathrm{loc}}} \right) \Big/ \left(\frac{\delta t}{t} \right) , \tag{4.32}$$

$$N_{\mathcal{G}} \equiv \left(\frac{\rho'_{\mathcal{G}\mathrm{loc}} - \rho_{\mathcal{G}\mathrm{loc}}}{\rho_{\mathcal{G}\mathrm{loc}}} \right) \Big/ \left(\frac{\delta t}{t} \right) . \tag{4.33}$$

In Fig. 4.16, we plot the LDOS susceptibility for a noninteracting and interacting system at room temperature at optimal density for various t'. We observe that the response function is linear at all frequencies except near the LDOS peak and, although not shown in the figure, at the band edges. Regardless of the presence of interaction, we note that the susceptibility is enhanced by tensile strain near the LDOS peak and reduced by a compressive strain.

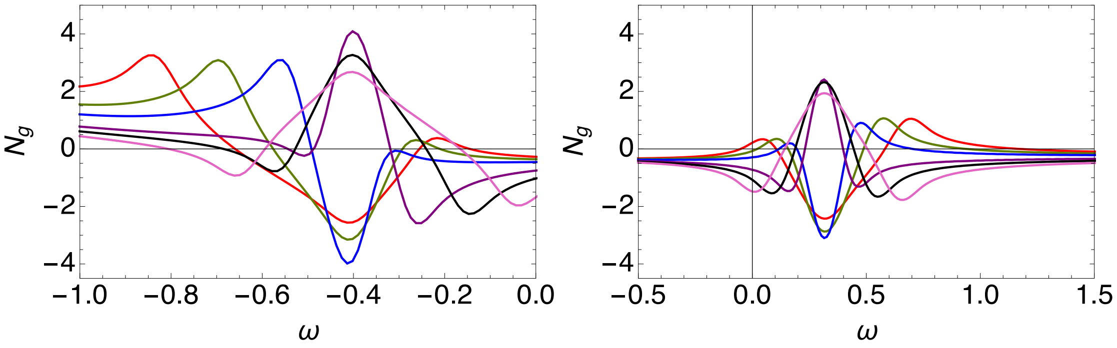

(a) $t'/t = -0.4$ (b) $t'/t = 0.0$

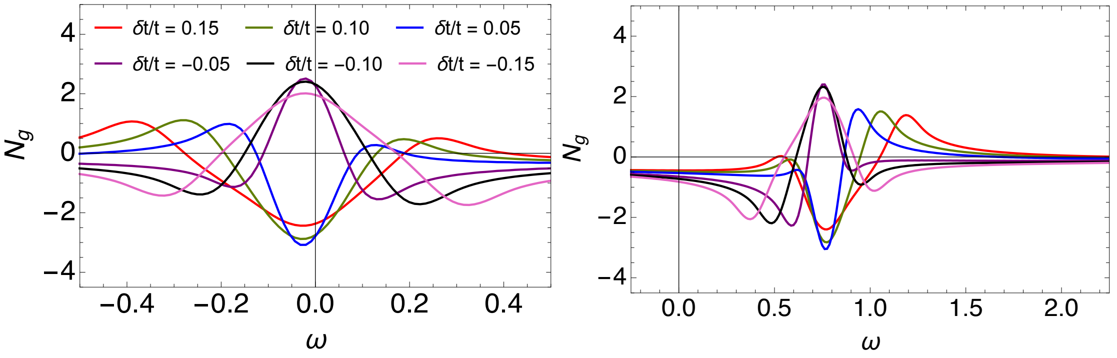

(c) $t'/t = -0.2$ (d) $t'/t = 0.2$

Figure 4.16: The noninteracting LDOS susceptibility N_g from Eq. (4.32) as a function of frequency at optimal filling $n = 0.85$, at room temperature ($T = 297K$), for various t' and $\delta t/t$. The noninteracting system is computed using the bare band-structure. (a) $t'/t = -0.4$, (b) $t'/t = -0.2$, (c) $t'/t = 0.0$, (d) $t'/t = 0.2$. All the figures share a legend.

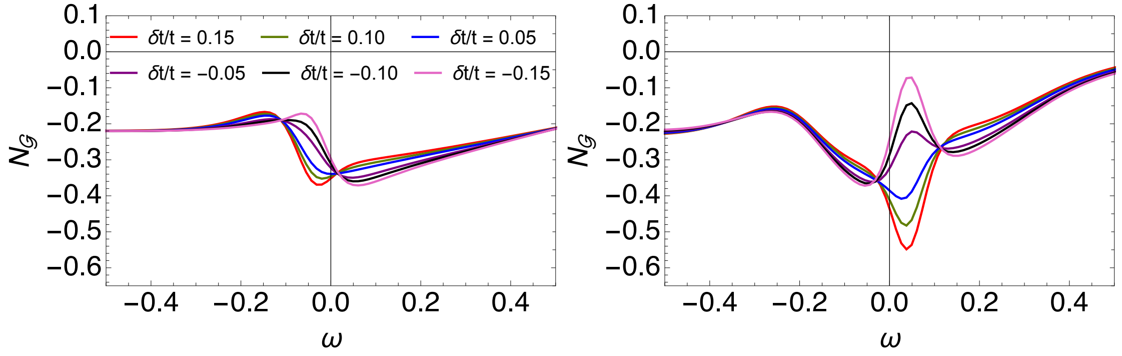

(a) $t'/t = -0.4$

(b) $t'/t = 0.0$

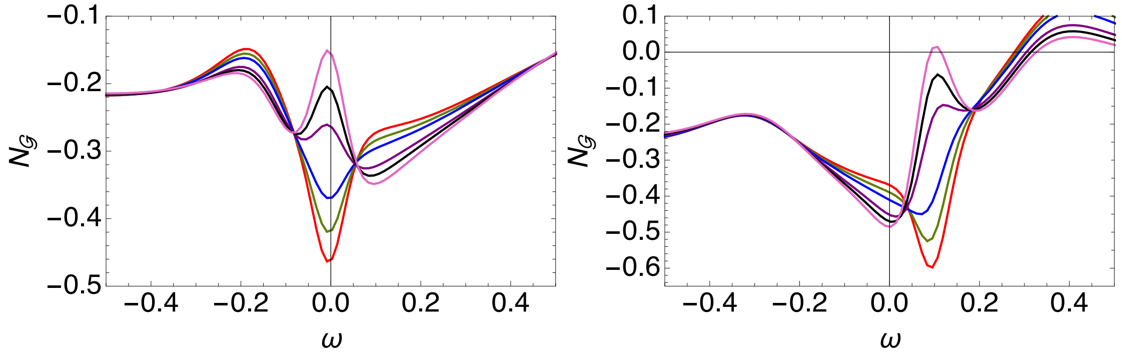

(c) $t'/t = -0.2$

(d) $t'/t = 0.2$

Figure 4.17: The interacting LDOS susceptibility $N_{\mathcal{G}}$ Eq. (4.33) as a function of frequency at optimal filling $n = 0.85$, at room temperature ($T = 297K$), for various t' and $\delta t/t$. The interacting system is computed using the t-t'-J model. (a) $t'/t = -0.4$, (b) $t'/t = -0.2$, (c) $t'/t = 0.0$, (d) $t'/t = 0.2$. All the figures share a legend.

4.3.5 Susceptibility versus strain

Changing up the perspective, we explore the LDOS susceptibility now as a function of strain, at four representative frequencies as seen in Fig. 4.18. We can approximate the variance in the linear response function in Eqs. (4.32) and (4.33)

$$N(T) = c_0(T) + c_1(T)(\delta t/t) + c_2(T)(\delta t/t)^2 + \dots \tag{4.34}$$

where c_0 is the linear term, c_1 is the second order term, and c_2 is the third order term of the response. We see that for the bare LDOS, Fig. 4.18(a), at $\omega = 0.45$ the system is nearly linear with $c_0 \approx -0.5$ and $c_1 \approx 3$. The other presented frequencies appear to be nonlinear with significant second and third order terms. The LDOS susceptibility for the interacting system [panel (b)] appears to be nearly linear everywhere except at the location of the LDOS peak ($\omega = 0$) which has a strong quadratic response, suggesting that at temperatures relevant to experiments nonlinear behavior is only observable at energies near the Fermi surface. Note that the second order scheme used here is good for low energies but somewhat less reliable at high energies, $|\omega| \gtrsim k_B T_{FL}$.

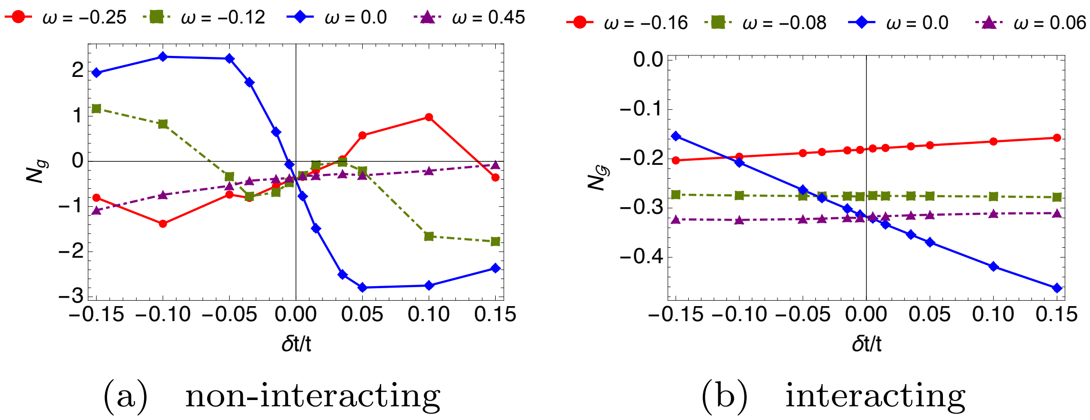

(a) non-interacting (b) interacting

Figure 4.18: The LDOS susceptibility versus strain at optimal filling $n = 0.85$, at room temperature ($T = 298K$), for $t' = -0.2t$, at a few representative frequencies ω in units of t. (a) The noninteracting system (band-structure) in Eq. (4.32). (b) The interacting system (t-t'-J model) in Eq. (4.33).

Chapter 5

Summary and Comments

5.1 Summary

In this work, we have applied the ECFL theory to study the effect of small strain on the resistivity, kinetic energy, LDOS, and their associated susceptibilities in the t-t'-J model Eq. (2.2) with various t' at $n = 0.85$. These results are expected to be relevant to cuprate superconductors, especially single layered materials, where the calculated unstrained resistivities are in good accord with the experimental data [64].

Based on comparisons carried out earlier, the second order scheme of ECFL used here is expected to be reasonable in the density range $0.85 \gtrsim n \gtrsim 0.80$ spanning an experimentally accessible range in cuprates. With improvements in the theoretical scheme, we expect that while resistivities themselves might not change too much, the related susceptibilities [involving division by the small resistivity as in Eq. (2.1)] could be more sensitive.

Our results exhibit in considerable detail the theoretically expected strain dependence of resistivity and LDOS as well as optical weight. The derived susceptibilities depend sensitively on the magnitude and sign of t'. Our results in Figs. 2 and 3 illustrate the quantitative change of the strain dependence due to varying the magnitude and sign of t'. We should stress that the absolute scale of t is important in determining the T dependence. For illustration we have used $t = 0.45$eV in the present paper while the more fine-tuned estimates in Ref. [64] suggest a material dependent and somewhat larger value of t~1eV in most cases.

Our results can be converted to actual strains as in Eq. (4.11), with α in the range $\alpha \in \{2, 5\}$. If data is available one may ideally eliminate α by measuring the strain dependence of the LDOS or the optical conductivity sum rule.

5.2 Comments on experiments

The results found in Fig. 4.2 and Fig. 4.3 yield a magnitude of the nematic susceptibility $\chi_{nem} \sim (1-5)\alpha$ for cuprates. Using the expected range of $\alpha \in \{2, 5\}$, we find χ_{nem}~ 2-25. On the other hand, iron based pnictide superconductors appear to have a considerably larger value for χ_{nem}, e.g., in Fig. 3 of Ref. [17] the range $|\chi_{nem}| \lesssim 650$ is reported, thus an order of magnitude greater than our theoretical estimate for cuprates. While fluctuations may drive the magnitude of nematicity further upwards, especially at some densities and temperatures, it appears that the baseline magnitude of this object is itself much larger than expected in cuprates. For example in the four featureless curves of Fig. 3 of Ref. [17] we see that $|\chi_{nem}|$ ~200.

This magnitude indicates that the downfolding of the many bands of the pnictides to an effective single (or few) band model must yield hopping parameters that are much more sensitive to strain than in cuprates. The different types of quantum overlap of relevant atomic orbitals from those in cuprates are presumably the origin of this difference. We also note that the sharp peaks in $|\chi_{nem}|$ on varying T, as reported in Refs. [17, 18] are missing in our results. Instead we have a monotonic increase of $|\chi_{nem}|$ and related susceptibilities as we cool the system, as seen in Fig. 4.2, Fig. 4.3 and Fig. 4.6. This increase is largely due to the decrease of the (unstrained) resistivity with lowering T in the Fermi liquid regime.

The sign of χ_{nem} presents a more subtle problem. In iron pnictides it is known to be sensitive to effective mass anisotropy. In fact it changes sign with doping in certain hole-doped iron pnictides [12]. Our single band model lacks such an anisotropy and is therefore not appropriate to describe the elastoresistivity of iron pnictide materials.

Recently, we came across the measurement of the elastoresistivity nematic susceptibility in Ref. [41] on the two layer cuprate Bi2212. In this experiment, the magnitude of the nematic susceptibility is found to be in the range $|\chi_{nem}| \in \{2.5, 5\}$. This range is consistent with our theoretical estimate. It is also smaller than the nematic susceptibility in iron pnictides by about two orders of magnitude.

The sign of the nematic susceptibility χ_{nem} [Eq. (2.1)] reported in Ref. [41] implies that the resistivity *increases* in the direction of compression. This result has the opposite sign to our theoretical result as seen in Fig. 4.2 and Fig. 4.3. There we see that the theoretical resistivity *decreases* in the direction of compression, although it does *increase* in the transverse direction. It is possible that the two-layer nature of Bi2212 might be responsible for this opposite sign. Also as noted in Fig. 4.8, the behavior of the nematic susceptibility $\chi_{nem} = \lim_{\epsilon_{xx} \to 0}(\alpha \chi_{xx})$ at sufficiently low T has the potential for a change of sign, depending on how we choose a sufficiently small $|\epsilon_{xx}|$ or $|\delta t/t|$ for the purpose of taking the limit $\lim_{\epsilon_{xx} \to 0}$. On the experimental side, a more detailed T variation and examining the various susceptibilities listed in Fig. 4.8 should yield a more complete picture.

The results found here should also motivate further studies of the strain variation of the three-dimensional electronic bands of cuprates, towards computing strain variation of the resulting two-dimensional bands found from projecting to a t-t'-J model. These would test the simple assumptions made here between strain and hopping parameters of a reduced two-dimensional model as presented in Eqs. (3.19), (3.24), (3.25), and (3.26). It is also possible that under certain situations, the sign of α can even be changed, as a naive interpretation of the experiments of Ref. [41] suggests.

We believe that it is important to study a more extensive set of samples including single layer cuprates at various compositions in the future. It would also be useful to study the variations of resistivity along different axes, parallel *and* transverse to the strain axis and extend the studies to various T's. This type of measurements would enable the construction of the symmetry adapted susceptibilities as in Fig. 4.8, which provide a greater insight into the results. It would also be of considerable interest to measure the variations of the LDOS and optical weight with strain, as emphasized above.

Part III

DIELECTRIC RESPONSE WITH SHORT AND LONG RANGE CORRELATIONS

Chapter 6

Introduction

The role of strong local correlations and their interplay with long ranged Coulomb interactions, is an important problem in condensed matter physics. In the context of the metal insulator (Mott-Hubbard) transition of a Hubbard-Gutzwiller-Kanamori type model of strong correlations with added long ranged Coulomb interactions, early work [60, 13, 82] emphasized that this combination of the two types of interactions, quite generally leads to a metal with poor screening. These works noted that strong local correlations enhance the effective mass of electrons near a Mott transition, with $m^*/m \sim 1/(1-U/U_c)$ at half filling $n=1$, or with $m^*/m \quad \sim \quad \frac{1}{(1-n)}$ with $U \gg t$[7]. and U_c is the putative critical interaction strength discussed in [13]. These result in the enhancement of the density of states $\frac{dN}{d\mu} \propto \frac{m^*}{m}$, which in turn suppresses the screening constant q_s related by the compressibility sum-rule [54] (see Eqs. (10.6)–(10.8) below):

$$q_s^2 = \frac{4\pi q_e^2}{a_0^3 N_s} \frac{dN}{d\mu} \to 0, \tag{6.1}$$

thereby increasing the screening length $\lambda_s = 2\pi/q_s$. More recent theoretical work [8, 15] has focused on the dynamical aspects of screening, within the program of unifying band structure methods with dynamically screened Coulomb interaction and short ranged correlations. The latter are usually treated within the dynamical mean field theory [8, 15].

An immediate motivation for the present work comes from a set of experiments using the recently developed tool of *momentum resolved electron energy loss spectroscopy* (M-EELS) [81, 51, 34]. This technique gives a direct readout of the structure function $S(\vec{q}, \omega)$ or equivalently the dielectric function $\varepsilon(\vec{q}, \omega)$, for a broad range of momentum transfer $\vec{q}$ and energy transfer ω. The initial application of this technique has provided high resolution data on the structure function for the archetypical strongly correlated cuprate superconducting material $Bi_{2.5}Sr_{1.9}CaCu_2O_{8+x}$ $(BSSCO)$, for two samples with $T_c = 91$K and $T_c = 50$K respectively. In the normal state, the data looks very different from what one might expect for a conventional weakly correlated Fermi liquid, e.g., one describable by the random-phase approximation (RPA). Sharp features arising from long lived quasiparticles in that theory are rounded off to broad peaks, and the spectrum has surprisingly long frequency tails. Understanding the data seems to require reducing the quasiparticle domination in charge response functions, as argued in Refs. [79, 80].

In this work we use an extended *extremely correlated Fermi liquid theory* (ECFL) [66], where the long ranged component of the Coulomb interaction is added.

---

[7] We denote by U and t the standard interaction and hopping parameters of the Hubbard model with N_s sites. Here the lattice constant is a_0, and we denote by q_e the electron charge, i.e., $q_e = -|e|$.

We thus calculate the charge dynamics of the t-J-V_C model Eq. (7.1), which is a generalization of the t-J model obtained by adding to it a long-ranged Coulomb interaction V_C. For this model we calculate the $\{\vec{q}, \omega\}$ dependent dielectric function $\varepsilon\{\vec{q}, \omega\}$ and the charge and current susceptibilities.

The ECFL theory was developed to describe the very large U Hubbard model, or equivalently the short ranged t-J interaction [66]. It therefore deals with the propagation and interaction of Gutzwiller projected electrons, obeying non-canonical anticommutators Eq. (7.7), within a tight binding model. The ECFL theory is characterized by a small but non-zero quasiparticle weight $Z \ll 1$ [66], and is therefore suitable for describing the above experiments.

The theory of the interacting 2-d electron system presented here differs significantly from earlier theories designed in the contexts of semiconductor inversion layers, surfaces of metals and more recently for graphene [74, 20, 35, 75]. In the current study, the dominant interaction is the short ranged Coulomb repulsion on the scale of a single atom, i.e., the Gutzwiller-Hubbard correlation. If one starts from weakly-interacting electrons within a perturbative scheme, it is very difficult to build in the strong local correlations, since the perturbation parameter is the largest energy scale! We start instead with non-canonical Gutzwiller projected electrons $\widetilde{C}_{i\sigma}$ Eqs. (7.1) and (7.7), and then introduce long ranged Coulomb interactions, giving the t-J-V_C model.

In this treatment the physics of the Mott-Hubbard insulator at half filling is obtained naturally, in view of the inbuilt Gutzwiller projection. This generalized ECFL calculation provides a microscopic theory of charge fluctuations in a metal, with fragile quasiparticles. We provide results for sum-rules, plasma frequencies and other measurable quantities, as functions of a few model parameters.

6.1 The outline

We define the t-J-V_C model below in Chapter 7, and summarize the method used to calculate the dynamic charge susceptibility. The calculation uses the ECFL theory to calculate the electron Green's function $\mathcal{G}$ to a certain approximation (termed as $\mathcal{O}(\lambda^2)$), which has been described in detail in our recent publications [6, 65]. To make this work self contained, we summarize the scheme and the equations used to compute $\mathcal{G}$ in Appendix A. In Appendix B we recall the derivation of dielectric constant from linear response theory [54] with dynamic structure function $S(\vec{q}, \omega)$.

In Chapter 8 we present the theoretical formulae for derived in Ref. [72], namely, alternate formulas for the dielectric constant analogous to Nozières formula [54] valid for the (continuum) electron gas and analogous formulas the reducible (unscreened) susceptibility $\widetilde{\chi}_{\rho\rho}$ and the connection between reducible susceptibilities and irreducible (screened) susceptibilities, when we are dealing with non-canonical electrons. We also report expressions for the dynamic charge susceptibility in terms of a novel self-energy.

In Chapter 9 the describes the method for interpolating the two alternative express of the dynamic charge susceptibility which worked better in complementary regions of $\{\vec{q}, \omega\}$ space, as discussed in Section 10.4 and in Section 10.10. The frequency sum-rules for the susceptibility play an important role in our theory and are summarized in Appendix C.

In Chapter 10 we present the methodology for the calculation approximate dielectric function and we present some applications of the dielectric constant. In Chapter 11 we discuss the results and present some conclusions.

Chapter 7

The t-J-V_C model

The t-J-V_C Hamiltonian studied here is

$$H = H_{\rm t} + H_{\rm J} + V_C \tag{7.1}$$

$$H_{\rm t} = -\sum_{ij\sigma} t_{ij} \widetilde{C}^{\dagger}_{i\sigma} \widetilde{C}_{j\sigma} - \boldsymbol{\mu} \sum_i n_i \tag{7.2}$$

$$H_{\rm J} = \frac{1}{2} \sum_{ij} J_{ij} \left(\vec{S}_i . \vec{S}_j - \frac{n_i n_j}{4} \right) \tag{7.3}$$

$$V_C = \frac{1}{2} \sum_{i \neq j} V_{ij} n_i n_j, \quad V_{ij} = \frac{1}{\varepsilon_\infty} \frac{q_e^2}{|\vec{r}_i - \vec{r}_j|} \tag{7.4}$$

with the electronic charge $q_e = -|e|$, the density operator $n_i = \sum_\sigma \widetilde{C}^{\dagger}_{i\sigma} \widetilde{C}_{i\sigma}$, and spin density operator $S_i^\alpha = \frac{1}{2} \sum_{\sigma\sigma'} \widetilde{C}^{\dagger}_{i\sigma} \tau^\alpha_{\sigma\sigma'} \widetilde{C}_{i\sigma'}$, τ^α is a Pauli matrix, and the Coulomb potential is denoted by V_{ij}. The hopping parameters $-t_{ij} = \frac{1}{N_s} \sum_{ij} e^{i\vec{k}(\vec{r}_i - \vec{r}_j)} \varepsilon_k$ are Fourier components of the band energy ε_k, N_s is the number of sites in the crystal. We will study both 3 and 2 dimensional (layered) strongly correlated electron systems, where the Fourier components of V is given in 3-d, assuming a simple cubic cell of side

a_0 by

$$V(\vec{q}) = \frac{1}{N_s a_0^3 \varepsilon_\infty} \frac{4\pi q_e^2}{|\vec{q}|^2} \text{ (3-d)}, \tag{7.5}$$

and in 2-d by

$$V(\vec{q}) = \frac{1}{N_s a_0^2 \varepsilon_\infty} \frac{2\pi q_e^2}{|\vec{q}|} \text{ (2-d)}. \tag{7.6}$$

To simplify the notation we will set $\hbar = 1$ and the lattice constant $a_0 = 1$ in most part below. Here ε_∞ is the static dielectric constant due to screening by mobile charges other than the ones described by H_t, if any are present. Here the correlated Fermi destruction operator $\widetilde{C}_i$ is found from the plain (i.e., canonical or unprojected) operators c_i, by sandwiching it between two Gutzwiller projection operators $\widetilde{C}_{i\sigma} = P_G C_{i\sigma} P_G$. Let us note that these Fermions satisfy a non-canonical set of anticommutation relations

$$\{\widetilde{C}_{i\sigma_i}, \widetilde{C}^\dagger_{j\sigma_j}\} = \delta_{ij}\left(\delta_{\sigma_i\sigma_j} - \sigma_i\sigma_j \widetilde{C}^\dagger_{i\bar{\sigma}_i}\widetilde{C}_{i\bar{\sigma}_j}\right), \text{and } \{\widetilde{C}_{i\sigma_i}, \widetilde{C}_{j\sigma_j}\} = 0. \tag{7.7}$$

The physical meaning of this sandwiching process is that the Fermi operators act within the subspace where projector P_G enforces single occupancy at each site. This model generalizes the well studied t-J model by adding the long ranged Coulomb interaction term, and we will study the effect of the added term in determining the fluctuations of the charge density, the dielectric function and related structure function. We initially keep the dimensionality of the electronic system general so that the results apply to 3-dimensions, and later consider the case of 2-dimensional stacking of the electronic system.

The t-J-V_C model used here neglects multi-band effects and focusses on the extremely correlated single band containing the Fermi surface. It throws out inter-band transition matrix elements of the Coulomb interaction and only retains intraband terms. A rough account of the other bands is taken, by rescaling the Coulomb interaction by an infinite frequency dielectric constant ε_∞ as in Eq. (7.4). This rescaling represents the cumulative effect of the "fast" (i.e. high energy) electrons on the "slow" (low energy) correlated electrons described by our model. This type of reasoning suggests that as long as the excitation energies do not exceed the inter-band energies, the single band model employed here should be quite reliable.

In applying the results of these calculations to real systems, it must be kept in mind that the t-J-V_C model is only a 'low energy' abstraction of the narrow band containing the Fermi energy, which is further embedded in a continuum of bands extending to very high energies. Thus, in an experimental situation, curtailing the frequency integration in Eq. (C.4) up to a cutoff frequency $\Omega \sim 1, 2$ eV is expected to capture the 'low energy' model, with strong correlations built into the results. On the other hand by extending the integral to higher energies, one gets rid of the correlations and the results should reveal the bare electron scales.

Chapter 8

Theoretical Background

In this chapter we present a brief summary of the essentials formulas that characterize the dielectric response function for systems with extreme short-range and strong long-range correlations. Also, we note that detailed derivations of each formula presented here can be found in Ref. [72].

8.1 The Twin Dielectric Functions $\varepsilon(\vec{q}, \omega)$

We present the two reducible susceptibilities $\chi_{\rho\rho}$ and χ_{WW} for interacting electrons on a lattice where the subscript ρ represents the charge density and W is the divergence of charge current density $W = \nabla \cdot J$ on the lattice. We note that the charge density correlation function is defined as

$$\chi_{\rho\rho}(\vec{q}, \tau) = \langle T_\tau \rho_{\vec{q}}(\tau), \rho_{-\vec{q}}(0) \rangle \tag{8.1}$$

and by analogy we can define similar expression for $\chi_{\rho W}$, $\chi_{W\rho}$, and χ_{WW}. Fourier transforming of the time-domain of Eq. (8.1) and analytically continuing the resultant, $i\Omega_n \to \omega + i\eta$, we find $\chi_{\rho\rho}(\vec{q},\omega)$. The relationship between the reducible susceptibility $\chi_{\rho\rho}$ and the dielectric function $\varepsilon(\vec{q},\omega)$ is

$$\frac{1}{\varepsilon(\vec{q},\omega)} - 1 = \frac{V(\vec{q})}{q_e^2}\chi_{\rho\rho}(\vec{q},\omega)\ . \tag{8.2}$$

This relation is readily found [54] from linear response theory. As a consequence of charge dynamics on a lattice and charge conservation these two susceptibilities have the following relationship:

$$\chi_{\rho\rho}(\vec{q},\omega) = \frac{1}{\omega^2}\Big(\chi_{WW}(\vec{q},\omega) - N_s\kappa(\vec{q})\Big)\ . \tag{8.3}$$

where taking $\vec{q}$ to be along the x-axis we find

$$\kappa(\vec{q}) = \frac{2q_e^2}{N_s}\sum_{k\sigma}\left(\varepsilon_{\vec{k}+\vec{q}} - \varepsilon_{\vec{k}}\right)\langle \widetilde{C}^{\dagger}_{\vec{k}\sigma}\widetilde{C}_{\vec{k}\sigma}\rangle\ . \tag{8.4}$$

For general non-parabolic bands

$$\lim_{q\to 0}\kappa(\vec{q}) = |\vec{q}|^2\mathcal{T} \tag{8.5}$$

where the variable $\mathcal{T}$ (equal to the stress tensor per site $\frac{1}{N_s}\langle\tau^{xx}\rangle$ in [70]), is given by

$$\mathcal{T} = \frac{q_e^2}{N_s}\sum_{k\sigma}\left(\frac{d^2\varepsilon_{\vec{k}}}{dk_x^2}\right)\langle \widetilde{C}^{\dagger}_{\vec{k}\sigma}\widetilde{C}_{\vec{k}\sigma}\rangle\ . \tag{8.6}$$

The unscreened current-current susceptibility χ_{JJ} can be expressed in same fashion as Eq. (8.1) and we can relate this to χ_{WW} for small $\vec{q}$:

$$\text{For }\ |\vec{q}|a_0 \ll 1,\ \ \chi_{JJ}(\vec{q},\omega) = \frac{1}{|\vec{q}|^2}\chi_{WW}(\vec{q},\omega)\ . \tag{8.7}$$

Using Eq. (8.3) we find an second formula for $\varepsilon(\vec{q},\omega)$, an alternative to Eq. (8.2),

$$\frac{1}{\varepsilon(\vec{q},\omega)} - 1 = \frac{V(\vec{q})}{q_e^2}\Big(\chi_{WW}(\vec{q},\omega) - N_s\kappa(\vec{q})\Big)\ . \tag{8.8}$$

Next the connection between the reducible $\chi_{\mu\nu}$ and irreducible $\widetilde{\chi}_{\mu\nu}$ susceptibilities can be written compactly as

$$\chi_{\mu\nu}(q) = \widetilde{\chi}_{\mu\nu}(q) - \frac{1}{q_e^2}V(\vec{q})\widetilde{\chi}_{\mu\rho}(q)\chi_{\rho\nu}(q) \tag{8.9}$$

where the pair of subscripts $\{\rho, W\}$ are denoted by greek symbols μ or ν and $q \equiv \{\vec{q},\omega\}$. Solving for the $\chi_{\rho\rho}$ case, we find

$$\chi_{\rho\rho}(q) = \frac{\widetilde{\chi}_{\rho\rho}(q)}{1 + \frac{1}{q_e^2}V(\vec{q})\widetilde{\chi}_{\rho\rho}(\vec{q},\omega)}\ . \tag{8.10}$$

It can be shown using Eq. (8.9) that an alternative form for the irreducible susceptibility

$$\widetilde{\chi}_{\rho\rho}(\vec{q},\omega)\ =\ \frac{1}{\omega^2}\Big(\widetilde{\chi}_{WW}(\vec{q},\omega) - N_s\kappa(\vec{q})\Big) \tag{8.11}$$

has the exact same form as Eq. (8.11). Since $\widetilde{\chi}_{\rho\rho}$ must be finite in the static limit for any generic $\vec{q}$, it follows that the terms in the brackets must cancel, i.e.,

$$N_s\kappa(\vec{q}) = \widetilde{\chi}_{WW}(\vec{q},0)\ , \tag{8.12}$$

and we can write Eq. (8.11) alternatively as

$$\widetilde{\chi}_{\rho\rho}(\vec{q},\omega) = \frac{N_s\kappa(\vec{q})}{\omega^2}\Big(\widetilde{\chi}_{WW}(\vec{q},\omega)/\widetilde{\chi}_{WW}(\vec{q},0) - 1\Big)\ . \tag{8.13}$$

Using Eqs. (8.2), (8.10) and (8.11), we can express the twin formulas for dielectric function in terms of irreducible susceptibilities as

$$\varepsilon(q) \equiv \varepsilon(\vec{q},\omega) = 1 + \frac{1}{q_e^2}V(\vec{q})\widetilde{\chi}_{\rho\rho}(\vec{q},\omega)\ , \tag{8.14}$$

$$\varepsilon(q) \equiv \varepsilon(\vec{q},\omega) = 1 + \frac{1}{q_e^2\omega^2}V(\vec{q})\Big(\widetilde{\chi}_{WW}(\vec{q},\omega) - N_s\kappa(\vec{q})\Big)\ . \tag{8.15}$$

The representation in Eq. (8.14) satisfies the exactly know behavior in low-frequency, long-wavelength limits Eq. (10.4), and the representation in Eq. (8.15) satisfies known high frequency behavior Eq. (C.8).

Based on the formula derivation [72] of Eqs. (8.14) and (8.15) if these two expressions are evaluated exactly, they must coincide. However not all classes of approximation for these expressions are guaranteed to retain their equivalence, but some do agree. For instance, the standard random phase approximation (RPA) uses non-interacting Green's function and the bare vertex and the numerics agree for all $\omega \gtrsim t$. The two susceptibilities are found from the bubble diagram [54]

$$\begin{aligned}
\widetilde{\chi}^{(0)}_{\rho\rho}(\vec{q}, i\Omega_v) &= -q_e^2 \sum_{k\sigma} G_0(k)G_0(k+q) = \sum_{\vec{k}} \frac{f_{\vec{k}} - f_{\vec{k}+\vec{q}}}{\varepsilon_{\vec{k}+\vec{q}} - \varepsilon_{\vec{k}} - i\Omega_v} \ , && (8.16)\\
\widetilde{\chi}^{(0)}_{WW}(\vec{q}, i\Omega_v) &= -q_e^2 \sum_{k\sigma} G_0(k)G_0(k+q) \left(\varepsilon_{\vec{k}} - \varepsilon_{\vec{k}+\vec{q}}\right)^2 \ , && (8.17)\\
&= 2q_e^2 \sum_{\vec{k}} \frac{f_{\vec{k}} - f_{\vec{k}+\vec{q}}}{\varepsilon_{\vec{k}+\vec{q}} - \varepsilon_{\vec{k}} - i\Omega_v} \left(\varepsilon_{\vec{k}} - \varepsilon_{\vec{k}+\vec{q}}\right)^2 \ . && (8.18)
\end{aligned}$$

8.2 Approximating the charge susceptibility using a novel self energy

In order to combine Nozières twin formulas into a single equation that captures the physics for all $\{\vec{q}, \omega\}$, we use a novel representation of the susceptibility using a suitable generalize self-energies as discussed in [68, 52, 23]. The irreducible susceptibility written in terms of a novel self-energy Ψ is

$$\frac{1}{q_e^2 N_s}\widetilde{\chi}_{\rho\rho}(\vec{q},\omega) = \left(\frac{q_e^2 N_s}{\widetilde{\chi}_{\rho\rho}(\vec{q},0)} - \frac{\omega^2}{\widetilde{\omega}^{(1)}(\vec{q})} - \Psi(\vec{q},\omega)\right)^{-1} \tag{8.19}$$

where $\widetilde{\omega}^{(1)}(\vec{q})$ is the first moment of the high frequency expansion discussed in Appendix C.2. The complex susceptibility Eq. (8.19), separating $\Psi = \Psi' + i\Psi''$, can be written in an alternative form as

$$\frac{1}{q_e^2 N_s}\widetilde{\chi}_{\rho\rho}(\vec{q},\omega) = \left(\frac{1}{\widetilde{\omega}^{(1)}(\vec{q})}\{\Omega^2(\vec{q},\omega) - \omega^2\} - i\Psi''(\vec{q},\omega)\right)^{-1}, \tag{8.20}$$

where the characteristic energy scale $\Omega(\vec{q},\omega)$ is given by

$$\Omega^2(\vec{q},\omega) \;=\; \widetilde{\omega}^{(1)}\left(\frac{d\mu}{dn}\gamma(\vec{q}) - \Psi'(\vec{q},\omega)\right), \tag{8.21}$$

$$\gamma(\vec{q}) = \frac{\widetilde{\chi}_{\rho\rho}(0,0)}{\widetilde{\chi}_{\rho\rho}(\vec{q},0)}, \quad \gamma(0) = 1 \tag{8.22}$$

This equation makes use of the exact result in Eq. (10.4) to express the static limit of the susceptibility in terms of the thermodynamics variable $\frac{d\mu}{dn}$. Note that the peaks of $\widetilde{\chi}_{\rho\rho}$ are located at $\omega^2 = \Omega^2(\vec{q},\omega)$. As $q \to 0$ the peaks approach zero energy so the approximate energy scale of the peaks Ω_p is given by

$$\Omega_p(\vec{q}) = \Omega(\vec{q},0) = \sqrt{\widetilde{\omega}^{(1)}(\vec{q})\frac{d\mu}{dn}\gamma(\vec{q})}\,. \tag{8.23}$$

We also note that the width of the peak

$$\Gamma_p(\vec{q}) = \sqrt{\widetilde{\omega}^{(1)}\Psi''(\vec{q},\Omega_p(\vec{q}))}\,. \tag{8.24}$$

Chapter 9

Calculating the approximate dielectric constant

The main problem of interest in this work is the t-J-V_C model. Here the short ranged Coulomb interactions lead to a Mott-Hubbard type insulating state at half filling, and doping such a state with holes leads to a metallic state of a very unusual — endowed with a small quasiparticle weight. Adding long ranged Coulomb interactions to this state poses a considerable difficulty. While we are able to obtain a fairly sophisticated single electron Green's function $\mathcal{G}$ from the ECFL theory [66], the two particle response functions are currently unreliable. This is a difficult task even for the simpler case of canonical electrons and has led to a variety of beyond-RPA type approximations [33].

For Gutzwiller projected electrons, it is indeed a formidable task. In this situation, the availability of the two alternate formulas Eqs. (8.14) and (8.15) is very helpful. We can compute the susceptibilities $\widetilde{\chi}_{\rho\rho}(\vec{q},\omega)$ and $\widetilde{\chi}_{WW}(\vec{q},\omega)$ at all $\{\vec{q},\omega\}$, using only the above $\mathcal{G}$ within a bubble scheme $\mathcal{G}\mathcal{G}$ as described below in Eqs. (9.1) and (9.2). Being approximate, these two estimates differ in general, but provide complementary perspective on the dielectric response at various $\vec{q}, \omega$. This provides us with the possibility of combining the two formulas, to obtain an approximate answer whose broad characteristics are known beforehand.

9.1 Calculation of the irreducible susceptibilities $\widetilde{\chi}_{\rho\rho}(\vec{q}, \omega)$ and $\widetilde{\chi}_{WW}(\vec{q}, \omega)$

It is very convenient to calculate the susceptibility starting from formulas Eq. (8.19). The input variables in Eqs. (8.19) and (8.20) are found from the ECFL theory, using suitable approximations described next. We make extensive use of the *bubble approximation*, where for $\widetilde{\chi}_{\rho\rho}$ we find an approximate expression from this bubble approximation

$$\widetilde{\chi}^{\mathrm{Bub}}_{\rho\rho}(\vec{q}, \omega) = -q_e^2 \sum_{k\sigma} \mathcal{G}(k)\mathcal{G}(k+q), \tag{9.1}$$

and evaluating $\widetilde{\chi}_{WW}$ within the bubble approximation

$$\widetilde{\chi}^{\mathrm{Bub}}_{WW}(\vec{q}, \omega) = -q_e^2 \sum_{k\sigma} \mathcal{G}(k)\mathcal{G}(k+q)(\varepsilon_k - \varepsilon_{k+q})^2. \tag{9.2}$$

Using the spectral representation Eq. (A.13) for $\mathcal{G}$ the latter reduces to

$$\widetilde{\chi}^{\mathrm{Bub}}_{WW}(\vec{q},\omega) = 2q_e^2 \sum_k (\varepsilon_k - \varepsilon_{k+q})^2 \\ \times \int_{\nu_1\nu_2} \frac{f(\nu_1) - f(\nu_2)}{\nu_2 - \nu_1 - \omega - i0^+} A(k,\nu_1)A(k+q,\nu_2), \tag{9.3}$$

where $\int_\nu = \int_{-\infty}^{\infty} d\nu$. The density response $\widetilde{\chi}^{\mathrm{Bub}}_{\rho\rho}(\vec{q},\omega)$ is found by dropping the factor $(\varepsilon_k - \varepsilon_{k+q})^2$ in this formula. The spectral functions in our model (see Fig. 10.1) consist of a quasiparticle part with a much-reduced weight $Z \ll 1$, and an extended background part. The indicated integrations can be performed numerically.

9.2 Approximating the irreducible susceptibility $\widetilde{\chi}_{\rho\rho}(\vec{q},\omega)$

Our two starting points are susceptibilities found from these bubble estimates and Eq. (8.13)

$$\widetilde{\chi}_A(\vec{q},\omega) = \widetilde{\chi}^{\mathrm{Bub}}_{\rho\rho}(\vec{q},\omega) \tag{9.4}$$

$$\widetilde{\chi}_B(\vec{q},\omega) = \frac{N_s\kappa(\vec{q})}{\omega^2}\left(\widetilde{\chi}^{\mathrm{Bub}}_{WW}(\vec{q},\omega)/\widetilde{\chi}^{\mathrm{Bub}}_{WW}(\vec{q},0) - 1\right). \tag{9.5}$$

For $\widetilde{\chi}_B$ we verify that $\widetilde{\chi}^{\mathrm{Bub}}_{WW}(\vec{q},0)$ agrees closely with $N_s\kappa(\vec{q})$, calculated independently using a single Green's function $\mathcal{G}$ from Eq. (8.4), at all $\vec{q}$ (see Fig. 10.6). The estimate $\widetilde{\chi}_A$ provides a reasonable estimate in the static limit for the susceptibility. The magnitude of the compressibility, found by taking the $\vec{q} \to 0$ limit, is much smaller than the band value, as seen in Fig. 10.4. It is comparable for most densities to that found from thermodynamical evaluation of $\frac{dn}{d\mu}$ (see Fig. 10.4). At finite $\vec{q}$ its shape resembles that of the band susceptibility (see Fig. 10.5). The imaginary part of $\widetilde{\chi}_A$ shows a quasiparticle contribution of the type $\chi'' \propto \frac{\pi\omega}{|\vec{q}|v_F}$ for very small $\omega < |\vec{q}|v_F Z$. For larger ω, it has a broad contribution from the background spectral functions, but does not give the first moment of frequency, and is therefore not satisfactory.

The estimate $\widetilde{\chi}_B$ is expected to be satisfactory at finite (high) frequencies since it is constructed to satisfy the first moment of frequency in the high ω limit. However, at at low ω it is does not capture the quasiparticle contribution discussed above. Further the static limit — found from the $\mathcal{O}(\omega^2)$ limiting behavior of $\widetilde{\chi}^{\text{Bub}}_{WW}(\vec{q},\omega)$ — does not display the behavior expected for an incompressible system discussed above. Thus, the two estimates are successful in almost non-overlapping regimes of frequency.

Before proceeding we note that the two expressions Eqs. (9.4) and (9.5) lead to two different self-energies

$$\Psi_A(\vec{q},\omega) + \frac{\omega^2}{\widetilde{\omega}^{(1)}_A(\vec{q})} = \frac{N_s q_e^2}{\widetilde{\chi}_A(\vec{q},0)} - \frac{N_s q_e^2}{\widetilde{\chi}_A(\vec{q},\omega)} \tag{9.6}$$

$$\Psi_B(\vec{q},\omega) + \frac{\omega^2}{\widetilde{\omega}^{(1)}_B(\vec{q})} = \frac{N_s q_e^2}{\widetilde{\chi}_B(\vec{q},0)} - \frac{N_s q_e^2}{\widetilde{\chi}_B(\vec{q},\omega)}. \tag{9.7}$$

The first frequency moment $\widetilde{\omega}^{(1)}_B(\vec{q})$ in the second equation Eq. (9.7) is in fact exact, i.e. $\widetilde{\omega}^{(1)}_B(\vec{q}) = \widetilde{\omega}^{(1)}(\vec{q})$, as explained above. The corresponding frequency $\widetilde{\omega}^{(1)}_A(\vec{q})$ is not correct, and we show that it is possible to avoid using it altogether.

Consider the approximate susceptibility $\widetilde{\chi}^{(I)}$ combining the two susceptibilities

$\widetilde{\chi}_A, \widetilde{\chi}_B$ as

$$\widetilde{\chi}^{(I)}(\vec{q},\omega) = \left\{ \frac{1}{\widetilde{\chi}_A(\vec{q},0)} - \frac{1}{\widetilde{\chi}_B(\vec{q},0)} + \frac{1}{\widetilde{\chi}_B(\vec{q},\omega)} \right\}^{-1} \tag{9.8}$$

$$= N_s q_e^2 \left\{ \frac{N_s q_e^2}{\widetilde{\chi}_A(\vec{q},0)} - \frac{\omega^2}{\widetilde{\omega}^{(1)}(\vec{q})} - \Psi_B(\vec{q},\omega) \right\}^{-1}. \tag{9.9}$$

It is readily seen from the arguments given above, to give the correct plasma frequency as well as the correct static limit, while respecting the strong local correlations. It therefore serves as a reasonable approximation over the entire frequency domain.

A feature that is missing from $\widetilde{\chi}^{(I)}$ in Eq. (9.9), is the quasi-particle contribution. This was present in Eq. (9.4), but was left out in Eq. (9.9) since we threw out all the frequency dependence of $\widetilde{\chi}_A$. We can incorporate this contribution, again approximately, by making a correction to Ψ_B taken from Ψ_A. Inspection shows that for small $\vec{q}, \omega$ the quasiparticle feature in $\widetilde{\chi}_A$ arises from a contribution $\operatorname{Im}\Psi_A \propto \frac{\omega}{|\vec{q}|v_f}$. It is analogous to the familiar correction that arises in the Lindhard function from quasiparticles [54, 1, 24]. This quasiparticle contribution leads to $|\operatorname{Im}\Psi_A(\vec{q},\omega)| > |\operatorname{Im}\Psi_B(\vec{q},\omega)|$ for small enough ω at a fixed $\vec{q}$, while for larger $|\omega|$ we find $|\operatorname{Im}\Psi_B(\vec{q},\omega)| \gg |\operatorname{Im}\Psi_B(\vec{q},\omega)|$. To further refine the approximation, we keep this observation in mind and add the incremental $\delta\Psi_{QP}(\vec{q},\omega)$ containing the quasiparticle damping to Ψ_B,

$$\widetilde{\chi}^{(II)}(\vec{q},\omega) = N_s q_e^2 \left\{ \frac{N_s q_e^2}{\widetilde{\chi}_A(\vec{q},0)} - \frac{\omega^2}{\widetilde{\omega}^{(1)}(\vec{q})} - \Psi_B(\vec{q},\omega) - \delta\Psi_{QP}(\vec{q},\omega) \right\}^{-1}. \tag{9.10}$$

Since $\operatorname{Im}\delta\Psi_{QP}$ should add the damping due to quasiparticles, with $\omega > 0$ we choose

$$\operatorname{Im}\delta\Psi_{QP}(\vec{q},\omega) = \operatorname{Max}\{\operatorname{Im}\Psi_A(\vec{q},\omega), \operatorname{Im}\Psi_B(\vec{q},\omega)\} - \operatorname{Im}\Psi_B(\vec{q},\omega), \tag{9.11}$$

It is easily seen that $\mathrm{Im}\,\delta\Psi_{QP}(\vec{q},\omega)$ vanishes outside the region $|\mathrm{Im}\,\Psi_A(\vec{q},\omega)| > |\mathrm{Im}\,\Psi_B(\vec{q},\omega)|$. For $\omega < 0$ a similar argument can be used keeping in mind the odd-ness of $\mathrm{Im}\,\Psi's$ in ω, we use Min instead of Max in Eq. (9.11). The real part of $\delta\Psi_{QP}$ can be calculated using the Kramers-Kronig relation, i.e., by taking the real part Ψ in Eq. (8.19)

$$\mathrm{Re}\delta\Psi_{QP}(\vec{q},\omega) = -\mathcal{P}\frac{1}{\pi}\int_{-\infty}^{\infty} d\nu\,\frac{\mathrm{Im}\,\delta\Psi_{QP}(\vec{q},\nu)}{\omega-\nu} - \frac{1}{\pi}\int_{-\infty}^{\infty} d\nu\,\frac{\mathrm{Im}\,\delta\Psi_{QP}(\vec{q},\nu)}{\nu}, \tag{9.12}$$

whereby we guarantee that $\delta\Psi_{QP}(\vec{q},0) = 0$.

On further separating the complex self-energies, these two approximate susceptibilities Eqs. (9.9) and (9.10) lead to expressions analogous to Eq. (8.20), with the same static susceptibility Eq. (8.22) but slightly different characteristic frequencies Ω in Eq. (8.21).

With these approximations $\widetilde{\chi}^{(I)}(\vec{q},\omega), \widetilde{\chi}^{(II)}(\vec{q},\omega)$, the 2-d dielectric function can be written in the form

$$\begin{aligned}\varepsilon^{(I,II)}(\vec{q},\omega) &= 1 + \frac{2\pi q_e^2}{|\vec{q}|a_0^2 N_s q_e^2 \varepsilon_\infty}\widetilde{\chi}^{(I,II)}(\vec{q},\omega)\\ &= 1 + \frac{g_c}{|\vec{q}|a_0}\left(\frac{t}{q_e^2 N_s}\widetilde{\chi}^{(I,II)}(\vec{q},\omega)\right),\end{aligned} \tag{9.13}$$

where the dimensionless Coulomb constant is defined by

$$g_c = \frac{2\pi q_e^2}{\varepsilon_\infty\, a_0 t}. \tag{9.14}$$

With the 2-d lattice constant $a_0 = 3.81\mathring{A}$, $t = 0.45eV$ and $\varepsilon_\infty = 1.76$, we get $g_c \sim 30.0$. Since these basic parameters can vary somewhat, we present results for $g_c = 10, 50, 100$ in the following.

Chapter 10

Calculations and results

We calculate the Green's functions using the set of formulas summarized in Appendix A Eqs. (A.5)–(A.12), employing the set of band and model parameters

$$t = 0.45eV,\ t' = -0.2t,\ J = 0.17t, . \tag{10.1}$$

The system sizes used in most of the presented calculations are

$$N_\omega = 2^{14},\ L_x \times L_y = 64 \times 64 \text{ (correlated model)}$$

where N_ω is the number of ω points in the frequency grid and L_x, L_y are the dimensions of the 2-d lattice. For Fig. 10.18, Fig. 10.20, as well as the reference uncorrelated model we use bigger spatial grids $L_x \times L_y = 128 \times 128$. We present results at a few representative temperatures, and focus on two densities $n = 0.80$ and $n = 0.85$. These correspond to the overdoped regime and optimally doped cases. As mentioned above, the resistivity tensor, the optical conductivity and spectral functions have been recently published by us in [6, 65], at these and more enlarged set of parameters. Here we concentrate our attention on the density response function $\widetilde{\chi}^{(I)}(\vec{q},\omega)$ and $\widetilde{\chi}^{(II)}(\vec{q},\omega)$ defined in Eqs. (9.4) and (9.5) and the corresponding dielectric functions Eq. (9.13). We also focus on the corresponding current response functions $\widetilde{\chi}_{JJ}(\vec{q},\omega)$ defined in Eq. (10.19), and the optical conductivity i.e., the $\vec{q} \to 0$ limit of Eq. (10.21). These variables are relevant for understanding the experiments in [81, 51, 34].

10.1 Spectrum $A(\vec{k},\omega)$

We now present the results from this formalism. We begin with the electronic spectral function $A(\vec{k},\omega)$ obtained by solving for the ECFL Green's function in Fig. 10.1. The figure is at the density $n = 0.85$ and at two temperatures $T = 99$K and $T = 297$K. The quasiparticle weight is seen to be very small $Z = 0.06, 0.09$ for $T = 99$K and $T = 297$K respectively. The area sum-rule for the lower Hubbard band spectral function reads as: $\int d\omega A(\vec{k},\omega) = 1 - \frac{n}{2}$, it is satisfied by depleting the quasiparticle peak, and smearing it over a wide background. This redistribution of weight accounts for the broad and featureless background seen in the spectral functions, it is a reflection of the strong local correlations.

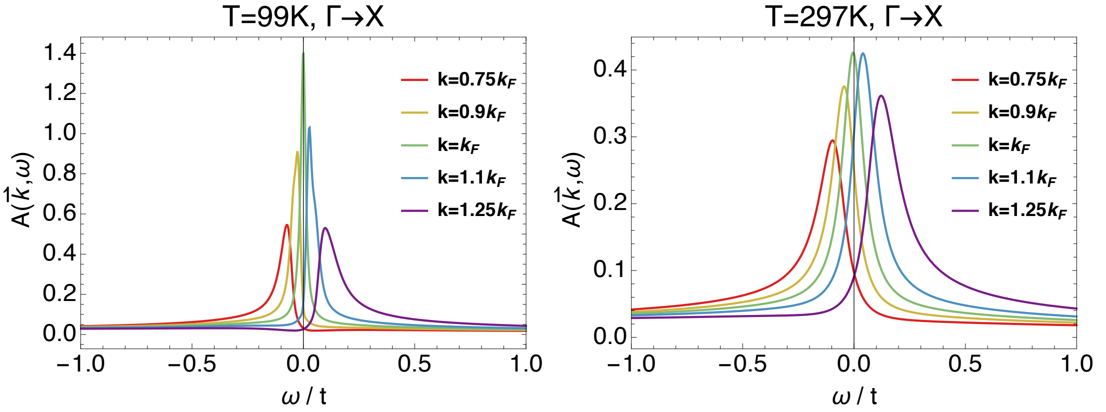

(a) (b)

Figure 10.1: The (single) electronic spectral functions for the ECFL Green's function at two temperatures: (a) $T = 99$K and (b) $T = 297$K. The Fermi wavevector is $k_F a_0 = 1.36$, and the quasiparticle weight is $Z = 0.0612, 0.0860$ for $T = 99$K and $T = 297$K respectively. The thermal sensitivity of the spectral width is a characteristic of the ECFL theory, where the effective Fermi temperature is much suppressed from the band value. The reduced quasiparticle weight is also noted in Fig. 10.2, leading to a very small jump.

10.2 Momentum Distribution $(n_k) m_k$

In Fig. 10.2 we display the momentum distribution function m_k, i.e., $\langle \widetilde{C}^\dagger_{k\uparrow} \widetilde{C}_{k\uparrow} \rangle$ for correlated electrons, and the analogous band value n_k for uncorrelated electrons at two densities $n = 0.85$ and $n = 0.80$. In the limit of $T \to 0$ this curve develops a jump in the distribution at k_F of magnitude Z, following the theorem of Migdal. A sharp reduction of the quasiparticle weight Z, noted in Fig. 10.1, is also evident from the flattening of the correlated distribution m_k.

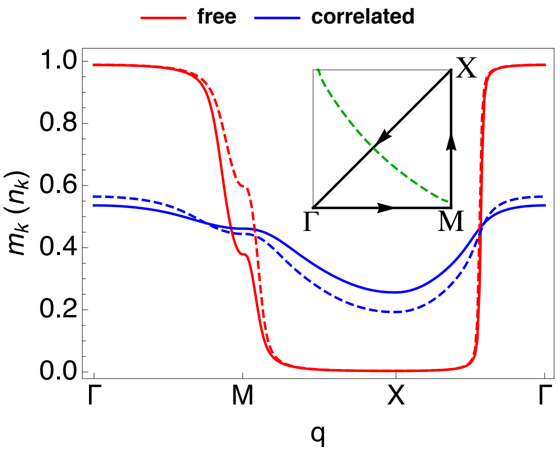

(a)

Figure 10.2: The momentum distribution function m_k for correlated electrons defined as $m_k = \langle \widetilde{C}^\dagger_{k\uparrow}\widetilde{C}_{k\uparrow}\rangle$ in blue, and the analogous function n_k for uncorrelated electrons ($n_k = \langle c^\dagger_{k\uparrow}c_{k\uparrow}\rangle$) in red, plotted over the Brillouin zone. The solid lines are at $n = 0.85$, and the dashed lines are at $n = 0.80$. Here we used $t = 0.45, t' = -0.2, J = 0.17$ in units of eV, and $T = 297$K. and the system size used in the computation is given in Eq. (10.2). The wavevector q traverses the octant of the Brillouin Zone, with corners $\Gamma = (0,0)$, M=$(\pi,0)$, and $X = (\pi,\pi)$ and the green dashed line traces the Fermi surface. A sharp reduction of the quasiparticle weight Z is evident from the flattening of the correlated distribution m_k in this figure.

10.3 Quasiparticle Weight Z

In this section we compute the quasiparticle weight (see Fig. 10.3) for electron with Hubbard-Gutzwiller-Kanamori type short-range correlations. The formula for the quasiparticle weight is defined as

$$Z_k^{-1} = 1 - \left.\frac{\partial \Sigma'}{\partial \omega}\right|_{\omega=\epsilon^*_k} \tag{10.2}$$

where $\epsilon^*_k = \epsilon_k + \Sigma'(\vec{k},\omega)$ is the renormalized energy (marked by the electron spectrum peaks in Fig. 10.1) and Σ' is the real part of the Dyson Self-Energy:

$$\Sigma(\vec{k},\omega) = \omega - \epsilon_k + \mu - \frac{1}{G(\vec{k},\omega)}\ . \tag{10.3}$$

In the neighborhood the Fermi surface, where Im Σ is small and $Z \ll 1$, we have well defined fragile quasiparticles in broad background continuum in this model. Far outside the neighborhood of the Fermi surface, $\epsilon_k^* \sim 0$ and $|\vec{k}_F - \vec{k}| < \frac{\varepsilon_F}{\hbar v_F}$, the quasiparticle concept loses its meaning, i.e., the distinction between the coherent quasiparticle and incoherent background continuum becomes blurred.

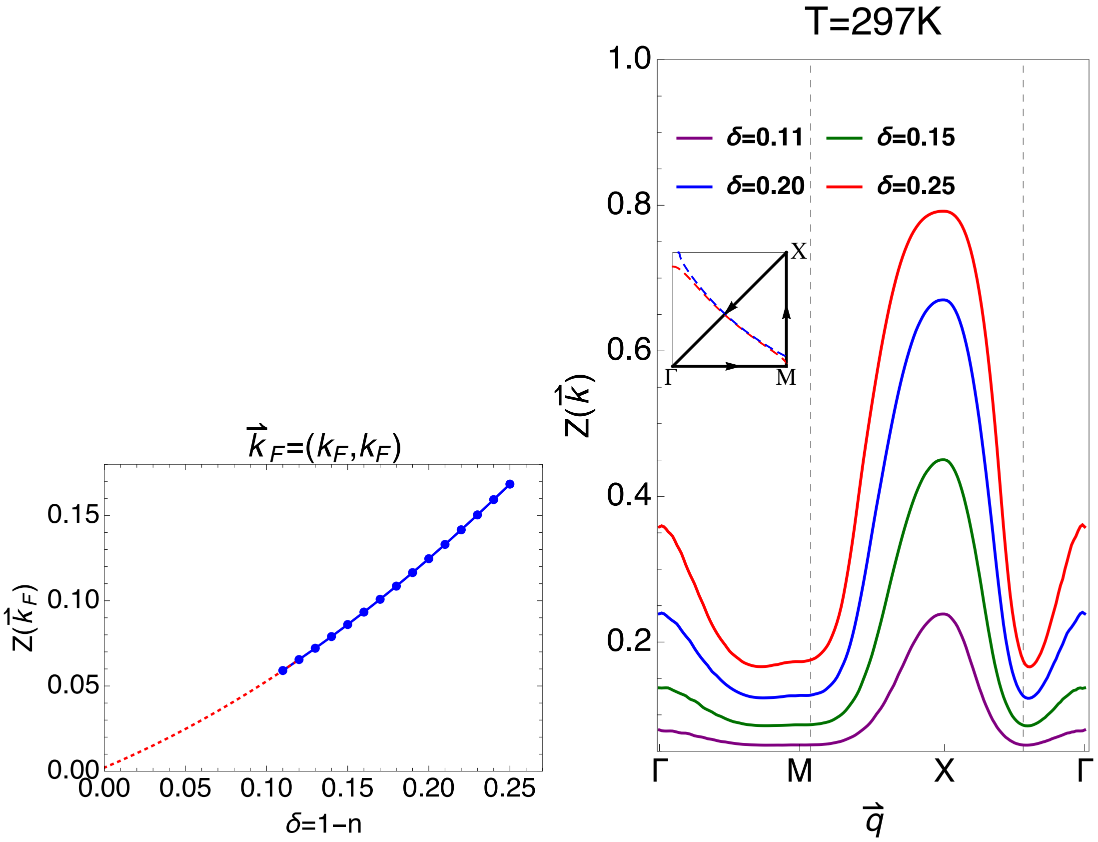

(a)

(b)

Figure 10.3: (**a**) The quasiparticle weight Z plotted as function of doping $\delta = 1 - n$ at the Fermi surface for $T = 297\text{K}$. The blue curve is calculated using Eq. (10.2) and red (dashed) curve is an extrapolation. (**b**) The quasiparticle weight traced along an octant of the BZ including high symmetry points $\Gamma = (0, 0)$, M=$(\pi, 0)$, and $X = (\pi, \pi)$. The gray dashed lines mark the Fermi surface at optimal doping $\delta = 0.15$. The inset shows the path of the wavevector $\vec{q}$ along an octant of the BZ where the dashed blue (red) line marks the Fermi surface for $\delta = 0.25$ (0.11). Early works [60, 13, 82] on models with Hubbard-Gutzwiller-Kanamori type correlations with added long range correlations noted that strong local correlations enhance the effective mass $Z \sim m^*/m \sim \frac{1}{1-n}$ near a Mott transition. Hence quasiparticle weight vanishes as the density approaches half-filling $n = 1$.

10.4 Static Screening, Compressibility χ_{comp} and Screening Length λ_s

At low frequencies $\omega \to 0$ and in the long-wavelength limit $|\vec{q}| \ll 1$, the screened susceptibility $\widetilde{\chi}_{\rho\rho}$ defined in Eq. (8.19) equals the thermodynamic derivative

$$\lim_{q\to 0}\lim_{\omega\to 0} \widetilde{\chi}_{\rho_q\rho_{-q}}(\vec{q},\omega) = q_e^2 \frac{dn}{d\mu} N_s \ . \tag{10.4}$$

In view of the connection with the compressibility Eq. (10.8), this is often called the *compressibility sum-rule.* This gives the compressibility sum-rule, i.e. the screening limit of the dielectric constant [54, 60, 82]

$$\lim_{q\to 0}\lim_{\omega\to 0} \varepsilon(\vec{q},\omega) = 1 + V(\vec{q}) N_s \frac{dn}{d\mu} \tag{10.5}$$

Thus in 3-d and 2-d we get the exact result:

$$\varepsilon \to 1 + \frac{q_s^2}{|\vec{q}|^2}, \ \ \text{(3-d) with } q_s^2 = \frac{4\pi q_e^2}{\varepsilon_\infty}\frac{dn}{d\mu} \tag{10.6}$$

$$\varepsilon \to 1 + \frac{q_s}{|\vec{q}|}, \ \ \text{(2-d) with } q_s = \frac{2\pi q_e^2}{\varepsilon_\infty}\frac{dn}{d\mu} \tag{10.7}$$

Using the thermodynamic relation for compressibility χ_{comp}

$$\chi_{comp} = \frac{1}{n^2}\frac{dn}{d\mu}, \tag{10.8}$$

the screening length $\lambda_s = 2\pi/q_s$ can thus be related to the compressibility χ_{comp}. Strongly correlated systems near half filling display a reduced compressibility, and are therefore expected to show very poor screening, i.e. $\lambda_s \gg 1$ (we set the lattice constant $a_0 = 1$).

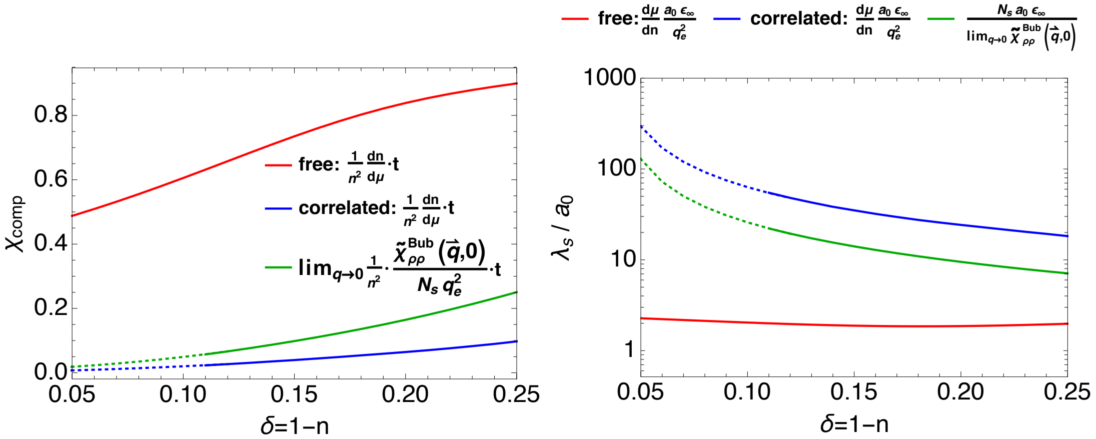

Figure 10.4: (**a**) The compressibility Eq. (10.8) and (**b**) the screening length Eq. (10.7) versus doping $\delta = 1 - n$, where the blue curve is the correlated case and the red curve is for the uncorrelated (bare band) case. In the correlated case the derivative $\frac{dn}{d\mu}$ is found numerically from the computed $\mu(n)$ curve. The dashed lines represent the extrapolation to $\delta = 0$. The green curve gives the static uniform limit of the susceptibility $\frac{1}{q_e^2 N_s}\lim_{\vec{q}\to0}\widetilde{\chi}^{\text{Bub}}_{\rho\rho}(\vec{q},0)$ [Eq. (9.1)]. If an exact calculation, going beyond the bubble approximation were possible, the green curve would coincide with the blue one.

In Fig. 10.4 we plot (a) the compressibility using Eq. (10.8) and (b) the screening length from Eq. (10.7) as a function of doping $\delta = 1-n$. We note that the discrepancy between the static uniform limit of $\widetilde{\chi}_{\rho\rho}$ and the thermodynamic result in the sumrule Eq. (10.4) is quite small. In panel (b) we observe that as we approach the Mott limit $\delta = 0$, the screening in the correlated case very poor whereas the screening in the free case which uses a standard RPA calculation is unchanged.

In Fig. 10.5 we display the momentum dependence of the static susceptibility along the three principal directions at $T = 297$K at a density $n = 0.85$. For comparison we also display the bare (uncorrelated) static susceptibility using Eq. (8.16). Correlations are seen to suppress the magnitudes of the susceptibilities as expected. Somewhat unexpectedly, the relative locations of the three curves, corresponding to different direction in the k-space is strong.

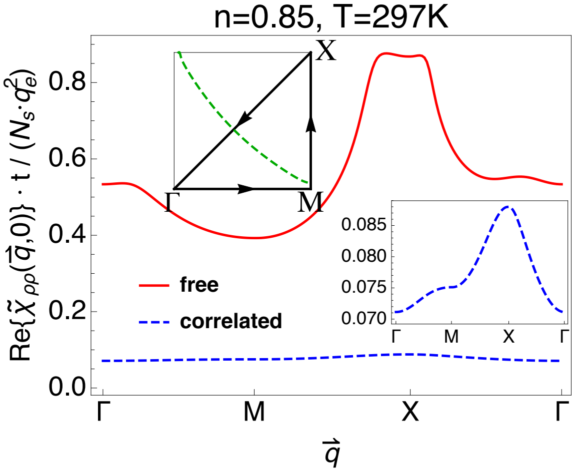

Figure 10.5: The wavevector dependence of the ECFL static susceptibility $\widetilde{\chi}^{(I)}(\vec{q},0)$ Eq. (9.9) dashed (blue) line and the (noninteracting) band structure case solid (red) line using Eq. (8.16) for different paths along the BZ. The inset shows a magnification of correlated case. The density $n = 0.85$ and q is the relevant component of $\vec{q}$ connecting the (high symmetry) points $\Gamma = (0,0), X = (\pi,\pi), M = (\pi,0)$ in the 2-d square lattice BZ.

10.5 Static susceptibility correction

In Fig. 10.6, we compare the computed $\kappa(\vec{q})$, with the static $\widetilde{\chi}_{WW}(\vec{q},0)/N_s$ obtained from Eq. (9.2), using the ECFL Green's function. We observe that they are almost identical over the entire Brillouin zone. Their identity is required in order to get a finite limiting behavior for $\widetilde{\chi}_{\rho\rho}$ at $\omega = 0$ in Eq. (8.3). To enforce this behavior exactly in our numerics, we insert the ratio $\kappa(\vec{q})/\widetilde{\chi}_{WW}(\vec{q},0) \approx 1$ in the second term of Eq. (8.13).

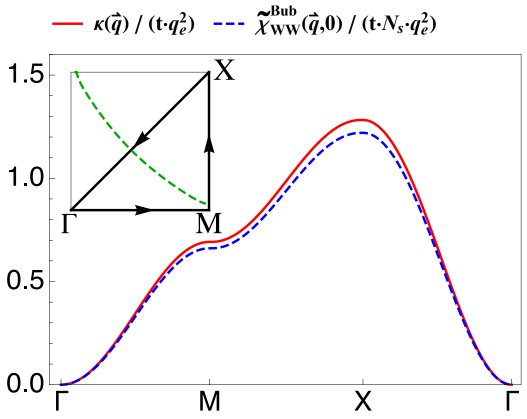

Figure 10.6: The dimensionless functions $\frac{1}{tq_e^2}\kappa(\vec{q})$ from Eq. (8.4) and $\frac{1}{tq_e^2 N_s}\widetilde{\chi}^{\rm Bub}_{WW}(\vec{q},0)$ from Eq. (9.2) plotted over the Brillioun zone are approximately identical for a system at $n = 0.85$ and $T = 297$K. These two curves should coincide identically in an exact calculation of the susceptibility that goes beyond the bubble approximation. The ratio between the two curves in Eq. (9.5) corrects for this discrepancy.

10.6 Novel Self-Energy $\Psi(\vec{q},\omega)$

This self-energy Ψ can be found from $\widetilde{\chi}_{\rho\rho}(\vec{q},\omega)$, if the latter is known, by inversion of Eq. (8.19), and can be expressed formally in terms of the higher moments $\widetilde{\omega}^{(2j+1)}(\vec{q})$ using Eq. (C.8) [68, 52, 23] as

$$\Psi(\vec{q},\omega) = \left(\frac{q_e^2 N_s}{\widetilde{\chi}_{\rho\rho}(\vec{q},0)} - \frac{\omega^2}{\widetilde{\omega}^{(1)}(\vec{q})} - \frac{q_e^2 N_s}{\widetilde{\chi}_{\rho\rho}(\vec{q},\omega)}\right), \tag{10.9}$$

and using the two expressions Eqs. (9.4) and (9.5) we get two different self-energies Ψ_A and Ψ_B (Eqs. (9.6) and (9.7)).

In Fig. 10.7 panels (a-e) we compare the real and imaginary parts of the self-energies Ψ_A, Ψ_B calculated from Eqs. (9.6) and (9.7). We note that $\operatorname{Im}\Psi_A$ contains a very small quasiparticle contribution as seen in panel (a), characterized by a linear behavior $\Psi'' \propto \frac{\pi\omega}{|\vec{q}|v_F}$ for $\omega < |\vec{q}|v_F Z$, while this linear behavior is absent in $\operatorname{Im}\Psi_B$. The construction of $\widetilde{\chi}^{(II)}$ in Eq. (9.10) adds a piece $\delta\Psi_{QP}$ representing the small quasiparticle contribution to the imaginary part of Ψ_B, and recomputes the real part using causality. We display the ω dependence of Ψ_B and $\Psi_B + \delta\Psi_{QP}$ in panels (b), (c), (d) and (f) of Fig. 10.7.

In Fig. 10.8 panel (a) we display $\mathrm{Im}\,\Psi_B$ at different $\vec{q}$ as functions of ω, and note that these collapse to a single curve over the Brillioun zone, when multiplied by $\widetilde{\omega}^{(1)}(\vec{q})$. The $\mathrm{Im}\{\Psi_B + \delta\Psi_{QP}\}$ at different $\vec{q}$ differ in the low ω region, due to the presence of the quasi-particle contributions, but do collapse to a single curve at higher frequencies, as seen in panel (b).

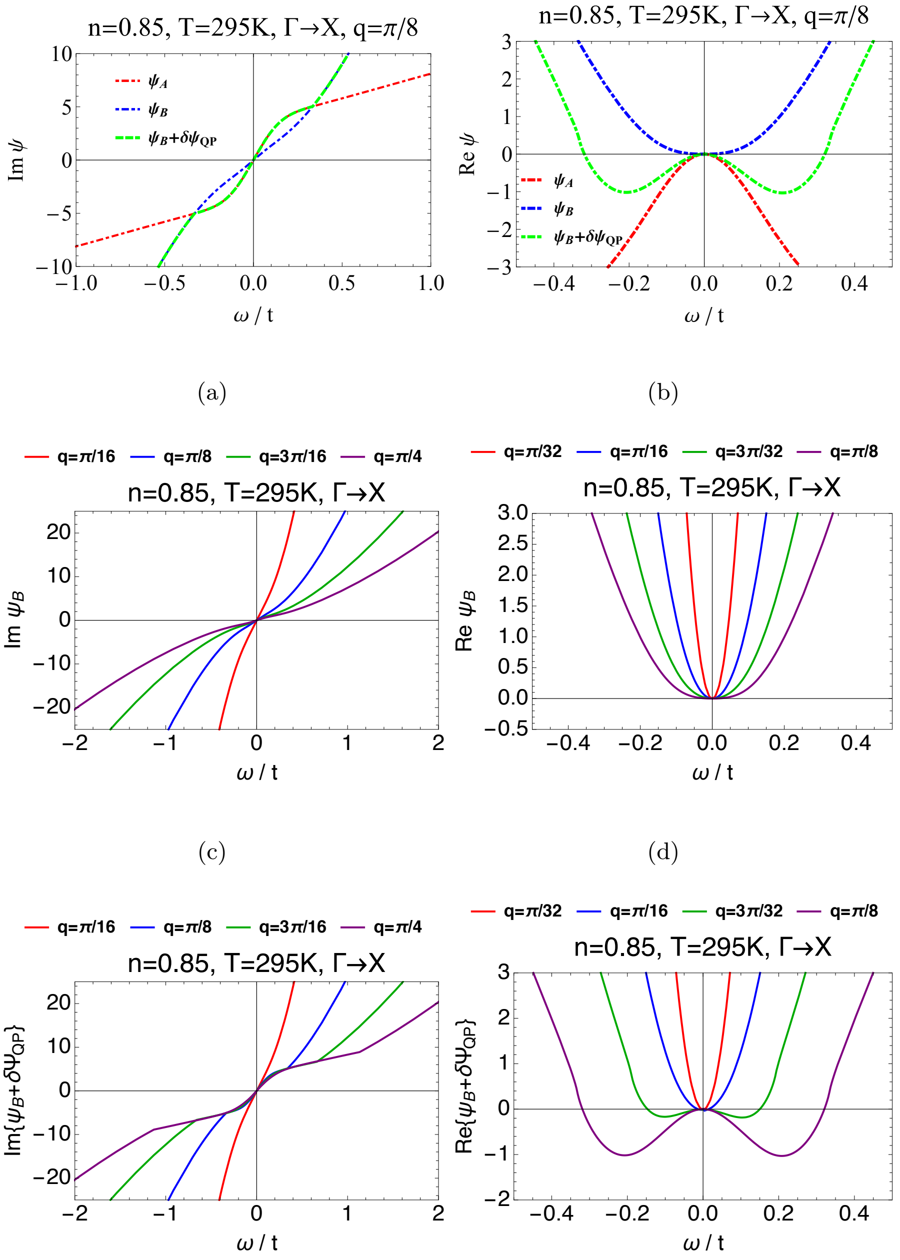

(a) (b)

(c) (d)

(e) (f)

Figure 10.7: The complex self-energy $\Psi(\vec{q},\omega)$ of the susceptibility $\widetilde{\chi}_{\rho\rho}(\vec{q},\omega)$ as defined Eq. (8.19). We show Eqs. (9.6), (9.7), (9.11) and (9.12) at density $n = 0.85$ and $T = 297$K along the $\Gamma \to X$ direction where $\vec{q} = (q, q)$. Panels (**a**) and (**b**) show the effects of adding the quasiparticle contribution $\delta\Psi_{QP}$ to Ψ_B in the imaginary and real parts of the self-energy. Panels (**c**) and (**d**) show the imaginary and real parts of $\Psi_B(\vec{q},\omega)$ and panels (**e**) and (**f**) shows the imaginary and real parts of $\Psi_B(\vec{q},\omega) + \delta\Psi_{QP}(\vec{q},\omega)$ for a few q values.

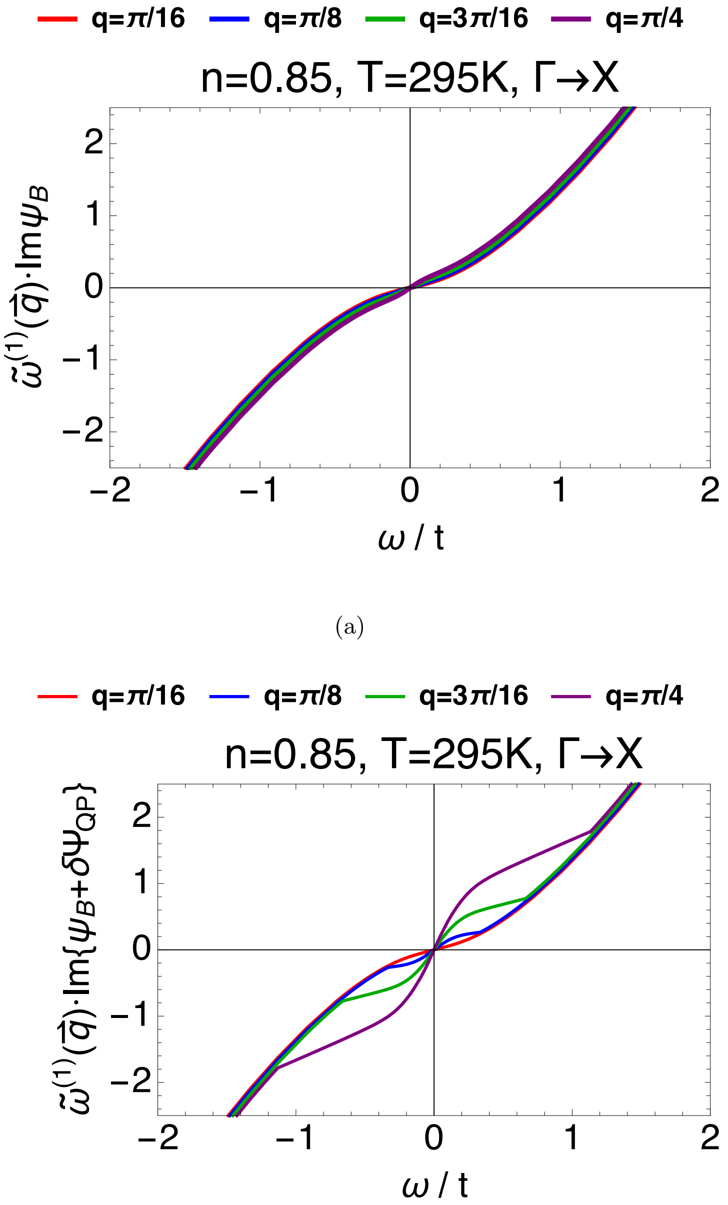

(a)

(b)

Figure 10.8: (**a**) The imaginary part of the self-energy $\Psi_B(\vec{q},\omega)$ [Eq. (9.7)] at different values of $\vec{q}=(q,q)$ (in $\Gamma \to X$ direction) coincide and collapse to a single curve when scaled by the first moment $\widetilde{\omega}^{(1)}(\vec{q})$ [Eq. (C.4)]. (**b**) For $\Psi_B(\vec{q},\omega)+\delta\Psi_{QP}(\vec{q},\omega)$ the imaginary part of the self-energy collapses also coincides, but only at high frequencies beyond the energy scale of the quasiparticle excitations. From Eq. (8.24) we see that the (on-shell) product $\widetilde{\omega}^{(1)}(\vec{q})\,\mathrm{Im}\,\Psi(\vec{q},\Omega_p(\vec{q}))$ equals the squared width $\Gamma_p^2(\vec{q})$ of the peak in $\mathrm{Im}\,\widetilde{\chi}_{\rho\rho}(\vec{q},\omega)$, located at $\omega \sim \Omega_p(\vec{q})$. On the other hand, the (off-shell) case Eq. (8.19) for generic ω describes the almost $\vec{q}$ independent fall off away from the peak.

10.7 Charge Density Susceptibility Approximations

In Fig. 10.9 we compare two approximations for the imaginary part of the irreducible (screened) susceptibilities $\mathrm{Im}\,\widetilde{\chi}^{(I)}$ (solid red line) and $\mathrm{Im}\,\widetilde{\chi}^{(II)}$ (blue dashed lines), i.e., Eqs. (9.9) and (9.10). As expected the quasiparticle contribution at low frequencies is roughly linear in ω.

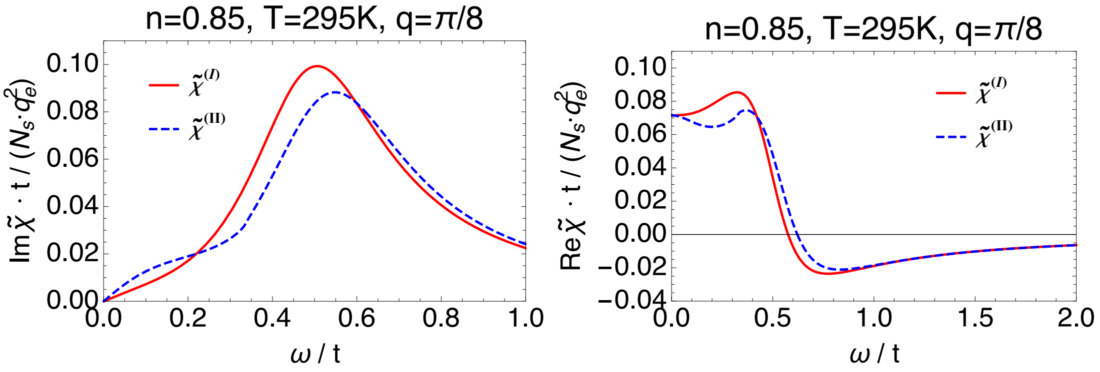

(a)

(b)

Figure 10.9: A comparison between the (**a**) imaginary and (**b**) real parts of the $\widetilde{\chi}$ susceptibilities $\widetilde{\chi}^{(I)}$ and $\widetilde{\chi}^{(II)}$ from Eqs. (9.9) and (9.10). The quasiparticle contribution is visible in (**a**) at low frequencies and is roughly linear in ω.

10.8 Characteristic frequency scale $\Omega_p(\vec{q})$ revisited

We show the density and temperature evolutions of the screened susceptibility approximations $\widetilde{\chi}^{(I)}$ (dashed) and $\widetilde{\chi}^{(II)}$ (solid) over the ranges $n = 0.8, 0.825, 0.85$ and $T = 99, 198, 295$K in the two principle directions $\Gamma \rightarrow X$ (see Fig. 10.10) and $\Gamma \rightarrow M$ (see Fig. 10.11). In all cases we observe that the high ω fall off of $\mathrm{Im}\,\widetilde{\chi}$ is $\sim \frac{1}{\omega^2}$, while the curves turn-around at low frequencies to vanish as $\omega \rightarrow 0$. This turn-around occurs at the peak frequency $\Omega_p(\vec{q})$ discussed in Eq. (8.23), and displayed in Fig. 10.12.

The magnitude of the turn-around frequency $\Omega_p(\vec{q})$, typically a small fraction of t can, depending upon the choice of the hopping parameter t, be very small. We can estimate this further as follows. Using Eqs. (8.21) and (8.23) together with the expression for the first moment $\widetilde{\omega}^{(1)}(\vec{q})$ in Eqs. (C.12), (C.16) and (C.17) we express $\Omega_p(\vec{q})$ explicitly as a function of $\vec{q}$. At small $\vec{q}$ this simplifies further to

$$\lim_{\vec{q}\to 0} \Omega_p(\vec{q}) = |\vec{q}|\sqrt{\frac{\mathcal{T}}{q_e^2}\frac{d\mu}{dn}}, \tag{10.10}$$

where the velocity $\sqrt{\frac{\mathcal{T}}{q_e^2}\frac{d\mu}{dn}}$ is determined by the ratio of $\mathcal{T}$ Eq. (C.18) that shrinks as the density $n \to 1$, and the compressibility Fig. 10.4. We comment further on this turn-around when discussing Figs. 10.18 and 10.20.

Given the interesting role played by this energy scale $\Omega_p(\vec{q})$, a natural question is whether it has a more direct origin and interpretation. For this purpose we construct a positive definite spectral-shape function $\varphi(\vec{q},\omega)$ from the complex susceptibility $\widetilde{\chi}_{\rho\rho}(\vec{q},\omega)$ as

$$\varphi(\vec{q},\omega) = \frac{1}{\widetilde{\chi}_{\rho\rho}(\vec{q},0)}\left[\frac{\mathrm{Im}\,\widetilde{\chi}_{\rho\rho}(\vec{q},\omega)}{\pi\omega}\right]. \tag{10.11}$$

Using a dispersion relation for $\widetilde{\chi}_{\rho\rho}(\vec{q},\omega)$ Eq. (C.7), we verify the normalization condition

$$\int_{-\infty}^{\infty} d\omega\, \varphi(\vec{q},\omega) = 1, \tag{10.12}$$

and also the even-ness $\varphi(\vec{q},-\omega) = \varphi(\vec{q},\omega)$. The second frequency moment of this spectral-shape function is given by

$$\int_{-\infty}^{\infty} d\omega\, \omega^2\, \varphi(\vec{q},\omega) = \Omega_p^2(\vec{q}), \tag{10.13}$$

where we used Eqs. (8.22), (C.7), (C.8) and (C.10) to relate the result of the integration to the expression in Eq. (8.23). Thus $\Omega_p(\vec{q})$ provides the lowest level characterization of the dynamics of $\widetilde{\chi}_{\rho\rho}(\vec{q},\omega)$. As noted above, our theory identifies this energy as the peak frequency, or equivalently the turn-around scale for $\mathrm{Im}\,\widetilde{\chi}_{\rho\rho}(\vec{q},\omega)$ (see Fig. 10.14).

In Fig. 10.13(**a**) we plot $\Omega_p(\vec{q})$ for $n = 0.85$ and $T = 297\mathrm{K}$. The red curve $\Omega_p^{corr}(\vec{q})$ is calculated exactly as show in Eq. (8.23) and for blue dashed curve $\Omega_p^{uncorr}(\vec{q})$, the thermodynamic correction factor is set to unity, i.e., $\frac{dn}{d\mu} = \lim_{\vec{q}\to 0}\widetilde{\chi}_{\rho\rho}(\vec{q},0)$. Note that $\Omega_p^{(I,II)}(\vec{q}) = \lim_{\omega\to 0}\Omega^{(I,II)}(\vec{q},\omega)$ and $\Omega_p^{(I)} = \Omega_p^{(II)}$ in the limit $\omega \to 0$. The observed effect of including the thermodynamic correction is a general shift of the peak frequency to higher energies. In Fig. 10.13(**b**) we plot the width of the peak $\Gamma(\vec{q})$ for $n = 0.85$ and $T = 297\mathrm{K}$. We not that for small $\vec{q}$ the width of the peaks coincide and separate as $\vec{q}$ grow, and the corrected peaks have wider widths.

In experiments a reasonable estimate of $\Omega_p(\vec{q})$ might be obtained by an integration over a *finite* frequency window in Eq. (10.13), if $\varphi(\vec{q},\omega)$ falls off rapidly with ω[8]. From Eqs. (10.10), (10.13) and (10.14), we see that this energy scale results from a ratio of two diminishing scales, the bandwidth reduction and the compressibility reduction, both due of the Gutzwiller-Hubbard correlations. In Fig. 10.12 we calculate the important characteristic energy $\Omega(\vec{q},\omega)$ for both approximations in Eq. (9.9) and Eq. (9.10) at optimal density $n = 0.85$ and room temperature $T = 295\mathrm{K}$ in the $\Gamma \to X$ direction.

---

[8] For this purpose it may be more useful to rewrite Eq. (10.13) in the form

$$\Omega_p^2(\vec{q}) = \frac{\int_{-\infty}^{\infty} d\omega\,\omega\,\mathrm{Im}\,\widetilde{\chi}_{\rho\rho}(\vec{q},\omega)}{\int_{-\infty}^{\infty} d\omega\,\frac{1}{\omega}\,\mathrm{Im}\,\widetilde{\chi}_{\rho\rho}(\vec{q},\omega)}. \tag{10.14}$$

For the purpose of estimation, one may perform both integrations over the finite range of available frequencies. The estimate can be quite reasonable if the range is not too small.

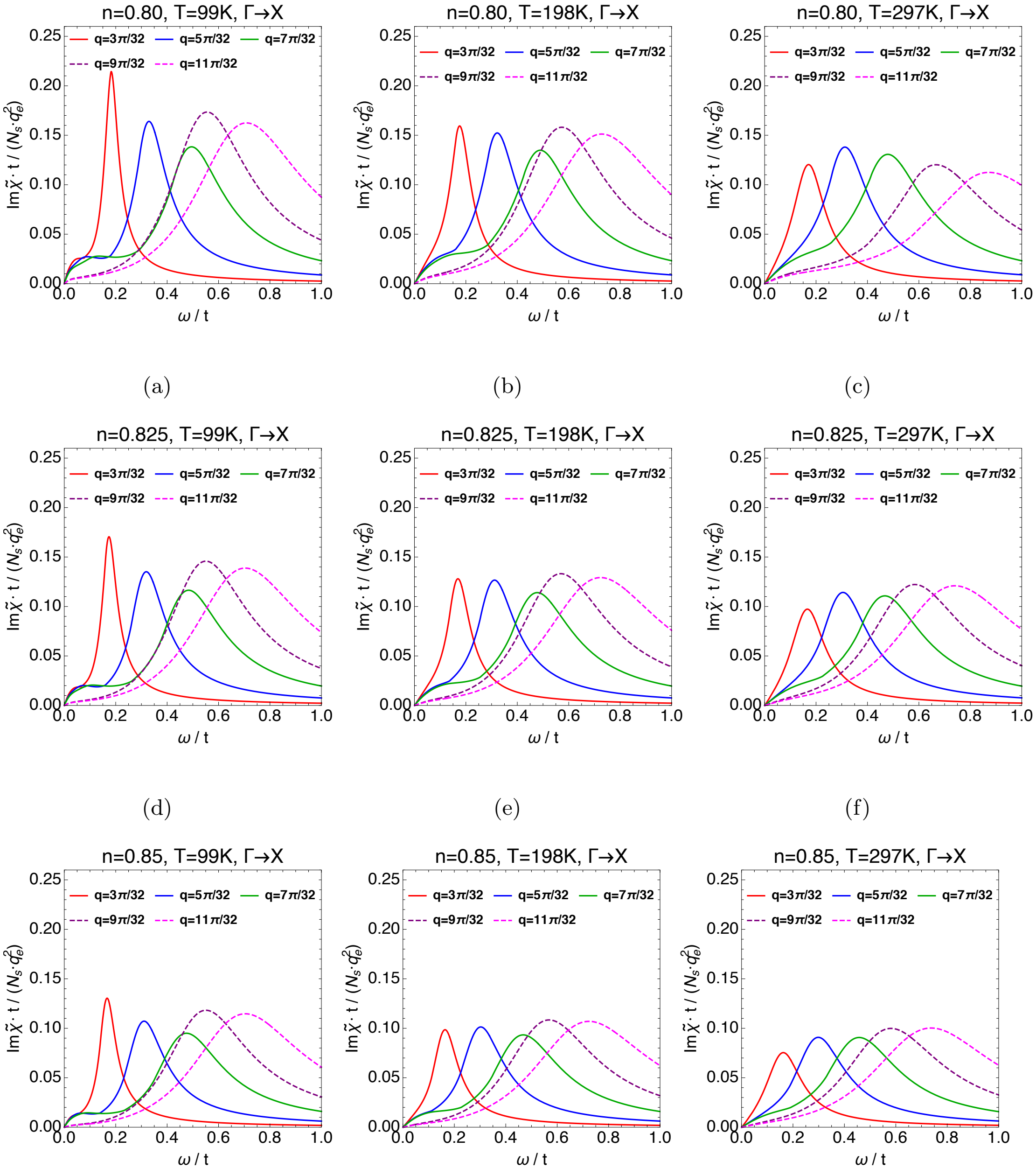
n=0.80, T=99K, Γ→X

n=0.80, T=198K, Γ→X

n=0.80, T=297K, Γ→X

n=0.825, T=99K, Γ→X

n=0.825, T=198K, Γ→X

n=0.825, T=297K, Γ→X

n=0.85, T=99K, Γ→X

n=0.85, T=198K, Γ→X

n=0.85, T=297K, Γ→X

(a) (b) (c)

(d) (e) (f)

(g) (h) (i)

Figure 10.10: The two susceptibilities $\mathrm{Im}\,\widetilde{\chi}^{(I)}$ (dashed) [Eq. (9.9)] and $\mathrm{Im}\,\widetilde{\chi}^{(II)}$ (solid) [Eq. (9.10)] at densities $n = 0.8, 0.825, 0.85$ and temperatures $T = 99, 198, 297\mathrm{K}$ in the $\Gamma \rightarrow X$ direction where $\vec{q} = (q, q)$. These curves show a $\vec{q}$ dependent peak at $\Omega_p(\vec{q}) \sim \Omega(\vec{q}, 0)$ from Eq. (8.23), detailed in Fig. 10.12.

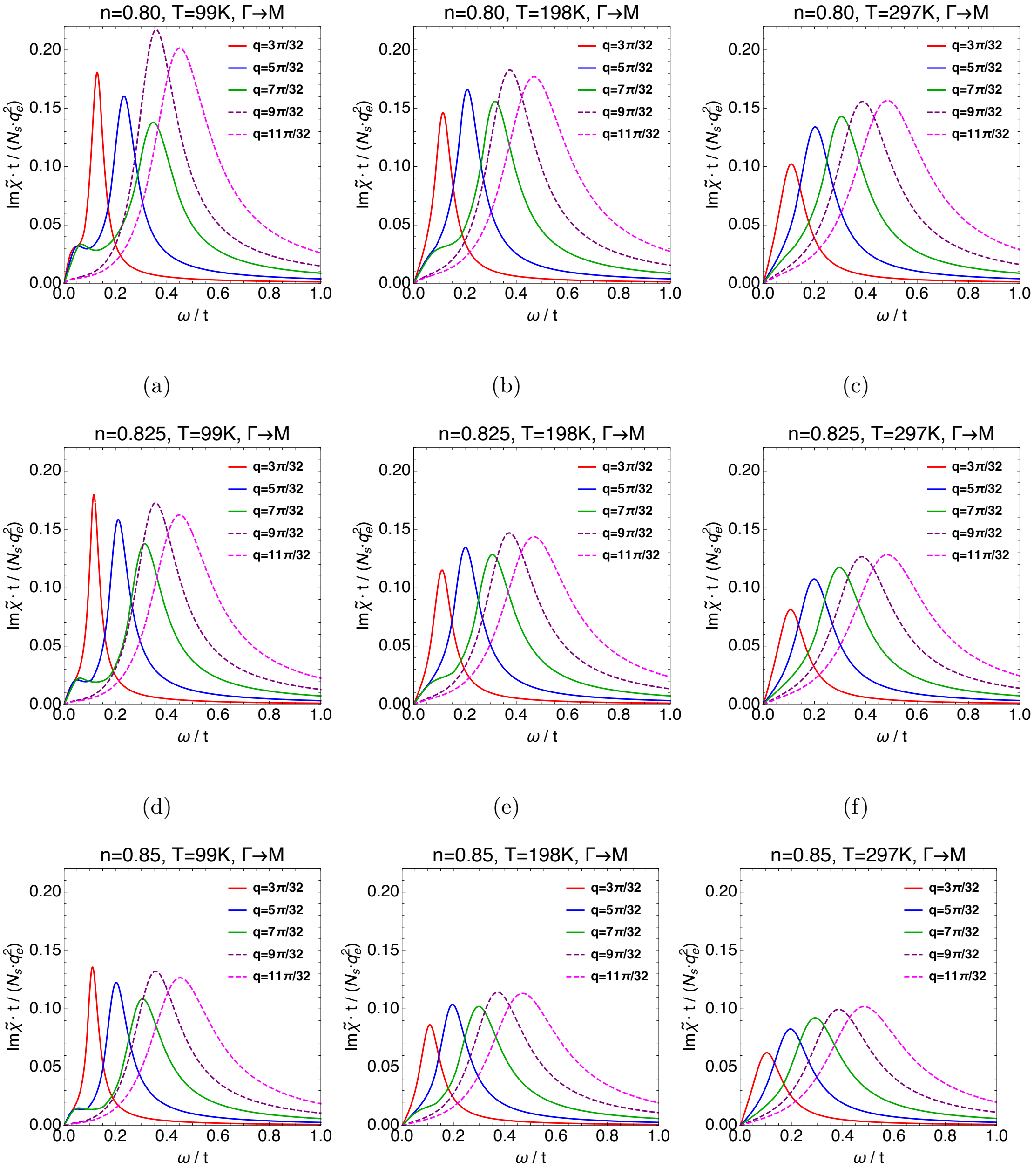

(a) (b) (c)

(d) (e) (f)

(g) (h) (i)

Figure 10.11: The two susceptibilities Im $\widetilde{\chi}^{(I)}$ (dashed) [Eq. (9.9)] and Im $\widetilde{\chi}^{(II)}$ (solid) [Eq. (9.10)] at densities $n = 0.8, 0.825, 0.85$ and temperatures $T = 99, 198, 297$K in the $\Gamma \to M$ direction where $\vec{q} = (q, 0)$.

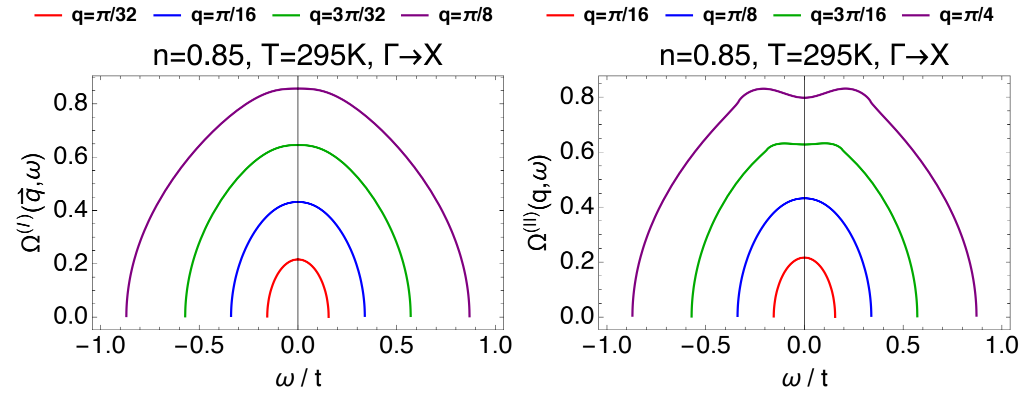

(a) (b)

Figure 10.12: The emergent energy scale Eq. (8.21) in unites of t. In panel (**a**) $\Omega^{(I)}$ uses Eq. (9.9), and panel (**b**) $\Omega^{(II)}$ uses Eq. (9.10), leading to similar energies. Here $n = 0.85$ and $T = 297$K with $\vec{q} = (q, q)$ in $\Gamma \to X$. The peaks of $\Omega(\vec{q}, \omega)$ are located at the roots of $\operatorname{Im} \widetilde{\chi}_{\rho\rho}(\vec{q}, \omega)$ are located at the roots of $\omega^2 = \Omega^2(\vec{q}, \omega)$, or at a cruder level, at the energy scale $\Omega_p(\vec{q}) \sim \Omega(\vec{q}, 0)$. It therefore represents the turn-around energy scale (i.e., peak frequencies) observed in Figs. 10.10, 10.11, 10.18 and 10.20.

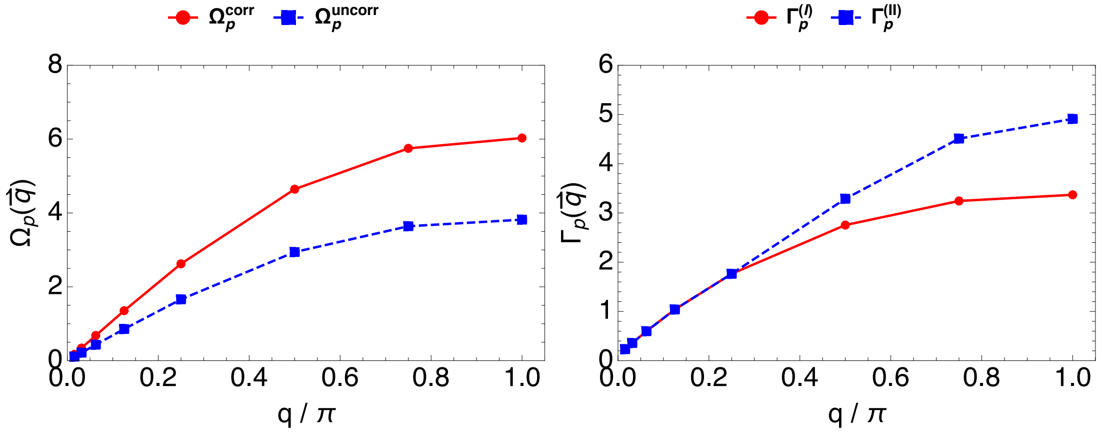

(a) (b)

Figure 10.13: Panel (**a**) The peak energy scale $\Omega_p(\vec{q})$ [Eq. (8.23)] and panel (**b**) the width of the peaks $\Gamma_p(\vec{q})$ [Eq. (8.24)]. In panel (**a**) the solid red curve $\Omega_p^{\text{corr}}(\vec{q})$ is defined exactly as presented in Eq. (8.23) and for the blue dashed curve $\Omega_p^{\text{uncorr}}(\vec{q}) \equiv \lim_{\omega \to 0} \Omega^{(I,II)}(\vec{q}, \omega)$. Note we set $\frac{dn}{d\mu} = \lim_{\vec{q} \to 0} \widetilde{\chi}_{\rho\rho}(\vec{q}, 0)$ for both panels and we note that $\Omega_p^{(I)} = \Omega_p^{(II)}$. In panel (**b**) the red solid curves $\Gamma_p^{(I)}$ uses $\Psi = \Psi_B$ and the blue dashed curve $\Gamma_p^{(II)}$ uses $\Psi = \Psi_B + \delta\Psi_{QP}$. These computation used $L_x \times L_y = 128 \times 128$. Here $n = 0.85$ and $T = 297$K and $\vec{q} = (q, q)$ is along $\Gamma \to X$.

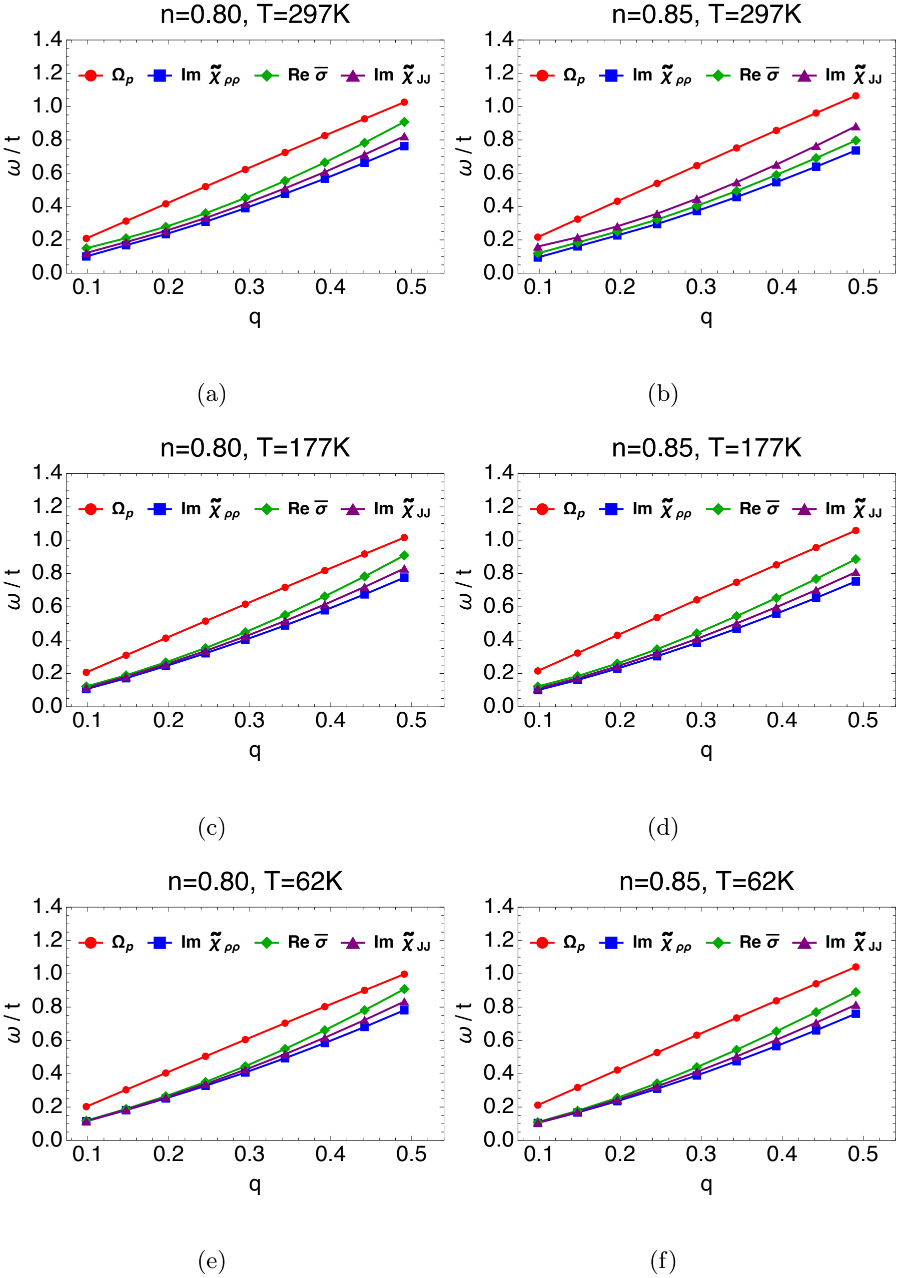

(a)

(b)

(c)

(d)

(e)

(f)

Figure 10.14: The characteristic frequency scale $\Omega_p(\vec{q})$ (red) Eq. (10.13) and the turn-around frequency (i.e., peak frequency) for Im $\widetilde{\chi}_{\rho\rho}$ (blue), Re $\bar{\sigma}$ (green) and Im $\widetilde{\chi}_{JJ}$ (purple) are compared. This computation used $L_x \times L_y = 128 \times 128$. The screened susceptibility $\widetilde{\chi}_{\rho\rho}$ is approximated using $\widetilde{\chi}^{(I)}$. Here the density and temperature is as shown and $\vec{q} = (q, q)$ is along $\Gamma \to X$. The turn-around-frequency is found by computing the numerical derivative of Im $\widetilde{\chi}_{\rho\rho}$, Re $\bar{\sigma}$, Im $\widetilde{\chi}_{JJ}$ and finding the zero crossing in the neighborhood of the peak.

10.9 Dielectric constant approximations $\varepsilon^{(I,II)}(\vec{q},\omega)$

In Fig. 10.15 we display the approximate dielectric functions, computed from Eqs. (9.13) and (9.14) at $n = 0.85$ and $T = 295$K, in the form of $\mathrm{Im}\,\frac{1}{\varepsilon(\vec{q},\omega)}$ [panels (a,c)] and $\mathrm{Re}\,\varepsilon(\vec{q},\omega)$ [panels (b,d)]. The first of these is directly measured in inelastic electron scattering where peaks, if present, signify plasmons. The second is a theoretical curve of a type used to identify plasmons through its zero crossing, and is relevant to certain optical experiments.

In panels (a,c) we observe a linear in ω behavior for sufficiently small ω, owing to the quasiparticle contribution in the self-energy. From panels (b,d) we note that unlike in the RPA calculation [51, 24] for uncorrelated materials, $\mathrm{Re}\,\varepsilon$ crosses the zero line only for large g_c. In Fig. 10.16, we focus on the evolution of the $\varepsilon^{(I)}$ over the ranges $q = \pi/16, \pi/8, 3\pi/16$ and $g_c = 10, 50, 100$ in the two principle directions $\Gamma \to X$ and $\Gamma \to M$. This result might be of use in pinning down the value of g_c in experiments.

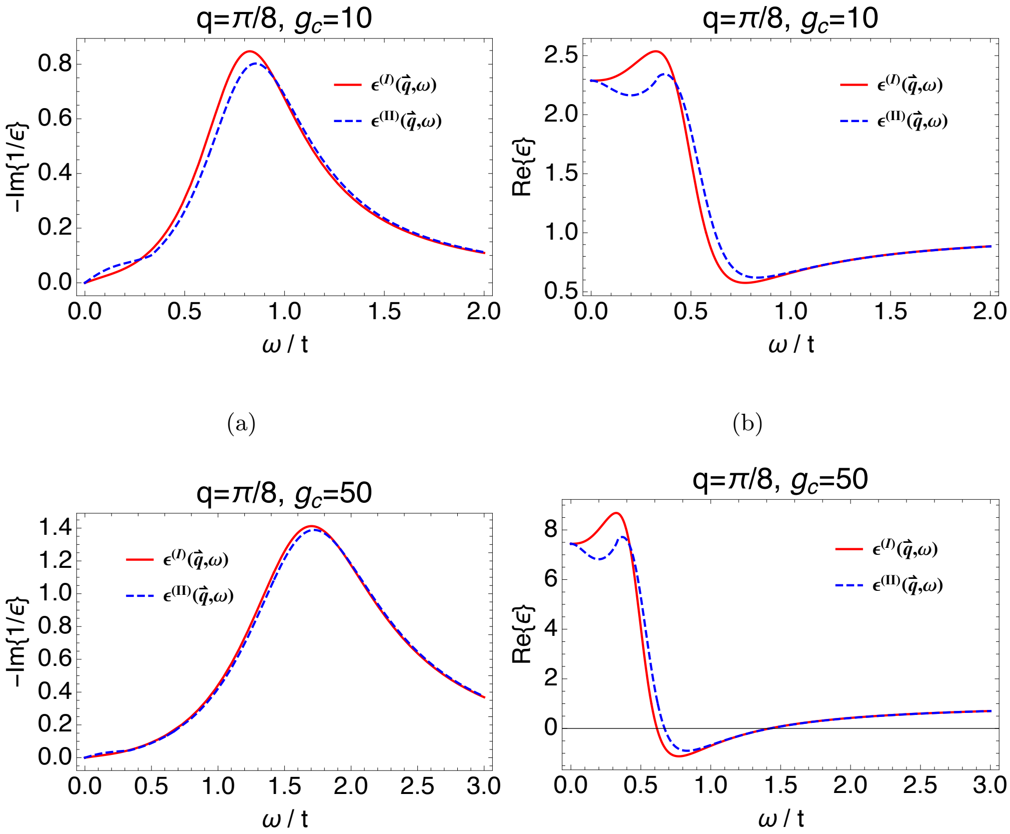

(a)

(b)

(c)

(d)

Figure 10.15: The dielectric function $\varepsilon^{(I)}$ and $\varepsilon^{(II)}$ from Eq. (9.13) for a system at $n = 0.85$ and $T = 297$K with $\vec{q} = (q, q)$ along $\Gamma \to X$. Here panel (**a**), (**c**) is the imaginary part and panel (**b**), (**d**) is the real part for $g_c = 10, 50$ respectively. The curves $\mathrm{Re}\,\varepsilon^{(I,II)}$ do not vanish in this range at $g_c = 10$ [panel(**d**)], while they do so when $g_c = 50$ [(panel(**d**))]. This is unlike plasmon in weakly interacting electron gas discussed in books Ref. [24], where a zero crossing accurately determines the plasmon.

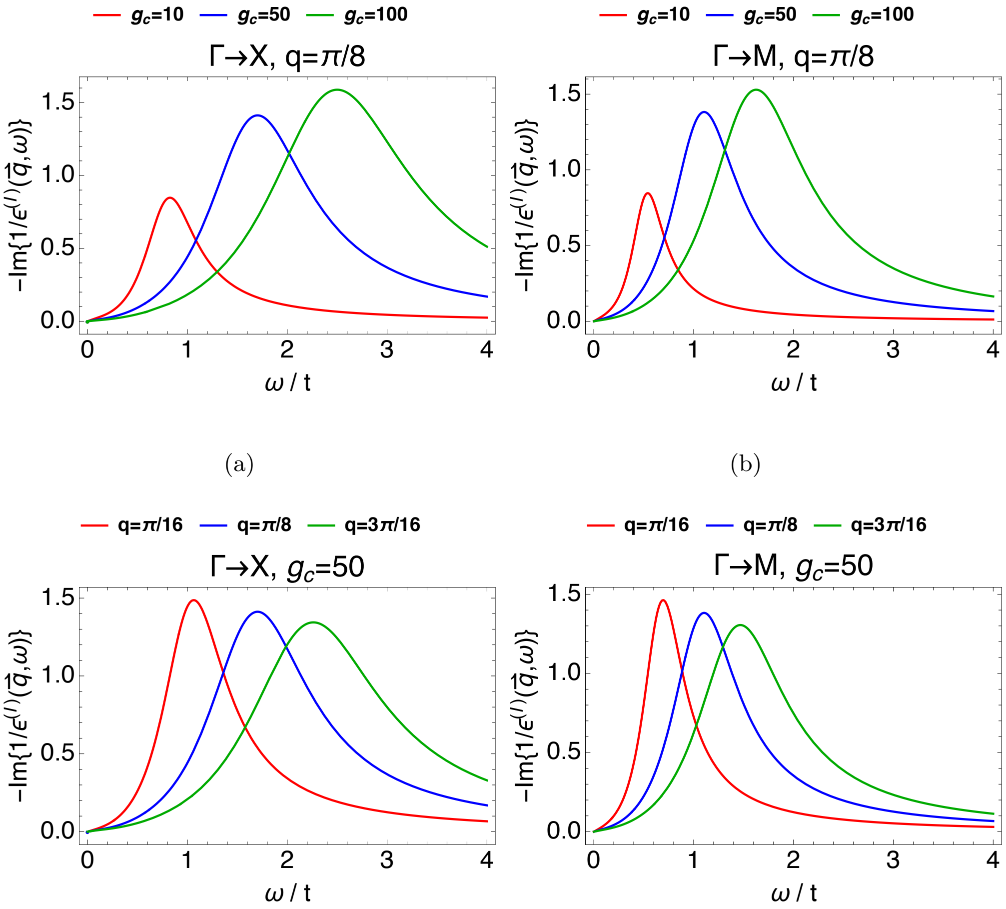

(a) (b)

(c) (d)

Figure 10.16: The imaginary part of the inverse dielectric function [Eq. (9.13)] at $n = 0.85$ and $T = 297\text{K}$. Panels (**a**) $\vec{q} = (\frac{\pi}{8,\frac{\pi}{8}})$ and (**b**) $\vec{q} = (\frac{\pi}{8}, 0)$ illustrate the variation of the plasmon peak with g_c. Panels (**c**) $\Gamma \to X$ and (**d**) $\Gamma \to M$ direction exhibit the peak variation with $\vec{q}$ at $g_c = 50$ in the respective directions.

10.10 Plasmon Dispersion in $\varepsilon(q)$ and f-sumrule

In the limit $\omega \gg t$ the behavior of the dielectric function is easily read off from Eq. (8.15). Neglecting $\frac{\widetilde{\chi}_{WW}(\vec{q},\omega)}{\widetilde{\chi}_{WW}(\vec{q},0)}$ compared to unity, we get

$$\lim_{\omega \gg t} \varepsilon(\vec{q},\omega) = 1 - \frac{\omega_p^2(\vec{q})}{\omega^2}. \tag{10.15}$$

In both 3-d and 2-d, the plasma frequency is given in terms of κ by

$$\omega_p^2(\vec{q}) = \frac{N_s}{q_e^2} V(\vec{q}) \kappa(\vec{q}). \tag{10.16}$$

The f-sumrule for the optical conductivity is expressible in terms of either $\mathcal{T}$ or plasma frequency as

$$\int_{-\infty}^{\infty} \frac{d\omega}{\pi} \mathrm{Re}\, \sigma(\omega) = \mathcal{T} = \frac{\varepsilon_\infty}{4\pi} \omega_p^2(0). \tag{10.17}$$

Let us note that the effect of Gutzwiller type short range correlations is seen most directly in expressions for $\mathcal{T}$ in Eq. (C.18) and in Fig. 10.17. We discuss in Appendix C.2 the connection of this result with the first frequency sum rule for the electron structure function.

In Fig. 10.17 panel (**a**) we display $\kappa(\vec{q})$ Eq. (8.4) at two densities $n = 0.85$ and $n = 0.8$ using the angular averages shown in Table 10.1 in Eq. (C.16), and Eqs. (C.10) and (C.12) relating it to the first frequency moment of the structure function $S(\vec{q},\omega)$. In Fig. 10.17 panel (**b**) displays the 2-d plasmon spectrum. It is found from κ and Eqs. (7.6) and (10.16). We display the plasma energy along the principal directions in the Brillouin zone. It displays the expected acoustic $\sqrt{|\vec{q}|}$ behavior at low $\vec{q}$.

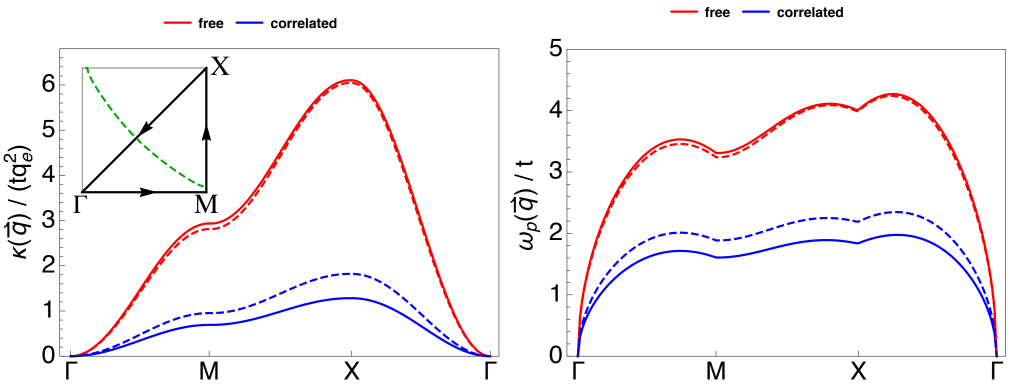

(a)

(b)

Figure 10.17: (**a**) The function $\frac{1}{tq_e^2}\kappa(\vec{q})$ [Eq. (8.4)], or equivalently the first moment $\widetilde{\omega}^{(1)}(\vec{q})/t$ [Eq. (C.12)] over the BZ. We used Eq. (C.16) at two densities $n = 0.85$ (solid curves) and $n = 0.8$ (dashed curves) for the uncorrelated (red) and correlated (blue) systems at $T = 297$K. Recall from Eqs. (C.10) and (C.12), that $\widetilde{\omega}^{(1)}(\vec{q})$, the first moment per site of the structure function $S(\vec{q}, \omega)$ can be directly inferred from experiments. (**b**) The plasmon dispersion $\omega_p(\vec{q})$ in 2-d from Eqs. (7.6) and (10.16) for the same parameters, and $\varepsilon_\infty = 4.5$, for the uncorrelated (red) and correlated (blue) systems. The reduction of the plasmon energy scale between the two sets is the effect of correlations.

n		Uncorrelated	Correlated
0.80	$\langle \cos k_x \rangle_{ave}$	0.188847	0.056881
	$\langle \cos k_x \cos k_y \rangle_{ave}$	0.032757	0.00661296
0.85	$\langle \cos k_x \rangle_{ave}$	0.190954	0.0400778
	$\langle \cos k_x \cos k_y \rangle_{ave}$	0.018181	-0.0079378

Table 10.1: The averages used in Eq. (C.16) to calculate $\kappa(\vec{q})$ in Fig. 10.17. The flattened distribution function m_k in Fig. 10.2 leads the much smaller values of these angular averages for the correlated metal.

10.11 Comparison of $\operatorname{Im}\widetilde{\chi}_{\rho\rho}$, $\operatorname{Re}\bar{\sigma}$ and $\operatorname{Im}\widetilde{\chi}_{JJ}$

We note that the formula in Eq. (8.15) also gives the correct resistivity formula used in studies of the t-J model. Let us first examine the 3-dimensional case with a cubic unit cell, and assume that the electric field polarization is longitudinal, i.e. the current is along $\vec{q}$. From the usual relation between the induced current and the polarization $\vec{J}_{ind} = \dot{\vec{P}}$, and $\vec{P} = \frac{1}{4\pi}(\vec{D} - \vec{E})$ combined with the constitutive relations $\vec{J}_{ind} = \sigma\vec{E}$ and $\vec{D} = \varepsilon\vec{E}$ we obtain $\sigma(q) = \frac{\omega}{4\pi i}(\varepsilon(q) - 1)$ and on using Eq. (8.15)

$$\sigma(\vec{q}, \omega) = \frac{i}{|\vec{q}|^2\,\omega}\left(\kappa(q) - \frac{1}{N_s}\widetilde{\chi}_{WW}(q)\right). \tag{10.18}$$

Using the charge conservation law $W_{\vec{q}} = \vec{q}.\vec{J}_{\vec{q}}$ applicable in the uniform limit $\vec{q} \to 0$, we can relate $\widetilde{\chi}_{WW}$ to $\widetilde{\chi}_{JJ}$ — the screened analog to Eq. (8.7):

$$\text{For } \ |\vec{q}|a_0 \ll 1, \ \ \widetilde{\chi}_{JJ}(\vec{q}, \omega) = \frac{1}{|\vec{q}|^2}\widetilde{\chi}_{WW}(\vec{q}, \omega)\ . \tag{10.19}$$

Let us note an important consequence of Eq. (10.18):

$$\operatorname{Re}\sigma(\vec{q}, \omega) = \frac{1}{\omega N_s}\operatorname{Im}\widetilde{\chi}_{JJ}(\vec{q}, \omega), \tag{10.20}$$

thus relating the dissipative part of conductivity with $\operatorname{Im}\widetilde{\chi}_{JJ}(\vec{q}, \omega)/\omega$. In Eq. (10.20) we have suppressed an implicit prefactor $\frac{1}{a_0}$, which needs modification for quasi 2-dimensional system such as the cuprate materials analyzed in [64, 65]. Here the theory proceeds by assuming that the unit cell is body centered tetragonal instead of cubic. Here a_0 is replaced by c_0, the separation between two copper oxide layers in the simple case of single layer cuprates, so that $c_0 \gg a_0$. The different layers are assumed to be decoupled as far as electron hopping is concerned, while their polarizations add up. We then obtain an appropriate generalization of Eq. (10.20)

$$\operatorname{Re}\sigma(\vec{q},\omega) = \frac{q_e^2}{c_0 h}\left(\frac{h}{q_e^2 \omega N_s}\operatorname{Im}\widetilde{\chi}_{JJ}(\vec{q},\omega)\right), \tag{10.21}$$

where the object in parentheses is $\mathcal{O}(1)$ and dimensionless.

The variable $\operatorname{Re}\bar{\sigma}(\vec{q},\omega)$ is related to the physical (i.e., dimensional) conductivity through $\operatorname{Re}\sigma(\vec{q},\omega) = \frac{h}{q_e^2 c_0}\operatorname{Re}\bar{\sigma}(\vec{q},\omega)$ [see Eq. (10.21)], where c_0 is the separation between two copper oxygen planes in the cuprates. Let us first summarize the relationships between the three sets of variables $\operatorname{Re}\bar{\sigma}(\vec{q},\omega)$, $\operatorname{Im}\widetilde{\chi}_{JJ}(\vec{q},\omega)$ and $\operatorname{Im}\widetilde{\chi}_{\rho\rho}(\vec{q},\omega)$. Combining Eqs. (8.11) and (10.19) we find

$$\text{for } |\vec{q}|a_0 \ll 1,\ \operatorname{Im}\widetilde{\chi}_{JJ}(\vec{q},\omega) = \frac{\omega^2}{|\vec{q}|^2}\operatorname{Im}\widetilde{\chi}_{\rho\rho}(\vec{q},\omega), \tag{10.22}$$

which is a form of the charge conservation law. Combining further with Eq. (10.21) we get the important relation valid in the regime $|\vec{q}|a_0 \ll 1$:

$$\operatorname{Re}\bar{\sigma}(\vec{q},\omega) = \frac{1}{\omega}\left(\frac{\operatorname{Im}\widetilde{\chi}_{JJ}(\vec{q},\omega)}{q_e^2 N_s}\right) = \frac{\omega}{|\vec{q}|^2}\left(\frac{\operatorname{Im}\widetilde{\chi}_{\rho\rho}(\vec{q},\omega)}{q_e^2 N_s}\right). \tag{10.23}$$

In Figs. 10.18–10.20 we display the above closely related triad of variables at room temperature $T = 297, 177, 62$K for two density $n = 0.80$ and $n = 0.85$. In panels (a,d) we show the imaginary part of the density susceptibility $\operatorname{Im}\widetilde{\chi}_{\rho\rho}(\vec{q},\omega)$, in panels (b,e) the real part of dimensionless conductivity $\operatorname{Re}\bar{\sigma}(\vec{q},\omega)$ and in panels (c,f) the current-current susceptibility $\operatorname{Im}\widetilde{\chi}_{JJ}(\vec{q},\omega)$. We compute this objects using our largest systems of $L_x \times L_y = 128 \times 128$, allowing us to access the long wavelength modes $\vec{q} = (\pi/64, \pi/64)$ of the susceptibility.

The overall factor of ω occurs at different locations in the expressions for the three displayed variables, and might be expected to lead to different sensitivity to low frequency noise of various kinds (on an absolute scale). The variable $\operatorname{Im}\widetilde{\chi}_{\rho\rho}$ is most sensitive in this regard. We also note that the peak frequency Ω_p is visible in all three variables, although the peak frequency is slightly different due to a small rightward shift caused by each multiplying factor of ω.

We believe that a systematic study of the variable $\operatorname{Re}\bar{\sigma}(\vec{q},\omega)$ offers some advantages. It can be obtained from the scattering intensity (via $\operatorname{Im}\widetilde{\chi}_{\rho\rho}$), using various available relations. As noted above it might be more stable than $\operatorname{Im}\widetilde{\chi}_{\rho\rho}$ against low ω noise. Secondly its low $\vec{q}$ behavior must evolve continuously from the independently measurable optical conductivity at $\vec{q}=0$, as well as transport measurements at $\omega=0$. These constraints are expected to be helpful in estimating the absolute scale of the susceptibility[9]. Therefore the systematic study of the deduced $\operatorname{Re}\bar{\sigma}(\vec{q},\omega)$, together with the optical conductivity $\operatorname{Re}\bar{\sigma}(0,\omega)$ could be most helpful.

---

[9] This is also true theoretically, as seen in Figs. 10.18 and 10.20. (We checked the continuity in $\vec{q}$ by independent calculations of the two sets of variables using the current vertex defined by Eq (2) of [45].

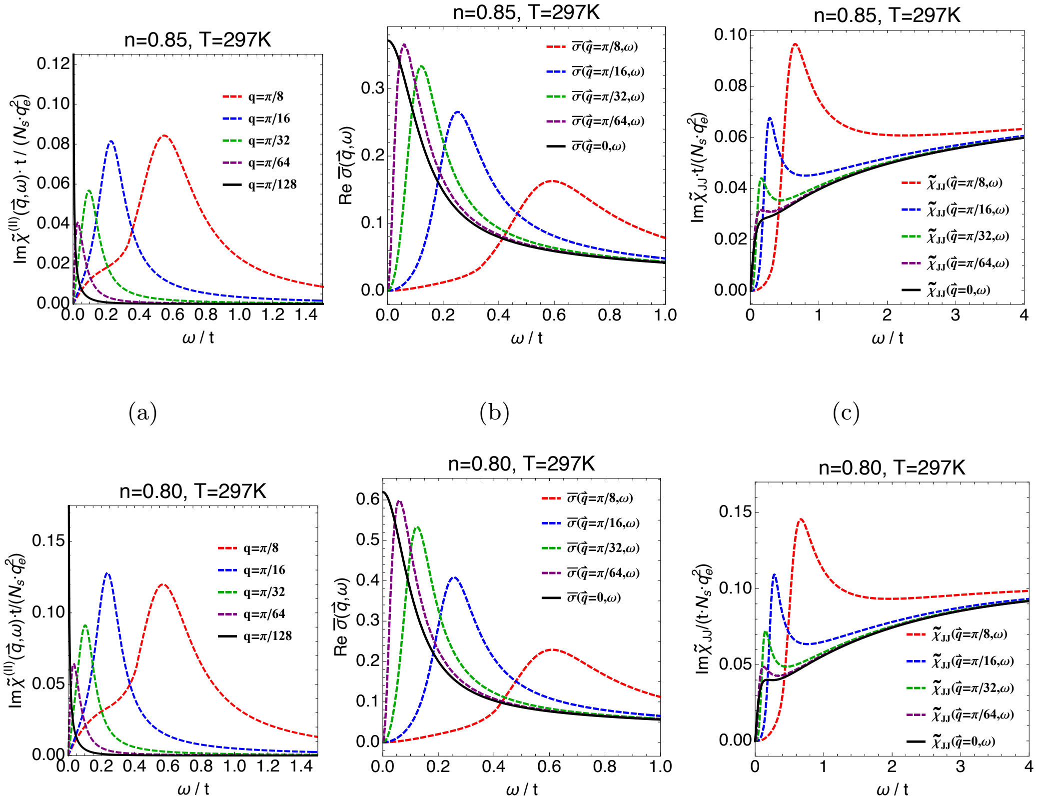

(a) (b) (c)

(d) (e) (f)

Figure 10.18: Panels (**a,d**) display Im $\widetilde{\chi}_{\rho\rho}$, panels (**b,e**) display Re $\bar{\sigma}$ and panels (**c,f**) Im $\widetilde{\chi}_{JJ}$ with the displayed prefactors. Here $T = 297K$, and the density is as shown and the wavevector $\vec{q} = (q, q)$ goes along the $\Gamma \to X$ line. This computation used $L_x \times L_y = 128 \times 128$. The real part of the conductivity $\sigma(\vec{q}, \omega)$ [Eqs. (10.18) and (10.21)] the imaginary part of current susceptibility $\widetilde{\chi}_{JJ}$ [Eqs. (10.19) and (10.22)] and imaginary part of density susceptibility $\widetilde{\chi}^{(II)}_{\rho\rho}$ [Eq. (9.10)] are related by Eq. (10.23). In going from panels (**a** to **c**) or from (**d** to **f**), apart from other constants the second and third objects are found by multiplying the first and second objects with ω respectively. This multiplication causes the peak frequencies to be slightly different in these objects. The flattening of the curves for Im $\widetilde{\chi}_{JJ}$ for all $\vec{q}$ beyond the peak imply that Im $\widetilde{\chi}_{\rho\rho}$ falls off as $1/\omega^2$ in that region. The peaks of all three variables are roughly at the same frequency. The solid black line is separately computed using the current vertex as defined by Eq. (2) of Ref. [45]. In Eqs. (10.22) and (10.23) we summarize the relationship between the two sets of curves presented above, and the curves for Im $\widetilde{\chi}_{\rho\rho}(\vec{q}, \omega)$ in Figs. 10.10 and 10.11. Reconciling the available optical conductivity data with the finite $\vec{q}$ measurements in the MEELS experiments [81, 51, 34] is therefore of considerable interest. Theoretical results for both sets of variables, as in panels (a,b) or in (c,d) are of potential use in such a task.

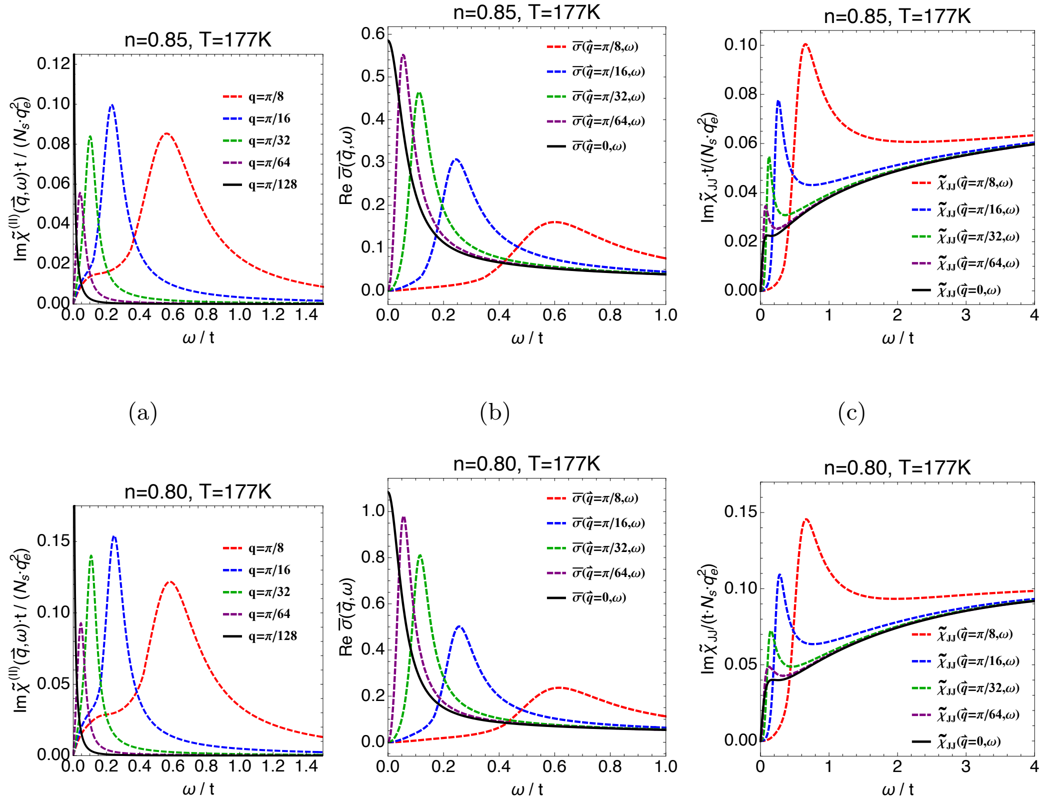

(a) (b) (c)

(d) (e) (f)

Figure 10.19: Panels (**a,d**) display $\mathrm{Im}\,\widetilde{\chi}_{\rho\rho}$, panels (**b,e**) display $\mathrm{Re}\,\bar{\sigma}$ and panels (**c,f**) $\mathrm{Im}\,\widetilde{\chi}_{JJ}$ with the displayed prefactors. Here $T = 177\mathrm{K}$ and the density is as shown and the wavevector $\vec{q} = (q, q)$ is along $\Gamma \rightarrow X$. See the caption of Fig. 10.18 for further common details.

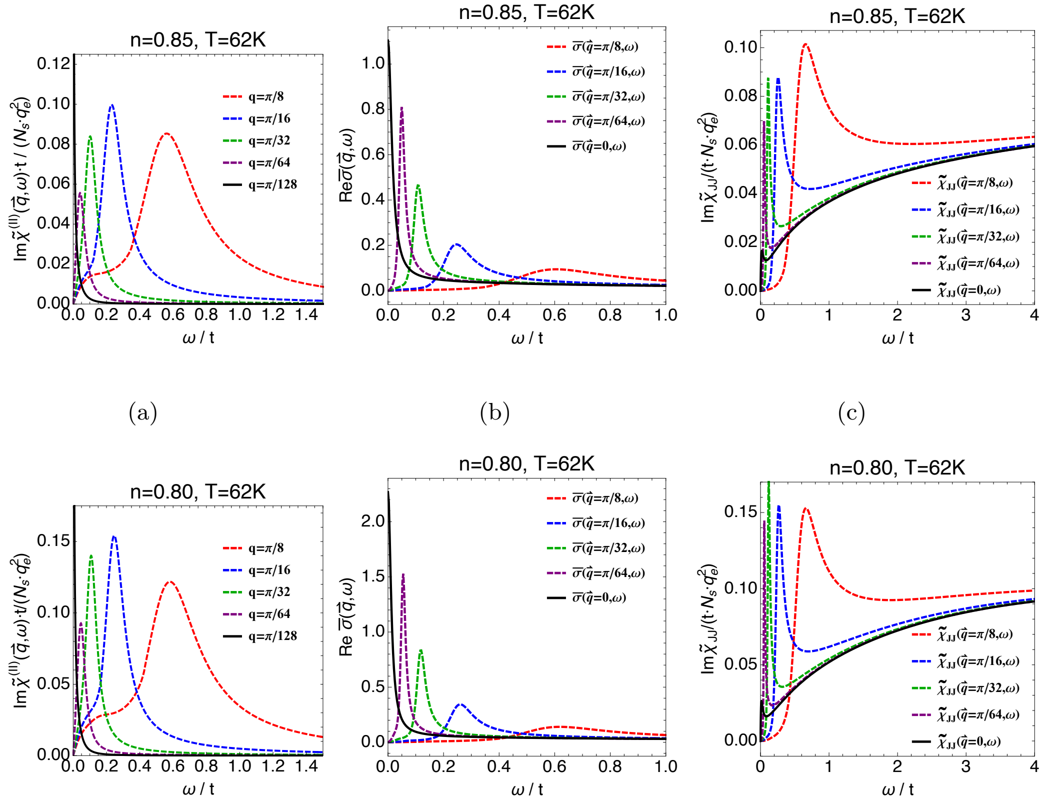

(a)

(b)

(c)

(d)

(e)

(f)

Figure 10.20: Panels (**a,d**) display Im $\widetilde{\chi}_{\rho\rho}$, panels (**b,e**) display Re $\bar{\sigma}$ and panels (**c,f**) Im $\widetilde{\chi}_{JJ}$ with the displayed prefactors. Here $T = 62$K and the density is as shown and the wavevector $\vec{q} = (q, q)$ is along $\Gamma \to X$. See the caption of Fig. 10.18 for further common details.

Chapter 11

Conclusions and Discussion

We have presented results from our calculation of the dynamics of electron fluctuations in the t-J-V_C model of Eq. (7.1). We see that the small quasiparticle weight in the normal state gives rise to a broad background in the electron spectral weight Fig. 10.1. This in turn leads to a smearing of sharp features in the dynamical correlations, as we see in Fig. 10.9. The small Z also reflects in the flattening of the momentum distribution, as seen in Fig. 10.2.

The plasmon energy $\omega_p(\vec{q})$ can be extracted in several distinct ways. We have discussed two methods already, from the peaks in $-\mathrm{Im}(\frac{1}{\varepsilon(\vec{q},\omega)})$, or from the zeroes of $\mathrm{Re}\ \varepsilon(\vec{q},\omega)$ as seen in Figs. 10.15 and 10.16. There is yet another possibility, namely from a measurement of the first frequency moment of the structure function $S(\vec{q},\omega)$ as in Eqs. (C.10) and (C.12). Here the frequency integration must be large enough to contain all the weight from the primary band containing the fermi level, but small enough to exclude interband effects. This balance is familiar from studies of optical conductivity in cuprates [11], where satisfying the various versions of the f-sumrule involves parallel issues.

The results for $\mathrm{Im}\,\widetilde{\chi}_{\rho\rho}(\vec{q},\omega)$ presented in Figs. 10.10 and 10.11 display a slow fall off for $\omega > \Omega_p$ over a substantial range. This behavior is similar to the fall off seen experimentally [34, 51]. From Eq. (10.23) this implies that the current susceptibility $\mathrm{Im}\,\widetilde{\chi}_{JJ}(\vec{q},\omega)$ should flatten out in the same ω range. This is indeed seen in Figs. 10.18 and 10.20 in panels (a,c). We should note that in the panels (b,d) of this figure, the conductivity shows a related sluggish fall off with ω, consistent with Eq. (10.23).

In the region $|\omega| \leq \Omega_p(\vec{q})$, our calculations show that the quasiparticle contribution to $\mathrm{Im}\,\widetilde{\chi}_{\rho\rho}(\vec{q},\omega)$ leads to a linear in ω behavior, as seen in the contrast between the two plots in Fig. 10.9, and in all the low $\vec{q}$ plots of in Figs. 10.10 and 10.11. A low magnitude of Z, as in the ECFL theory makes the linear regime small, but remain non-zero, and hence worth looking for in data.

Finally we believe that extracting systematically the energy scale $\Omega_p(\vec{q})$ for a range of small $\vec{q}$ values is an important task for future experimental studies. In addition to tracking the peaks of the imaginary parts of the various susceptibilities noted in Eq. (10.23), as well as Fig. 10.18 and related figures, approximately evaluating the formula Eqs. (10.13) and (10.14) using data could provide a useful alternative. It is possibly a difficult task if the $\Omega_p(\vec{q})$ is not sufficiently larger than the experimental resolution, and if other sources such as phonons contribute strongly to the scattering intensity. Such a study would provide insight into the nature of the metallic state in the cuprates.

Appendix A

Summary of ECFL Green's function $\mathcal{G}$

The one-electron Green's function $\mathcal{G}$ for the t-J on a lattice in space-time coordinates can be written as

$$\mathcal{G}_{\sigma_i\sigma_j}(\tau_i,\tau_j) = -\langle\langle \widetilde{C}_{i\sigma_i}(\tau_i)\widetilde{C}^{\dagger}_{i\sigma_j}(\tau_j)\rangle\rangle \ . \tag{A.1}$$

Using our notation, the expectation value of an arbitrary observable $Q(\tau_1,\ldots)$ is expressed as

$$\langle\langle Q(\tau_1,\ldots)\rangle\rangle = Tr\ P_\beta\ T_\tau\{e^{-\mathcal{A}}Q(\tau_1,\ldots)\}. \tag{A.2}$$

Here we have T_τ the time-ordering operator, $\mathcal{A} = \int_0^\beta d\tau \hat{\mathcal{A}}(\tau)$ an external potential term, and $P_\beta = e^{-\beta H}/Tr\left(e^{-\beta H}T_\tau e^{-\mathcal{A}}\right)$ the Boltzmann weight factor including $\mathcal{A}$. As usual Eq. (A.1) is a function of difference in lattice coordinate $l = i - j$ and time $\tau \equiv \tau_i - \tau_j$ when the material is homogeneous in both the lattice and time and we study its Fourier transform $\mathcal{G}(\vec{k}, i\omega_k)$.

The $\mathcal{O}(\lambda^2)$ approximation of the ECFL equations determining the Green's function for the t-J model has been discussed earlier in our papers Ref. [66, 6, 65], so we provide a very short summary of the equations used. In the ECFL theory, $\mathcal{G}$ is found using the Schwinger method [66], and expressed as a product of an auxiliary Green's function $\mathbf{g}$ and a "caparison" function $\widetilde{\mu}$:

$$\mathcal{G}(k) = \mathbf{g}(k) \times \widetilde{\mu}(k) \tag{A.3}$$

where $k \equiv (\vec{k}, i\omega_k)$, and $\omega_k = (2k+1)\pi k_B T$ is the Fermionic Matsubara frequency and subscript k is an integer. The auxiliary $\mathbf{g}(k)$ is a Fermi-liquid type Green's function. The Schwinger equation of motion for the physical Green's function can be symbolically written as [66, 6, 65]

$$\left(\mathbf{g}_0^{-1} - \lambda \hat{X} - \lambda Y_1\right) . \, \mathcal{G} = \delta \, (\mathbb{1} - \lambda\gamma). \tag{A.4}$$

where $\hat{X}$ represents a functional derivative and Y_1 describes a Hartree-type energy. Here λ is an expansion parameter and set equal to unity after retaining all second order terms. The non-canonical nature of the Gutzwiller projected operators leads to the term $(\mathbb{1} - \lambda\gamma)$ on the right hand side, this would be just $\mathbb{1}$ for canonical electrons. The decomposition in Eq. (3.2) circumvents this problem since $\mathbf{g}$ is constructed so as to satisfy a canonical equation [66].

To second order (in λ) the ECFL equations [6, 65] are found to be

$$\widetilde{\mu}(k) = 1 - \lambda\frac{n}{2} + \lambda\psi(k) \tag{A.5}$$

$$\mathbf{g}^{-1}(k) = i\omega_k + \boldsymbol{\mu} - \epsilon_{\vec{k}} + \lambda\frac{n}{2}\epsilon_{\vec{k}} - \lambda\phi(k) \tag{A.6}$$

where $\boldsymbol{\mu}$ is the chemical potential and $\epsilon_{\vec{k}}$ is the bare band energy Eq. (C.15) and $\psi(k)$

is the second self-energy. The self-energy $\phi(k)$ factors out as $\phi(k) = \chi(k) + \epsilon'_{\vec{k}}\psi(k)$ where $\chi(k)$ is another function defined below, $\epsilon'_{\vec{k}} = \epsilon_{\vec{k}} - u_0/2$, where u_0 is a Lagrange multiplier. Both $\boldsymbol{\mu}$ and u_0 are determined by constraining the number of electrons defined respectively using $\mathcal{G}$ and $\mathbf{g}$ on Eq. (A.12). The two self-energies functions ψ and χ expanded formally in λ to second order approximation $\mathcal{O}(\lambda^2)$ are $\psi = \psi_{[0]} + \lambda\psi_{[1]} + \ldots$ and $\chi = \chi_{[0]} + \lambda\chi_{[1]} + \ldots$. The expression for these self-energies in the expansion are

$$\psi_{[0]}(k) = 0, \quad \chi_{[0]}(k) = -\sum_{p}\left(\epsilon'_{\vec{p}} + \frac{1}{2}J_{\vec{k}-\vec{p}}\right)\mathbf{g}(p) \tag{A.7}$$

and

$$\psi_{[1]}(k) = -\sum_{pq}\left(\epsilon'_{\vec{p}} + \epsilon'_{\vec{q}} + J_{\vec{k}-\vec{p}}\right)\mathbf{g}(p)\mathbf{g}(q)\mathbf{g}(p+q-k) \tag{A.8}$$

$$\begin{aligned}\chi_{[1]}(k) = &-\sum_{pq}\left(\epsilon'_{\vec{p}} + \epsilon'_{\vec{q}} + J_{\vec{k}-\vec{q}}\right)\left(\epsilon'_{\vec{p}+\vec{q}-\vec{k}} + J_{\vec{k}-\vec{p}}\right)\\ &\times \mathbf{g}(p)\mathbf{g}(q)\mathbf{g}(p+q-k)\end{aligned} \tag{A.9}$$

where we denote $\sum_k \equiv \frac{k_B T}{N_s}\sum_{\vec{k},\omega_k}$ and $J_{\vec{q}}$ is the Fourier transform of J_{ij}. With $\lambda \to 1$, the expressions for the $\mathcal{O}(\lambda^2)$ ECFL equations are

$$\widetilde{\mu}(k) = 1 - \frac{n}{2} + \psi(k) \tag{A.10}$$

$$\begin{aligned}\mathbf{g}^{-1}(k) = i\omega_k + \boldsymbol{\mu} - \epsilon_{\vec{k}} + \frac{n}{2}\epsilon_{\vec{k}} - \chi_{[0]}(k)\\ - \chi_{[1]}(k) - \epsilon'_{\vec{p}}\psi_{[1]}(k)\end{aligned} \tag{A.11}$$

We can determine the two chemical potentials $\boldsymbol{\mu}$ and u_0 by satisfying the following number sum rules

$$\sum_k \mathbf{g}(k)e^{i\omega_k 0^+} = \frac{n}{2} = \sum_k \mathcal{G}(k)e^{i\omega_k 0^+}\ , \tag{A.12}$$

where n is the particle density. We find the spectral function $A(\vec{k},\omega) = -1/\pi \mathrm{Im}\,\mathcal{G}(k)$ by analytically continuing (i.e. $i\omega_k \to \omega + i\eta$) and by solving Eq. (3.2) and Eqs. (A.7)–(A.12) iteratively. We also note the useful spectral representation expressing $\mathcal{G}$ in terms of A:

$$\mathcal{G}(\vec{k}, i\omega_n) = \int_{-\infty}^{\infty} d\nu \, \frac{A(k,\nu)}{i\omega_n - \nu}. \tag{A.13}$$

Appendix B

Susceptibilities and the Structure Function

Our focus is on the charge susceptibility and the related structure function, and hence we first summarize some standard results [54, 36, 1, 24]. Let us define the susceptibility of any pair of operators A, B as

$$\chi_{AB}(\omega + i\eta) = i\int_0^\infty dt\; e^{i\omega t - \eta t}\langle[A(t), B(0)]\rangle \tag{B.1}$$

where $\eta = 0^+$ is a positive infinitesimal, $A(t) = e^{iHt}Ae^{-iHt}$, and the brackets denote the usual thermal average. Its causal nature allows us to write a spectral representation

$$\chi_{AB}(\omega + i\eta) = -\frac{1}{\pi}\int_{-\infty}^{\infty} d\nu \frac{\chi''_{AB}(\nu)}{\omega - \nu + i\eta}. \tag{B.2}$$

By integration over t we find the usual expression for the structure function

$$S_{AB}(\omega) = \int_{-\infty}^{\infty} \frac{dt}{2\pi} e^{i\omega t}\langle A(t)B(0)\rangle, \tag{B.3}$$

and

$$S_{AB}(\omega) = \frac{1}{\pi}\frac{\chi''_{AB}(\omega)}{1 - e^{-\beta\omega}}. \tag{B.4}$$

In order to obtain the charge density structure function we must calculate the charge susceptibility $\chi_{\rho\rho}$ defined from Eq. (B.1) as

$$A = \rho_q = q_e \sum_{k\sigma} \widetilde{C}^{\dagger}_{k\sigma} \widetilde{C}_{k+q\sigma}, \text{ and } B = \rho_{-q}, \tag{B.5}$$

where $q_e = -|e|$ is the electron charge. In real space we write the local charge density ρ_m at site m as

$$\rho_m \equiv q_e n_m, \text{ and } \rho_m = \frac{1}{N_s}\sum_q e^{i\vec{q}.\vec{r}_m}\rho_q, \tag{B.6}$$

where N_s is the number of lattice sites. For our calculations it is more convenient to evaluate the imaginary time object and its Fourier transform

$$\chi_{AB}(\tau) = \langle T_\tau A(\tau) B(0)\rangle, \text{ and } \chi_{AB}(i\Omega_\nu) = \frac{1}{2}\int_{-\beta}^{\beta} d\tau e^{i\Omega_\nu \tau}\chi_{AB}(\tau), \tag{B.7}$$

where $\Omega_\nu = \frac{2\pi}{\beta}\nu$ and $\nu = 0, \pm1, \pm2, \ldots$. We can use analytic continuation $i\Omega_\nu \to \omega + i0^+$ to obtain the physical susceptibility $\chi_{AB}(\omega + i\eta)$ Eq. (B.1) from Eq. (B.7).

Appendix C

Structure Function Frequency Moments

The recent momentum dependent electron energy loss experiments (M-EELS) [81, 51, 34] probe charge response inferred from the inelastic momentum resolved scattering of electrons from the surface of the high T_c superconductor Bi2212 $Bi_2Sr_2CaCu_2O_{8+x}$. Making various simplifying assumptions that are argued for in the work of Mills [49], the experiment gives a readout of the structure function

$$S_{\rho\rho}(\vec{q},\omega) = \int_{-\infty}^{\infty} \frac{dt}{2\pi} e^{i\omega t} \langle \rho_{\vec{q}}(t)\rho_{-\vec{q}}(0)\rangle = \frac{1}{\pi}\frac{\chi''_{\rho\rho}(\omega)}{1-e^{-\beta\omega}}, \tag{C.1}$$

over a substantial portion of the $\vec{q},\omega$ region with remarkably high precision. The energy resolution $\Delta\omega \sim 2$meV. Here $\vec{q}$ is taken to be 2-dimensional. These works present direct information about $\chi_{\rho\rho}$, in fact using the odd-ness of $\chi''_{\rho\rho}$ we can extract this object by combining energy loss and energy gain data:

$$\chi''_{\rho\rho}(\vec{q},\omega) = \pi\left(S_{\rho\rho}(\vec{q},\omega) - S_{\rho\rho}(\vec{q},-\omega)\right) \tag{C.2}$$

The work of [81, 51, 34] presents data for the $\chi''_{\rho\rho}(\omega)$ as well as the inferred screened susceptibility $\widetilde{\chi}_{\rho\rho}$.

C.1 High frequency moments: reducible susceptibility

Using the familiar analyticity of $\chi_{\rho\rho}(\vec{q},\omega)$ in the upper half of the complex ω plane, we can write a spectral representation

$$\chi_{\rho\rho}(\vec{q},\omega) = -\frac{1}{\pi}\int_{-\infty}^{\infty} d\nu \, \frac{\chi''_{\rho\rho}(\vec{q},\nu)}{\omega-\nu+i0^{+}}. \tag{C.3}$$

We note that $\chi''_{\rho\rho}(\vec{q},\nu)$ is odd in ω and hence as $\omega \gg 0$ we get a moment expansion with even terms [57]

$$\lim_{\omega\gg 0} \chi_{\rho\rho}(\vec{q},\omega) = -q_e^2 N_s \left(\frac{\omega^{(1)}(\vec{q})}{\omega^2} + \frac{\omega^{(3)}(\vec{q})}{\omega^4} + \dots\right), \tag{C.4}$$

where the frequency moments $\omega^{(2j+1)}(\vec{q})$ are given by

$$\omega^{(2j+1)}(\vec{q}) = \frac{1}{q_e^2 N_s}\int_{-\infty}^{\infty} \frac{d\omega}{\pi}\omega^{2j+1}\chi''_{\rho\rho}(\vec{q},\omega), \tag{C.5}$$

or upon using Eq. (C.2)

$$\omega^{(2j+1)}(\vec{q}) = \frac{2}{q_e^2 N_s}\int_{-\infty}^{\infty} d\omega\omega^{2j+1} S(\vec{q},\omega). \tag{C.6}$$

C.2 High frequency moments: irreducible susceptibility

In the presence of long-ranged Coulomb interactions it is necessary [54] to distinguish between reducible susceptibility (or polarization) $\chi_{\rho\rho}$ and the irreducible susceptibility (or polarization) $\widetilde{\chi}_{\rho\rho}$. The irreducible susceptibility $\widetilde{\chi}_{\rho\rho}$ can be shown to satisfy a spectral representation

$$\widetilde{\chi}_{\rho\rho}(\vec{q},\omega) = -\frac{1}{\pi}\int_{-\infty}^{\infty} d\nu \, \frac{\widetilde{\chi}''_{\rho\rho}(\vec{q},\nu)}{\omega - \nu + i0^{+}}. \tag{C.7}$$

This is completely analogous to Eq. (C.3), and using a moment expansion analogous to Eq. (C.4) we get

$$\lim_{\omega \gg 0} \widetilde{\chi}_{\rho\rho}(\vec{q},\omega) = -q_e^2 N_s \left(\frac{\widetilde{\omega}^{(1)}(\vec{q})}{\omega^2} + \frac{\widetilde{\omega}^{(3)}(\vec{q})}{\omega^4} + \ldots \right), \tag{C.8}$$

In order to determine the moments $\widetilde{\omega}^{(2l+1)}(\vec{q})$, we recast Eq. (8.10) in the form

$$\widetilde{\chi}_{\rho\rho}(\vec{q},\omega) = \frac{\chi_{\rho\rho}(\vec{q},\omega)}{1 - \frac{V(\vec{q})}{N_s}\chi_{\rho\rho}(\vec{q},\omega)}. \tag{C.9}$$

We next plug into this expression the high frequency expansion Eq. (C.4) giving an infinite series in $\frac{1}{\omega^2}$. Comparing with Eq. (C.8), the moments $\widetilde{\omega}^{(2l+1)}(\vec{q})$ can be determined in terms of $\omega^{(2l+1)}(\vec{q})$. For our purpose we only need the first moment:

$$\widetilde{\omega}^{(1)}(\vec{q}) = \omega^{(1)}(\vec{q}). \tag{C.10}$$

We make extensive use of the first moment $\omega^{(1)}(\vec{q})$ below, let us note that it is in frequency units and provides a very important scale in the problem. We now relate this frequency to $\kappa(\vec{q})$. From Eq. (8.14) we note that

$$\lim_{\omega \gg 0} \varepsilon(\vec{q},\omega) \to 1 - V(\vec{q}) N_s \left(\frac{\widetilde{\omega}^{(1)}(\vec{q})}{\omega^2} + \frac{\widetilde{\omega}^{(3)}(\vec{q})}{\omega^4} + \ldots \right). \tag{C.11}$$

Comparing the leading term with the expression in Eqs. (10.15) and (10.16), we get

$$\widetilde{\omega}^{(1)}(\vec{q}) = \frac{a_0 \hbar}{q_e^2}\kappa(\vec{q}), \tag{C.12}$$

where we temporarily reintroduced the lattice constant a_0 and $\hbar$ to emphasize that $\widetilde{\omega}^{(1)}$ is in frequency units, while κ is the square of a frequency[10].

Using Eq. (10.16), the first moment also determines the plasmon energy as $\omega_p(\vec{q}) = \sqrt{\frac{N_s}{q_e^2} V(\vec{q}) \kappa(\vec{q})}$. Proceeding further we can express $\kappa(\vec{q})$ in 2-d explicitly in terms of $\vec{q}$, the band hopping parameters and the averages over the momentum distribution function $\langle \widetilde{C}_k^\dagger \widetilde{C}_k \rangle$ of the type $\langle \cos k_x \rangle_{ave} \equiv \frac{1}{N_s} \sum_k \cos k_x \langle \widetilde{C}_k^\dagger \widetilde{C}_k \rangle$.

Using Eq. (8.4) and the band dispersion parameters t, t' representing the nearest and next nearest neighbor hops on the square lattice:

$$\varepsilon_k = -2t(\cos k_x + \cos k_y) - 4t' \cos k_x \cos k_y. \tag{C.15}$$

We find

$$\widetilde{\omega}^{(1)}(\vec{q}) = 8t \langle \cos k_x \rangle_{ave} (2 - \cos q_x - \cos q_y) + 16t' \langle \cos k_x \cos k_y \rangle_{ave} (1 - \cos q_x \cos q_y). \tag{C.16}$$

For small $\vec{q}$ we find

$$\lim_{\vec{q} \to 0} \widetilde{\omega}^{(1)}(\vec{q}) \to |\vec{q}|^2 \frac{\mathcal{T}}{q_e^2}, \tag{C.17}$$

where we utilized Eq. (8.5), and

$$\mathcal{T} = q_e^2 \left(4t \langle \cos k_x \rangle_{ave} + 8t' \langle \cos k_x \cos k_y \rangle_{ave} \right) \tag{C.18}$$

---

[10] A comment on the dimensions of these variables may be useful. The variables $\kappa(\vec{q})$ and $\mathcal{T}$ have dimensions of frequency squared. This feature is submerged in the notation since we have set the lattice constant $a_0 \to 1$ and also set $\hbar \to 1$. To restore the dimensions we should read Eq. (8.4) as

$$\kappa(\vec{q}) = \frac{2 q_e^2}{a_0 \hbar^2 N_s} \sum_{k\sigma} \left(\varepsilon_{\vec{k}+\vec{q}} - \varepsilon_{\vec{k}} \right) \langle \widetilde{C}_{\vec{k}\sigma}^\dagger \widetilde{C}_{\vec{k}\sigma} \rangle. \tag{C.13}$$

and Eq. (8.6) as

$$\mathcal{T} = \frac{q_e^2}{a_0 N_s \hbar^2} \sum_{k\sigma} \left(\frac{d^2 \varepsilon_{\vec{k}}}{d(k_x a_0)^2} \right) \langle \widetilde{C}_{\vec{k}\sigma}^\dagger \widetilde{C}_{\vec{k}\sigma} \rangle, \tag{C.14}$$

We see from Eq. (10.17) that $\mathcal{T}$ determines the total weight of the optical conductivity. The relevant averages of the cosines are tabulated in Table 10.1, where we see the enormous reduction from uncorrelated values brought about by the strong correlations.

For completeness we note that our notation for the reducible $\chi_{\rho\rho}$ and irreducible $\widetilde{\chi}_{\rho\rho}$ polarizations can be mapped into that used in [81, 51, 34] by setting

$$\begin{aligned} &\chi_{\rho\rho} \to -\chi \\ &\widetilde{\chi}_{\rho\rho} \to -\Pi \\ &\varepsilon \to \varepsilon/\varepsilon_{\infty}. \end{aligned} \tag{C.19}$$

Part IV

CONCLUSION

In this part we briefly summarize a few important results from each part of the dissertation, and we discuss some work in progress.

In Part II we adapted ECFL theory to account for strain-induced anisotropy in order to explore the nematicity in strange metals, and in particular we calculated the strain-induced anisotropic resistivity, kinetic energy (f-sumrule for the optical conductivity) and the local density of state (measurable via STM) and we also calculated the elastoresistivity and other related susceptibilities. Our calculations amount to predictions of physical response of these materials and we are awaiting further experimental test. These results are expected to be applicable to high T_c superconducting materials, specifically high-T_c cuprates. The recent experimental measurements in Ref. [41] of the nematic susceptibility χ_{nem} (i.e., elastoresistivity) in cuprates is consistent our theoretical estimates; even though, our model contains no explicit mechanism to account for nematic fluctuations. On the other hand, measurements of the nematic susceptibility in iron pnictide materials [17, 12] are much more sensitive than our theoretical estimates, which presumably is an effect of downfolding pnictides from a many-band to an effective single band model, and this yields parameters that are more sensitive to strain.

In Part III we remarked on recent experiments using a novel approach, a inelastic electron scattering probe, which essentially gives a readout of the structure function after making various simplifying assumptions. This is exciting since the structure function is an object which contains information about the physics of the charge density fluctuations in the cuprate materials. Motivated by these results, we use an extended version of ECFL theory [72] (based on the t-J-V_C model) which adds the effects long-range Coulomb-type interactions V_c to the t-J model and a set of novel expressions for the dielectric constant and charge susceptibility to explore the dielectric response in cuprates. Our calculation of $\operatorname{Im}\widetilde{\chi}_{\rho\rho}$ shows a fall off for $\omega > \Omega_p$, and this behavior similar to the fall seen in experiments [34, 51] and serves as one benchmark for the t-J-V_C model. We also mention that dielectric constant ε is exact in the uniform static limit and has the correct high frequency behavior for our model, and our calculation of the finite $\vec{q}$ electron energy loss $-\operatorname{Im}\{1/\varepsilon\}$ has broad peaks at similar energies as seen in experiments and it has the expected $1/\omega^2$ high frequency behavior. Our calculation of the plasma energy ω_p and f-sumrule $\widetilde{\omega}^{(1)}$ are two more strong benchmarks of our theory awaiting experimental tests. Closely related to $\widetilde{\chi}_{\rho\rho}$ is the current susceptibility $\widetilde{\chi}_{JJ}$ and optical conductivity $\operatorname{Re}\sigma$ which both can benchmarked t-J-V_C model via alternative experimental means. We also comment on the importance of measuring the characteristic energy Ω_p — the approximate turn-around frequency of $\widetilde{\chi}_{\rho\rho}$ for small $\vec{q}$ — since this material signature is measurable in absentia of reliable information about the relative intensity of $\widetilde{\chi}_{\rho\rho}$.

We also mention some of our work in progress that is directly related to this dissertation. One of the projects currently in progress is a calculation of the non-canonical electron Green's function $\mathcal{G}$ using for the first time the $\mathcal{O}(\lambda^3)$ approximation of ψ and χ self-energies described in Eq. (A.4) for two- and ∞-dimensional systems using a novel pair of sum rules [alternative to Eq. (A.12)] to determine the Lagrange multipliers μ' and u_0. The other work in progress is a scheme to calculate $\mathcal{G}$, the usual Green's function for t-J model, and $\mathcal{F}$, the anomalous Green's function, for extremely correlated superconductors [73].

Bibliography

[1] A. A. Abrikosov, L. Gor'kov and I. Dzyaloshinski, *Methods of Quantum Field Theory in Statistical Physics* , Prentice-Hall, Englewood Cliffs, NJ (1963).

[2] P. W. Anderson, Science **235**, 1196 (1987).

[3] Y. Ando, in *High Tc Superconductors and Related Transition Metal Oxides* (A Bussmann-Holder and H. Keller, Springer, Berlin, 2007) pp. 17-28

[4] Y. Ando, S. Komiya, K. Segawa, S. Ono, and Y. Kurita, Phys. Rev. Lett. **93**, 267001 (2004)

[5] T. Arai and M. H. Cohen, Phys. Rev. B **21**, 3300 (1980); ibid. **21**, 3309 (1980); T. Arai, ibid. **21**, 3320 (1980).

[6] M. Arciniaga, P. Mai and B. S. Shastry, Phys. Rev. B **101**, 245149 (2020).

[7] N. P. Armitage, D. H. Lu, C. Kim, A. Damascelli, K. M. Shen, F. Ronning, D. L. Feng, P. Bogdanov, X. J. Zhou, W. L. Yang, Z. Hussain, P. K. Mang, N. Kaneko, M. Greven, Y. Onose, Y. Taguchi, Y. Tokura, and Z.-X. Shen, Phys. Rev. B **68** 064517 (2003).

[8] F. Aryasetiawan, M. Imada, A. Georges, G. Kotliar, S.Biermann, and A. I. Lichtenstein, Phys. Rev. B **70**, 195104 (2004).

[9] D. N. Basov and T. Timusk, Rev. Mod. Phys. **77**, 721 (2005).

[10] D. N. Basov, R. D. Averitt, D. van der Marel, M. Dressel, and K. Haule,Rev. Mod. Phys. **83**, 471 (2011).

[11] D. N. Basov and T. Timusk, Rev. Mod. Phys. **77**, 721 (2005); J Orenstein, G A Thomas, A J Millis, S L Cooper, D H Rapkine, T Timusk, L F Schneemeyer, J V Waszczak, Phys. Rev. B **42**, 6342 (1990); D. van der Marel, F. Carbone, A. B. Kuzmenka and F. Giannini, Ann. Phys. **321**, 1716 (2006).

[12] E. C. Blomberg, M. A. Tanatar, R. M. Fernandes, I. I. Mazin, Bing Shen, Hai-Hu Wen, M. D. Johannes, J. Schmalian and R. Prozorov, Nature Communications **4** 1914 (2013)

[13] W. F. Brinkman and T. M. Rice, Phys. Rev. B **2**, 4302 (1970).

[14] K. Bouadim, N. Paris, F. Hebert, G. G. Batrouni, and R. T. Scalettar, Phys. Rev. B **76**, 085112 (2007).

[15] M. Casula, Ph. Werner, L. Vaugier, F. Aryasetiawan, T. Miyake, A. J. Millis, and S. Biermann, Phys. Rev. Letts. **109**, 126408 (2012).

[16] P. Choubey, A. Kreisel, T. Berlijn, B. M. Andersen, and P. J. Hirschfeld, Phys. Rev. B **96**, 174523 (2017).

[17] J. H. Chu, H. Kuo, J. G. Analytis, I. R. Fisher, Science **337**, 710 (2012).

[18] J. H. Chu, H. Kuo, J. C. Palmstrom, S. A. Kivelson and I. R. Fisher, Science **352**, 958 (2016).

[19] A. Damascelli, Z. Hussain, and Z-X Shen, Rev. Mod. Phys. **75**, 473 (2003).

[20] S. Das Sarma, S. Adam, E. H. Hwang, and Enrico Rossi,Rev.Mod. Phys. **83**, 407 (2011).

[21] X.Y. Deng, J. Mravlje, R. Žitko, M. Ferrero, G. Kotliar and A. Georges, Phys. Rev. Lett. **110**, 086401 (2013).

[22] W. Ding, R. Žitko, P. Mai, E. Perepelitsky and B. S. Shastry, Phys. Rev. B **96**, 054114 (2017); W. Ding, Rok Žitko, and B. S. Shastry, ibid. **96**, 115153 (2017).

[23] M. Dupuis, Prog. Theor. Phys. **37**, 502 (1967).

[24] A. L. Fetter and J. D. Walecka, *Quantum Theory of Many-Particle Systems*, (McGraw-Hill, New York, 1971.)

[25] K. Fujita, A. R. Schmidt, E. -A. Kim, M. J. Lawler, D. H. Lee, J. C. Davis, H. Eisaki, and S. -i. Uchida, J. Phys. Soc. Jpn. **81**, 011005 (2012).

[26] A. Georges, G. Kotliar, W. Krauth, and M. J. Rozenberg, Rev. Mod. Phys. **68**, 13 (1996)

[27] R. L. Greene, P. R. Mandal, N. R. Poniatowski and T. Sarkar, Ann. Rev. Condens. Matter Phys. 11, 213 (2020)

[28] G. -H. Gweon, B. S. Shastry, and G. D. Gu, Phys. Rev. Lett. **107**, 056404 (2011).

[29] G. -H. Gweon, B. S. Shastry and G. D. Gu, Phys. Rev. Letts. 107, 056404 (2011).

[30] M. Hamermesh, *Group Theory And Its Application To Physical Problems* (Reading, Mass: Addison-Wesley Pub. Co., 1962)

[31] V. Heine, Phys. Rev. **153**, p. 673 (1967).

[32] E. W. Huang, R. Sheppard, B. Moritz and T. P. Devereaux, Science **366**, 987 (2019).

[33] J. Hubbard, Proc. Phys. Soc., London, Sect. **A 68**, 976 (1955); K. S. Singwi, M. P. Tosi, R. H. Land, and A. Sjolander Phys. Rev. **176**, 589 (1968); A. Holas, S. Rahman, Phys. Rev. B **35**, 2720 (1987);

[34] A. A. Husain, M. Mitrano, M. S. Rak, S. Rubeck. B. Uchoa, K. March, C. Dwyer, J. Scheenloch, R. Zhang, G. D. Gu and P. Abbamonte, Phys. Rev. X **9**, 041062 (2019).

[35] E. H. Hwang and S. Das Sarma, Phys. Rev. B **75**, 205418 (2007).

[36] L. P. Kadanoff, G. Baym, *Quantum Statistical Mechanics: Green's Function Methods in Equilibrium and Nonequilibrium Problem*, Benjamin, NY, 1962

[37] A. Koitzsch, G. Blumberg, A. Gozar, B. S. Dennis, P. Fournier, and R. L. Greene, Phys. Rev. B **67** 184522 (2003).

[38] J. D. Koralek, J. F. Douglas, N. C. Plumb, Z. Sun, A. V. Federov, M. M. Murnane, H. C. Kapteyn, S. T. Cundiff, Y. Aiura, K. Oka, H. Eisaki, and D. S. Dessau, Phys. Rev. Lett. **96**, 017005 (2006).

[39] A. Kreisel, P. Choubey, T. Berlijn, W. Ku, B. M. Andersen, and P. J. Hirschfeld, Phys. Rev. Lett. **114**, 217002 (2015).

[40] G. Kotliar, S. Y. Savrasov, K. Haule, V. S. Oudovenko, O. Parcollet and C. A. Marianetti, Rev. Mod. Phys. **78** 865 (2006).

[41] K. Ishida, S. Hosoi, Y. Teramoto, T. Usui, Y. Mizukami, K. Itaka, Y. Matsuda, T. Watanabe, and T. Shibauchi, J. Phys. Soc. Jpn. **89**, 064707 (2020)

[42] L. D. Landau, & E. M. Lifshitz, *Quantum Mechanics: Non-Relativistic Theory*, 3rd ed. (New York : Pergamon Press, 1991), Vol. 3, p. 366

[43] W. S. Lee, I. M. Vishik, D. H Lu and Z-X Shen, J. Phys.: Condens. Matter **21**, 164217 (2009).

[44] J. M. Luttinger, Phys. Rev. **121**, 942 (1960); esp. Sec. 2.

[45] P. Mai and B. S. Shastry, Phys. Rev. B **98**, 115101 (2018).

[46] P. Mai, S. R. White and B. S. Shastry, Phys. Rev. B **98**, 035108 (2018).

[47] T. A. Maier, M. Jarrell, T. Prushke, and M. H. Hettler, Rev. Mod. Phys. **77**, 1027 (2005).

[48] R. S. Markiewicz, S. Sahrakorpi, M. Lindroos, Hsin Lin, and A. Bansil, Phys. Rev. B**72**, 054519 (2005).

[49] D. L. Mills, Surf. Sci. **48**, 59 (1975).

[50] F. Ming, S. Johnston, D. Mulugeta, T. S. Smith, P. Vilmercati, G. Lee, T. A. Maier, P. C. Snijders, and H. H. Weitering, Phys. Rev. Lett. **119**, 266802 (2017).

[51] M. Mitrano, A. A. Husaina, S. Viga, A. Kogara, M. S. Rak, S. I. Rubeck, J. Schmalian, B. Uchoa, J. Schneeloch, R. Zhong, G. D. Gu, and P. Abbamonte, PNAS, **115**, 5392 (2018).

[52] H. Mori, Prog. Theor. Phys. **33**, 423 (1965); **34**, 399 (1965).

[53] Y. Nambu, Phys. Rev. **117**, 648 (1960).

[54] P. Nozières, in *Theory of Interacting Fermi Systems*, (W. A. Benjamin, New York, 1964).

[55] M. Ogata and H. Fukuyama *Rep. Prog. Phys.* **71**, 036501 (2008).

[56] Y. Onose, Y. Taguchi, K. Ishizaka, and Y. Tokura, Phys. Rev. B **69**, 024504 (2004).

[57] K. N. Pathak and P. Vashishta, Phys. Rev. B **7**, 3649 (1973).

[58] M. M. Qazilbash, A. Koitzsch, B. S. Dennis, A. Gozar, H. Balci, C. A. Kendziora, R. L. Greene, and G. Blumberg, Phys. Rev. B **72**, 214510 (2005); A. Koitzsch, G. Blumberg, A.Gozar, B. S. Dennis, P. Fournier, and R. L. Greene, Phys. Rev. B **67**, 184522 (2003).

[59] A. K. Rajagopal, Nucl. Phys. 57, 435 (1964); A. K. Rajagopal, H. Brooks, and N. Ranganathan, Nuovo Cimento, Suppl. 5, 807 (1967).

[60] T. M. Rice and W. F. Brinkman, “Some aspects of the theory of the Mott transition”, in *Critical Phenomena in Alloys, Magnets and Superconductors*, ed. R. E. Mills, E. Ascher and R. H. Jaffee, p593 (McGraw-Hill, New York) (1971).

[61] M. C. Shapiro, P. Hlobil, A. T. Hristov, A. V. Maharaj, and I. R. Fisher, Phys. Rev. B **92**, 235147 (2015)

[62] B. S. Shastry, Phys. Rev. B **81**, 045121 (2010).

[63] B. S. Shastry, Phys. Rev. B **87**, 125124 (2013)

[64] B. S. Shastry and P Mai Phys. Rev. B 101, 115121 (2020)

[65] B. S. Shastry and P. Mai, New J. Phys. **20** 013027 (2018); P. Mai and B. S. Shastry Phys. Rev. B **98**, 205106 (2018)

[66] B.S. Shastry, Phys. Rev. Lett. **107**, 056403 (2011)

[67] B. S. Shastry, Phys. Rev. Letts. **63**, 1288 (1989).

[68] B. S. Shastry, Phys. Rev. B **84**, 165112 (2011); Phys. Rev. B **86**, 079911(E) (2012).

[69] B S Shastry, Phys. Rev. B **73**, 085117 (2006).

[70] B. S. Shastry, Rep. Prog. Phys. **72** 016501 (2009); Eq. (6) and Eq. (64).

[71] B. S. Shastry and E. Perepelitsky, Phys. Rev. B **94**, 045138 (2016); R. Žitko, D. Hansen, E. Perepelitsky, J. Mravlje, A. Georges and B. S. Shastry, ibid. **88**, 235132 (2013); B. S. Shastry, E. Perepelitsky and A. C. Hewson, ibid. **B 88**, 205108 (2013).

[72] B. S. Shastry and M. R. Arciniaga arXiv:2111.04891

[73] B. S. Shastry arXiv:2102.08395v3

[74] F. Stern, Phys. Rev. Letts. **18**, 546 (1967).

[75] H. L. Störmer, R. Dingle, A.C. Gossard, W. Wiegmann, M. D. Sturge, Sol. State Comm **29**, 705 (1979).

[76] S. Sugai, J. Nohara, R. Shiozaki, T. Muroi, Y. Takayanagi, N.Hayamizu, K. Takenaka, and K. Okazaki, J. Phys.: Condens.Matter **25**, 415701 (2013); S. Sugai, Y. Takayanagi, N. Hayamizu, T. Muroi, J. Nohara, R.Shiozaki, K. Okazaki, and K. Takenaka, Physica C **470**, S97 (2010).

[77] M. Tinkham, *Group Theory and Quantum Mechanics* (New York : McGraw-Hill, 1964)

[78] J. Town, T. Cockerill, M. Dahan, I. Foster, K. Gaither, A. Grimshaw, V. Hazlewood, S. Lathrop, D. Lifka, G. D. Peterson, R. Roskies, J. R. Scott, N. Wilkins-Diehr "XSEDE: Accelerating Scientific Discovery", Computing in Science & Engineering, Vol.16, No. 5, pp. 62-74, Sept.-Oct. 2014, doi:10.1109/MCSE.2014.80

[79] C. M. Varma, Phys. Rev. B **96**, 075122 (2017).

[80] C. M. Varma, P. B. Littlewood, S. Schmitt-Rink, E. Abrahams and A. E. Ruckenstein, Phys. Rev. Letts. **63**, 1999 (1989).

[81] S. Vig, A. Kogar, M. Mitrano, A. A. Husain, L. Venema, M. S. Rak, V. Mishra, P. D. Johnson, G. D. Gu, E. Fradkin, M. R. Norman and P. Abbamonte, SciPost Phys. **3**, 026 (2017).

[82] D. Vollhardt, Rev. Mod. Phys. **56**, 99 (1984) (esp. Sec. IV).

[83] W. Xu, K. Haule, and G. Kotliar, Phys. Rev. Lett. **111**, 036401 (2013).

[84] Y. J. Yan, M. Q. Ren, H. C. Xu, B. P. Xie, R. Tao, H. Y. Choi, N. Lee, Y. J. Choi, T. Zhang, and D. L. Feng, Phys. Rev. X **5**, 041018 (2015).

[85] T. Yoshida, X. J. Zhou, D. H. Lu, S. Komiya, Y. Ando, H. Eisaki, T. Kakeshita, S. Uchida, Z. Hussain, Z-X Shen and A. Fujimori, J. Phys.: Condens. Matter **19** 125209 (2007).

[86] F. C. Zhang and T. M. Rice, Phys. Rev. B**41**, 7243 (1990);

[87] Y. Zhang, Y. F. Zhang, S. X. Yang, K.-M. Tam, N. S. Vidhyadhiraja and M. Jarrell Phys. Rev. B **95** 144208 (2017).